Improving Data Quality for High Resolution Functional MRI in Cognitive Neuroscience Applications

Huang Pei
Wolfson College

MRC Cognition and Brain Sciences Unit
School of Clinical Medicine
University of Cambridge

This dissertation is submitted for the degree of Doctor of Philosophy
September 2019

Table of Contents

Thesis Summary

Since the first successful Magnetic Resonance Imaging (MRI) image was produced by Paul Lauterbur in 1973, the field of MRI has been improving by leaps and bounds. The number of MRI and functional MRI (fMRI) papers have sky rocketed over the last decade, alongside with advancements in MRI field strength and techniques. In this thesis, I explore various methods for improving data quality for high resolution fMRI in 3T and 7T MRI scanners.

Firstly, I studied the effect of Prospective Motion Correction (PMC) on 3T data using a simple visual paradigm. In contrast to most conventional techniques that use retrospective motion correction (RMC), PMC collects real-time motion data and uses it to update the acquisition field of view prior to each radiofrequency (RF) pulse. This allows for the correction of spin-history effects and intra-volume distortions. In this study, I utilized a secondary optical camera in the bore of the scanner to track a Moiré phase marker attached to the participant via a custom-moulded dental mouthpiece. I demonstrated that the camera is capable of accurately tracking the participant's head motion. While simple metrics such as temporal signal-to-noise ratio (tSNR) and functional contrast-to-noise ratio (fCNR) showed no difference between the two methods, more complex analysis such as the Linear Discriminant Contrast (LDC) showed that the PMC data was indeed cleaner than the RMC data for higher resolution data.

Next, I compared the sensitivity of two multi-voxel pattern analysis (MVPA) methods, Support Vector Machines (SVM) and Linear Discriminant Contrast (LDC). MVPA attempts to capture the relationship between the spatial fMRI activity and the experimental manipulations by treating it as a supervised learning problem. This is a promising technique that can capture spatial activation patterns that are lost in univariate analysis. I demonstrated through both actual fMRI data and computer simulations that LDC is a better MVPA metric than SVM. This agrees with our theory that SVM has more inherent variability and less sensitivity due to its limitations, discretization of results, rigid decision boundaries and ceiling effects.

Subsequently, I analysed the quality of fMRI data acquired in a 3T Prisma scanner vs a 7T Terra scanner using a visual attention paradigm. While 7T scanners are becoming increasingly commonplace with over 70 of them worldwide now, the higher field strength also comes with its own host of problems. Field inhomogeneities and artefacts are a larger problem at 7T, and the smaller voxel sizes also cause data to be more susceptible to motion. As such, it is important to establish if there is a real benefit to using a 7T scanner. I observed that both 3T and 7T data showed similar trends with comparable z-scores and concluded that both scanners yielded comparable results. However, the 7T data was acquired at a much higher resolution (64x smaller volume per voxel) and thus, these results indicate

a benefit of 7T as comparable results were achieved in spite of the smaller voxel volume. I hypothesized that acquiring data in a 7T scanner would be informative if studies sought to probe further into laminar or columnal structures which require submillimetre resolution, while a 3T scanner should suffice for studies looking at coarse regional activations. I did not explore the benefits of using 7T MRI at coarser resolutions.

I also assessed the utility of boundary-based registration (BBR) realignment to improve on conventional RMC techniques to realign fMRI time series. Some motion artefacts affect the image in non-rigid ways and thus, voxel-based registration (VBR), generally utilized in conventional RMC, might be insufficient to properly realign fMRI time series. I demonstrated that BBR realignment outperforms VBR realignment across multiple metrics at submillimetre resolution, but no difference was observed at lower resolutions.

Lastly, I examined the process of cleaning up 7T fMRI data for laminar analysis. Gradient echo (GE) sequences have been widely used for fMRI studies due to the high signal-to-noise ratio (SNR) and low specific absorption rate (SAR) relative to other sequences. However, GE sequences have been shown to exhibit superficial bias due to the presence of draining veins. I employed two methods- excluding venous voxels and utilizing a regression analysis, to remove superficial bias in an attempt to unmask any laminar effects for a visual attention task.

In summary, I have explored various methods of optimizing fMRI data, ranging from initial setup decisions, such as which field strength scanner to use, to final MVPA analysis methods. I also analysed methods to remove motion artefacts, through both PMC and RMC, as well as post-processing methods to remove superficial bias in laminar data.

Preface

Parts of this PhD work has been featured in following publications:

- Huang, P., Carlin, J.D., Alink, A., Kriegeskorte, N., Henson, R.N., Correia, M.M., 2018. Prospective motion correction improves the sensitivity of fMRI pattern decoding. Hum. Brain Mapp. 39, 4018–4031. https://doi.org/10.1002/hbm.24228
- Huang, P., Carlin, J.D., Henson, R.N., Correia, M.M., 2019. Improved motion correction of submillimetre 7T fMRI time series with boundary-based registration (BBR). BioRxiv. https://doi.org/10.1101/747386

Parts of this PhD work have been presented in the form of posters at the following conferences:

- Huang, P., Hayes, D., Correia, M., 2017. Validating the accuracy and effectiveness of Prospective Motion Correction on rsfMRI, in: Proceedings of the 25th Scientific Meeting of ISMRM. p. 1275.
- Huang, P., Kriegeskorte, N., Henson, R., Alink, A., Correia, M., 2017. Quantifying the effectiveness of prospective motion correction using a visual fMRI task, in: Proceedings of the 25th Scientific Meeting of ISMRM. p. 1276.

- Huang, P., Correia, M.M., Gardner, J., Carlin, J.D., 2018. Spatial- and category-based attention have distinct functional organizations in human visual cortex, in: Proceedings of the 26th Scientific Meeting of ISMRM. p. 2360.

- Huang, P., Carlin, J.D., Henson, R.N., Correia, M.M., 2019. Improved motion correction of submillimetre 7T fMRI time series with boundary-based registration (BBR), in: Proceedings of the 27th Scientific Meeting of ISMRM. p. 4427.

Acknowledgements

This PhD has been a truly exciting and challenging experience, which would not have been possible without the support and guidance from the following people.

First and foremost, I wish to thank my main supervisor, Dr Marta M. Correia, for her unwavering support and patience with me. She allowed me the freedom to determine the direction of my research and encouraged me to follow my own ideas, while always been there to provide guidance and advice when I needed it. I would also like to thank Dr Johan D. Carlin and Prof Richard N. Henson for their invaluable advice and for taking over as my supervisors when Dr Correia was on maternity leave. Our meetings felt extremely insightful to me and I have always walked away brimming with new ideas. Throughout the course of my PhD, my supervisors have also impressed me with the breadth of their knowledge and motivated me to never stop learning.

I would also like to express my gratitude to the radiographers at both MRC-CBU and WBIC for their assistance in data acquisition. Their natural friendliness and good humour often made the long scan sessions fly by in a blink of an eye. I would also like to acknowledge Dr Chris Rodgers and Dr Catarina Rua for helping out with the 7T data acquisitions as well as implementing the sequences at 7T.

I would also like to thank the researchers at Maastricht and Oxford for allowing me to visit their 7T sites and sharing their experiences and insights with me. Their tips and advice were valuable in my work on the 7T scanner.

My fellow PhD candidates (Courtney, Hannes, Laura, Moataz, Shraddha, Sneha, Tanya and Verity) were also an important part of my PhD experience. Their friendship and laughter helped me through the tough times of my PhD and bouncing ideas off them in our office often resulted in new insights. These four years were definitely made more enjoyable with our board games sessions and hanging out together after work.

Last, but not least, I would like to thank my parents, Huang Su and Qian Hui Hua, for their encouragement throughout my PhD and imbuing me with a natural curiosity since young. Most importantly, I want to thank my wife, Ada Teo, for her unwavering support and constant encouragement. I could not have done any of this without them.

List of Abbreviations

ASL	Arterial Spin Labelling
AMI	Attention Modulation Index
ANOVA	Analysis of Variance
BBR	Boundary Based Registration
BOLD	Blood Oxygen Level Dependent
CBF	Cerebral Blood Flow
CBV	Cerebral Blood Volume
$CMRO_2$	cerebral metabolic rate of oxygen
CSF	Cerebrospinal Fluid
EPI	Echo Planar Imaging
fCNR	Functional Contrast to Noise Ratio
FFA	Fusiform Face Area
FFX	Fixed Effect
FID	Free Induction Decay
fMRI	Functional Magnetic Resonance Imaging
FMRIB	Oxford Centre for Functional MRI of the Brain
FOV	Field-of-view
FSL	FMRIB Software Library
GE-EPI	Gradient Echo EPI
GLM	General Linear Model
GM	Grey Matter
GRAPPA	Generalized Autocalibrating Partially Parallel Acquisitions
GRASE	Gradient and Spin Echo EPI
HSD	Tukey's Honest Significant Difference
LDC	Linear Discriminant Contrast
LFP	Local Field Potential
MRI	Magnetic Resonance Imaging
MVPA	Multi-Voxel Pattern Analysis
OFA	Occipital Face Area
OLS	Ordinary Least Squares
PET	Positron Emission Tomography
PMC	Prospective Motion Correction

PPA	Parahippocampal Place Area
pRF	Population Receptive Field
PSU	Post Stimulus Undershoot
PVE	Percentage Variance Explained
revPE	Reverse Phase Encoding
RF	Radiofrequency
RFX	Random Effect
RMC	Retrospective Motion Correction
ROI	Regions of Interest
SAR	Specific Absorption Rate
SE-EPI	Spin Echo EPI
SNR	Signal-to-Noise Ratio
SPM	Statistical Parametric Mapping
SVM	Support Vector Machines
TE	Echo Time
TOS	Transverse Occipital Sulcus
TR	Repetition Time
tSNR	Temporal Signal-to-Noise Ratio
UHF	Ultra High Field
VASO	Vascular Space Occupancy
VBR	Voxel Based Registration
WM	White Matter

1 Introduction

1.1 History and Development of functional Magnetic Resonance Imaging (fMRI)

In 1973, Paul Lauterbur shocked the world by generating an image of two glass tubes of ordinary water (H_2O) attached to the inside wall of a larger tube of deuterated water (D_2O), creating the first published magnetic resonance imaging (MRI) image (Lauterbur, P.C., 1973). Since then, the field has developed by leaps and bounds, with MRI coming into common clinical use in 1984. A mere 6 years later, John Belliveau produced the first functional magnetic resonance imaging (fMRI) series (Belliveau et al., 1991). Using the echo-planar imaging (EPI) technique developed by Mansfield (Mansfield, 1977), Belliveau utilized two sequential injections of Gadolinium to generate two maps of cerebral blood volume before and during visual stimulation. The subtraction of the two maps produced the iconic feature image on the cover of the November 1st, 1991 issue of Science.

In 1990, Seji Ogawa demonstrated that MRI can be used to detect changes in blood oxygen level dependent (BOLD) effects in rats (Ogawa et al., 1990) and within the next two years, three independent groups published successful acquisition of BOLD fMRI results, demonstrating task-related BOLD changes in the human brain (Bandettini et al., 1992; Kwong et al., 1992; Ogawa et al., 1992). Each of these landmark papers provided crucial insight into BOLD fMRI. Kwong's paper demonstrated BOLD contrast in the visual cortex with similar dependence on visual stimulation as previously demonstrated with Positron Emission Tomography (PET), proving that the BOLD contrast was indeed reflective of the underlying neural activity. Ogawa's group showed that the BOLD response was dependent on the echo time (TE). This provided further proof that the BOLD response was related to changes in the transverse relaxation of the blood. Last but not least, Bandettini's group showed BOLD activations in the left and right motor cortex independently, showcasing the spatial specificity of BOLD and demonstrated that activations were not simply due to a motion artefact. Together, these papers heralded in a paradigm shift for the usage of MRI scanners; rather than just acquiring structural MRI which provides only anatomic and basic physiological information, the new fMRI sequences are able to produce dynamic time series of brain activation maps quickly and at a relatively high resolution, without the need for invasive procedures.

The number of fMRI papers have seen an explosive growth since 1990 and shows little signs of slowing down. A search on PubMed of papers with "fMRI", "Functional Magnetic Resonance" or "Functional MRI" in the title and/or abstract showed an exponential increase every year (Figure 1-1). While this is not a perfect tally since certain fMRI papers may be omitted due to the terms not appearing in the title and abstract or certain tangential papers might be caught up due to comparisons to fMRI, it is

nonetheless indicative of the overall trend and it is undeniable that fMRI is now a huge part of neuroimaging.

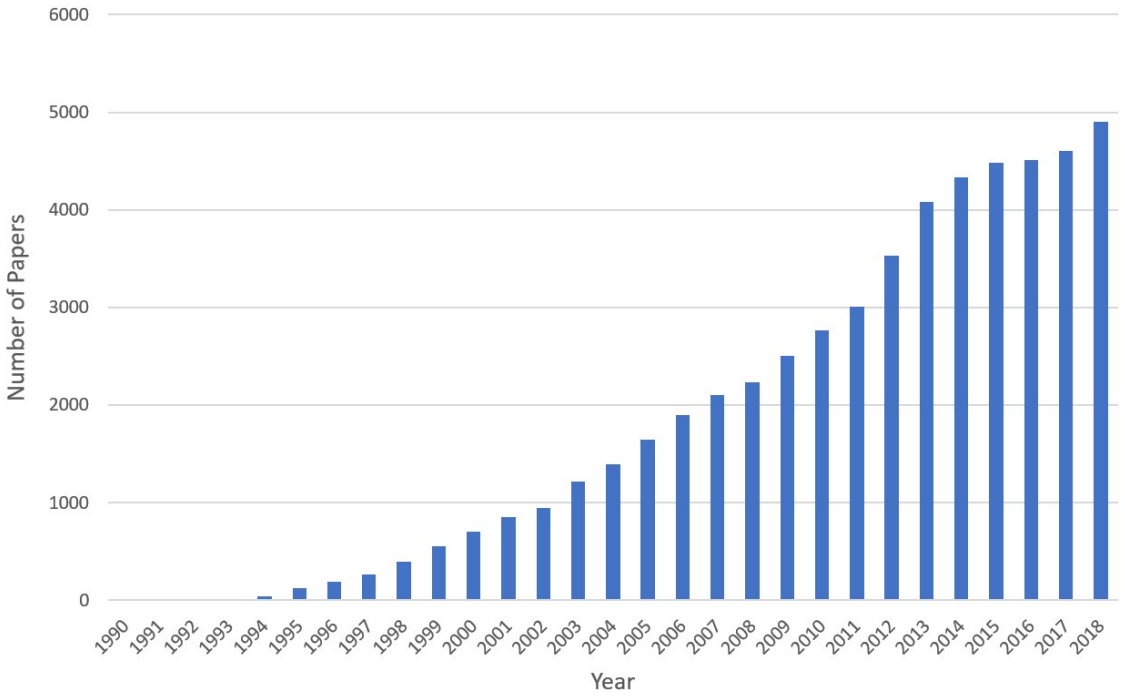

Figure 1-1: A plot of the number of fMRI-related papers published each year according to PubMed. The first fMRI-related paper appeared in 1990.

1.2 Scientific basis for fMRI

40 ### 1.2.1 The Nuclear Magnetic Resonance Signal

An MRI scanner measures the nuclear spin in nuclei and uses that to generate images of the participant. Most atomic nuclei (with the exception of atoms with an even number of both protons and neutrons) have an inherent nuclear spin, which aligns with the external magnetic field. For MRI of the brain, protons (the nucleus of the hydrogen atom) are used as the nuclei of choice due to their abundance in the brain.

Upon entry into the MRI scanner, the strong underlying B_0 magnetic field (1.5/3/7T as specified by the scanner) causes the spin of the protons to align parallel or anti-parallel to the B_0 field. At rest, the majority of the protons align parallel to the field as it is a lower energy state, giving rise to a net macroscopic magnetization in the direction parallel to the B_0 field, which is referred to as the longitudinal magnetization. While aligned to the B_0 field, the spin of the protons also exhibit

precession, rotation in the direction perpendicular to the B_0 field, at the Larmor frequency ω_0, given by the following equation:

$$\omega_0 = \gamma * B_0$$

Equation 1: The Larmor frequency is given by the product of the gyromagnetic ratio, γ, and the strength of the B_0 field.

Here, γ is the gyromagnetic ratio, which is constant for any given nuclei. Thus, importantly, the Larmor frequency is linearly dependent on the strength of the B_0 field. For protons, the Larmor frequency is approximately 128MHz at 3T and 300MHz at 7T. In a pure B_0 field, there is no coherence in the precession of the protons and hence, no net magnetization perpendicular to the B_0 field (transverse magnetization) at the macroscopic level.

To measure the MRI signal, RF pulses are applied to the B_0 field in a rotating manner at the frequency given by the Larmor frequency, also known as the resonance frequency. The component of the RF pulses that is perpendicular to the B_0 field has two net effects on the spin of the protons. Firstly, a proportion of the protons will flip from the lower energy parallel configuration into the higher energy anti-parallel configuration. Secondly, it causes the protons to precess in phase with the radio frequency pulse, and thus in phase with each other. This causes the longitudinal magnetization to decrease while giving rise to a transverse magnetization that rotates in the plane perpendicular to the B_0 field. Depending on the amplitude of the RF pulses, this creates a new macroscopic magnetization at a specific angle from the B_0, commonly referred to as the flip angle. When the radio frequency pulse is removed, the signal will gradually decay over time, a process called free induction decay (FID). The protons will gradually collapse back towards the equilibrium state as they lose energy to the surroundings, causing the longitudinal magnetization to increase back to the original magnitude (T1 relaxation). Similarly, the precession of the protons will gradually dephase due to spin-spin interactions, causing the transverse magnetization to drop back to zero (T2 relaxation). In reality, the transverse magnetization decays faster than what is predicted by T2 relaxation due to magnetic field inhomogeneities (T2* relaxation). It is the relaxation times that are being measured in an MRI image and since different tissue types and different blood oxygenation levels exhibit different relaxation times, they can be differentiated on an MRI scan.

It is often easier to consider the MRI system using a rotating frame of reference, with angular velocity equal to the precession of the protons instead of the laboratory frame. In this rotating frame, the RF pulses are applied in one direction with a constant magnitude and the protons do not precess initially.

Upon application of a gradient, protons in a slightly higher B_0 field precess in the positive direction while protons in a slightly lower B_0 field precess in the negative direction.

In order to generate an image from the MRI signal, each voxel needs to be uniquely identified. This is done via frequency and phase encoding using gradients in different directions and slice selection for 2D acquisitions. There are a multitude of 2D and 3D sequences that can be used, with their individual advantages and disadvantages. For the purposes of this thesis, I will be focusing on 2D GE-EPI (gradient echo EPI) sequence (Stehling et al., 1991) since it has been employed in both 3T and 7T scanners to good results (Lawrence et al., 2019; Polimeni et al., 2010; Todd et al., 2016).

1.2.2 The 2D GE-EPI sequence

For 2D GE-EPI, prior to the application of the RF pulse, a gradient is first applied to the magnetic field in the direction perpendicular to the slices (z-axis). By doing so, each position along the z-axis would have a slightly different Larmor frequency. Thus, by applying a pulse with a specific frequency, all the protons from one of the slices can be selectively activated. To accurately identify the source of each signal, frequency encoding is employed along the x-axis while phase encoding is employed in the y-direction. Frequency encoding is achieved by applying a constant gradient (G_x) along the x-axis. This would cause protons to precess at varying frequencies, ω, given by the following equation:

$$\omega = \omega_0 + \gamma * G_x * x$$

Equation 2: Equation describing how the frequency varies along the x-axis

For phase encoding, a gradient (G_y) is applied along the y-axis for a short period t, thus resulting in the protons precessing at the same angular velocity during acquisition but with slightly different phase, ϕ, which is described by the following equation.

$$\phi = \gamma * G_y * y * t$$

Equation 3: Equation describing how the phase varies along the y-axis

Thus, each voxel in space is uniquely specified by slice selection and a unique pair of phase and frequency values.

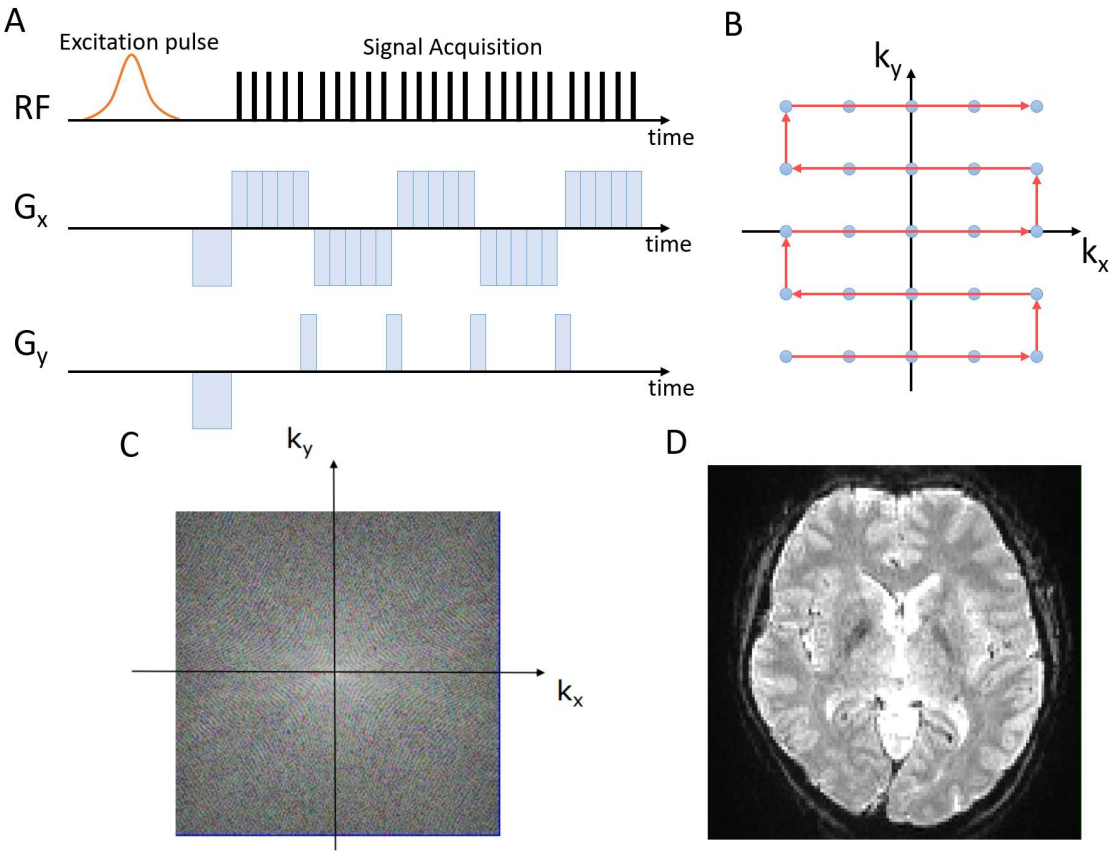

Figure 1-2: Panels A and B show a simplified illustration of a Cartesian EPI acquisition. Panel A illustrates the changes in gradients applied over time while Panel B illustrated the trajectory of the sampling in k-space. Panel C shows a sample k-space image, which is then Fourier transformed to generate the reconstructed image in Panel D.

In order to reconstruct the MRI image, researchers need to first generate the k-space image. The k-space image is the 2D (or 3D) Fourier transform of the MRI image in the frequency domain. Each point in k-space is sampled during the MR sequence and the resultant image undergoes Fourier transform to reconstruct the MRI image. For EPI sequences, this is done by sampling each point in the k-space in a continuous fashion after one RF excitation. There are various methods to traverse the k-space, with a zig-zag Cartesian pattern being the standard method (illustrated by Figure 1-2, Panels A and B), though some groups have shown success with spiral EPI or other non-cartesian trajectories (Glover, 2012; Wright et al., 2014).

120 Once the k-space image (Figure 1-2, Panel C) is acquired, a 2D Fourier transform is applied to generate the reconstructed image (Figure 1-2, Panel D). This means that the properties of the k-space image determine the properties of the reconstructed image. The inverse of the sampling interval determines the field of view of the reconstructed image while the inverse of the width of the k-space image

determines the resolution of the reconstructed image. It is important to note that the usage of the Fourier transform from the raw data to the final image means that simple motion correction on the final image would be insufficient to address all the artefacts that arise from motion between the RF pulse and image acquisition. Any inaccuracies in acquiring a single point in k-space would affect the entire image.

1.2.3 Going from MRI to fMRI

The difference between structural MRI and fMRI is akin to that of the differences between a photograph and a video. Structural MRI obtains a single image of the entire brain volume at a high resolution while fMRI obtains a time-series of images of the brain, but often at a lower resolution (for the same field strength).

Prior to the implementation of EPI, the time taken to acquire a single volume was extremely long. As such, the main usage of MRI scanners revolved around structural MRI, where a single volume is acquired over the course of a few minutes and analysed. In fact, this is still the primary purpose that clinical scanners are being used for today. With the advent of EPI (Stehling et al., 1991) and other acceleration techniques (GRAPPA (generalized autocalibrating partially parallel acquisitions, Kiefer et al., 2002), partial Fourier (McGibney et al., 1993) and multiple other methods (Feinberg and Yacoub, 2012)), a full brain volume can be acquired in a matter of seconds, albeit at the expense of lower resolution. By acquiring volumes in rapid succession, researchers are able to obtain a time series of the behaviour of the brain, allowing for the detection of changes in the brain in real-time. By utilizing the BOLD effect as described in the next section, this allows researchers to stimulate the brain in real-time and utilize the fMRI time series to observe which sections of the brain respond to the stimulus.

1.2.4 Neurological Basis for the BOLD effect

One of the cornerstones of fMRI research is the BOLD effect (Ogawa et al., 1992). The BOLD effect measures the hemodynamic response of the brain, which ties the fMRI signal changes to neurological activities. This allows us to make inferences about brain activity based on changes in the fMRI signal. While the exact causal link between neurological activity and the subsequent hemodynamic response is not fully understood nor quantified, there has been numerous studies that demonstrate that BOLD changes is indeed related to the neural activity (Logothetis et al., 2001; Ogawa et al., 2002; Rees et al., 2000). Rees et al., 2000 compared the behaviour of the middle temporal region in human fMRI measurements and electrophysiological data from single-unit recordings in monkeys to demonstrate that the BOLD response and the average neuronal firing rate exhibits a linear relationship. Logothetis

et al., 2001 carried out simultaneous intracortical recording of neural signal and fMRI and demonstrated a strong correlation between local field potential (LFP) and the BOLD signal.

To the best of our understanding, the biological mechanism that drives the BOLD effect arises because all neural activity, ranging from propagating action potentials along the axons to releasing of
160 neurotransmitters across synapses, all require energy. When a brain region is activated during a cognitive task, the increase in neural activity causes an increase in energy consumption, which is turn increases the cerebral metabolic rate of oxygen ($CMRO_2$) in that specific brain region. Through neurovascular coupling, this also generates an increase in blood flow through vessel dilation. It is this increase in blood flow, specifically oxygenated blood, that gives rise to the BOLD signal.

The research for the exact link between the hemodynamic response and neural activity is still an on-going one. There is a general consensus that BOLD is linked to LFP rather than spike rate. Viswanathan and Freeman, 2007 utilized a stimulus that elicits synaptic activity but without spiking activity to demonstrate that the BOLD signal is a reflection of LFP, not spike rate. Magri et al., 2012 showed that not only does BOLD signal correlate to specific bands of LFP frequencies, but the amplitude and latency of the BOLD signal reflects relationships between the power levels of the alpha, beta and gamma LFP frequency bands. On the other hand, a model analysis by Tyler et al., 2015 suggests that the form of the BOLD response is more compatible with the energetics of the primary neural activation than the LFP waveform.

1.2.5 Timecourse of the BOLD effect

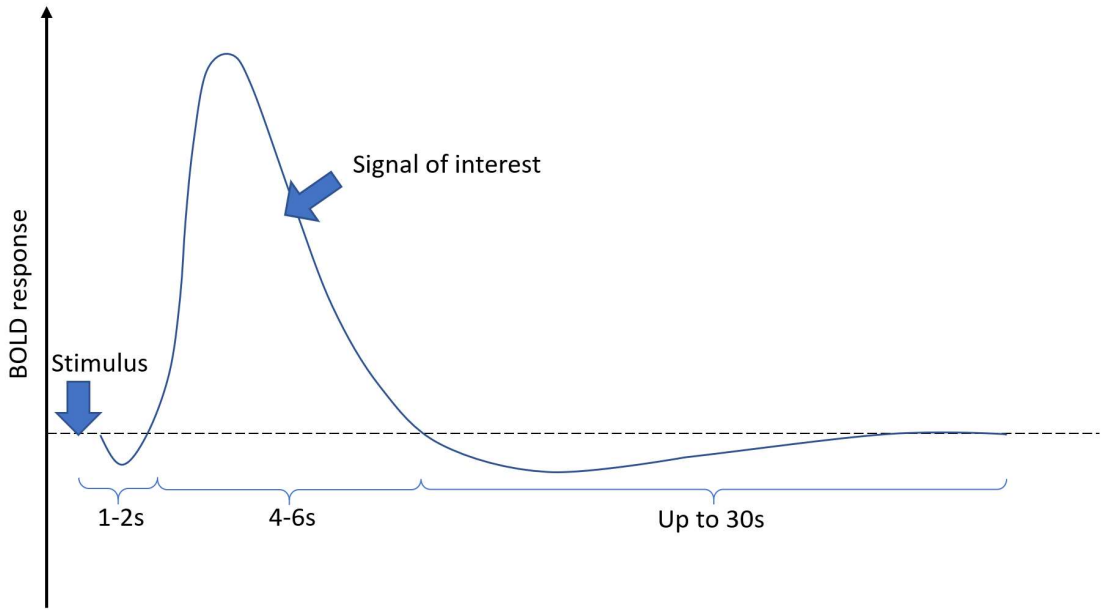

Figure 1-3: Illustration of a typical BOLD response to an event-related stimulus.

While the exact causal link is still an unanswered question, the timecourse of the BOLD response has been well characterized (Figure 1-3). At the start of neural activity, an initial dip at one to two seconds has been reported (Hu et al., 1997; Kim et al., 2000; Yacoub and Hu, 2001), corresponding to a transient increase in deoxyhemoglobin seen in optical studies (Malonek and Grinvald, 1996). While this effect is much smaller than that of the standard BOLD increase and not necessarily always present or detectable (Buxton, 2001; Lindauer et al., 2001), it is interesting because the initial dip has been shown to have better spatial and temporal localization relative to the standard BOLD increase (Kim et al., 2000; Malonek and Grinvald, 1996). This effect is theorized to reflect a rapid increase of $CMRO_2$ prior to the increase of cerebral blood flow (CBF), hence explaining the better localization.

Approximately three seconds after the stimulus presentation, a large increase in BOLD signal is observed. This is the main signal of interest measured in most fMRI studies and has a temporal width of four to six seconds (Bandettini et al., 1992) for event-related stimuli. It is important to note that this response has substantial temporal and spatial variations depending on the type and length of stimulus presentation (Birn et al., 2001; Friston et al., 1998; Vazquez and Noll, 1998). For longer stimulus of more than five seconds, the BOLD response will begin to plateau out (Miller et al., 2001).

After the positive BOLD signal, there is a post-stimulus undershoot (PSU) that lasts up to 30s depending on the stimulus duration (Chen and Pike, 2009; Hirano et al., 2011). The source of PSU has been a matter of great interest. Recent studies (Dechent et al., 2011; Poser et al., 2011) show cerebral blood volume (CBV) and CBF changes provide little to no contribution to the PSU and suggests $CMRO_2$ as the main source of PSU. Sadaghiani et al., 2009 and Donahue et al., 2009 demonstrated changes in the PSU independent of CBF changes. Zong and Huang, 2011 demonstrated that the ratio of positive BOLD and PSU remained constant in both micro- and macrovascular regions, hence suggesting that the PSU is not dependent on CBV. Hua et al., 2011 estimated the relative contributions of CBV changes and $CMRO_2$ to be 19.7±15.9% and 78.7±18.6%, respectively based on their experimental data. However, $CMRO_2$ does not provide the complete picture as it does not explain the variation in PSU due to stimulus variation. Some studies (Hirano et al., 2011; Kim and Kim, 2011) suggest that delayed vascular compliance is a better explanation, mainly because the venous response is slower and only visible after longer stimulation, potentially providing an explanation to the stimulus-duration dependence behaviour of the PSU.

1.2.6 Measuring the BOLD effect

Changes in the BOLD signal are detected by MRI scanners due to the difference in magnetic susceptibility of oxyhaemoglobin and deoxyhaemoglobin. Oxyhaemoglobin (haemoglobin bonded with oxygen molecules) has zero magnetic moment, making it diamagnetic (Pauling and Coryell, 1936).

This means that when oxyhaemoglobin is exposed to an external magnetic field (i.e. in the MRI scanner), it creates an induced magnetic field in the opposite direction. In contrast, deoxyhaemoglobin (haemoglobin without bound oxygen molecules) is paramagnetic and forms internal, induced magnetic fields in the direction of the external magnetic field. This arises due to the presence of unpaired electrons in the iron atoms in haemoglobin. These unpaired electrons have a magnetic dipole moment due to their spin and align parallel to the applied field, generating a net attraction.

The large difference in magnetic susceptibility between deoxyhaemoglobin and the surrounding tissue leads to a susceptibility-induced perturbation of the magnetic field around blood vessels, predominantly veins and capillaries. This perturbation leads to increased dephasing of the proton signals relative to each other (since each proton now precesses at a different frequency which corresponds to their local magnetic environment). This increase in dephasing effect is reflected in a faster T2* relaxation and hence, picked up by the MRI scanner in the form of lower signal intensity.

1.3 The Need for Higher Field Strengths

While conventional 1.5T and 3T scanners are generally more than sufficient for structural acquisitions and looking at activations at the level of region of interests (ROIs), However, at field strengths of 3T or below, it is extremely difficult to obtain sub-millimetre resolution images while maintaining a reasonable signal-to-noise ratio (SNR). While sub-millimetre resolution has been achieved at 3T, these acquisitions require a high degree of sequence manipulation, longer repetition time (TR), increasing slice thickness, etc. Furthermore, the relaxation times of tissue also change with the field strength, allowing for better contrast at higher field strengths. Thus, by going to 7T, there is approximately a six-fold increase in signal strength, allowing us to acquire at submillimetre resolution with reasonable TR and good SNR.

One of the main motivations for sub-millimetre images is to improve our understanding of brain functionality, especially with regards to the behaviour of individual cortical columns and layers. The thickness of the cortex varies from 2mm to 5mm depending on the brain region, so sub-millimetre resolution is needed to resolve individual cortical layers. The neuroanatomy of individual cortical layers has been well studied in non-human primates(Markov et al., 2014; Rockland, 2017; Rockland and Virga, 1989), with different layers exhibiting different connections. Feedback neurons have been shown to terminate in superficial and deep layers, while bottom-up feedforward neurons generally terminate in the middle layers. Thus, by probing the laminar origin of different fMRI effects,

researchers would be able to make inferences about the nature of the effect (bottom-up representations vs top-down modulations).

1.4 Challenges of UHF fMRI

However, while ultra-high field fMRI is able to increase the attainable resolution, the higher field strengths also generate additional problems that need to be addressed in order to utilize the data. These problems include higher susceptibility to subject motion, increased magnetic field inhomogeneities and superficial bias when carrying out laminar analyses.

1.4.1 Subject Motion

Subject motion is a huge confound in all of MRI (Andre et al., 2015), resulting in striping, blurring and other artefacts which degrades the image quality. As the MRI image is generated from the Fourier transform of the acquired k-space data, any motion could potentially affect every voxel in the image. Intra-volume motion can result in amplitude and phase inconsistences in k-space, leading to distortions and ghosting in the data (Jezzard and Clare, 1999) while through-plane motion for 2D acquisitions would result in fluctuations in signal intensity as the hydrogen nuclei have a different spin history from what was expected (Friston et al., 1996). Moreover, in partial volume acquisitions, motion can cause the acquisition box to shift relative to the brain, resulting in edge voxels being lost.

Similar to other applications of MRI, fMRI acquisition is also highly sensitive to motion. This is further compounded by the time-sensitive nature of fMRI data. Once the data at a certain time point in an fMRI experiment is lost or compromised due to motion, it would be impossible to recover it unless the entire acquisition and experimental sequence is repeated. Moreover, fMRI data processing requires accurate realignment of volumes across the time series as most fMRI analyses implicitly assume that the same voxel corresponds to the same location throughout the session. This assumption is invalidated by motion and could result in missed effects or false positives (Field et al., 2000; Schulz et al., 2014)

These problems are further exacerbated by the smaller voxel sizes in higher resolutions, as the magnitude of the motion increases relative to the size of the voxel. For example, a displacement of 1mm between scans is a small issue at 3mm isotropic resolution, since 66% of the voxel's contributions remains constant. In contrast, a 1mm movement between scans will result in an entirely different voxel being imaged at 0.8mm isotropic. Sub-millimetre scans also generally have longer TRs, which

worsens the problem since the longer time window between consecutive scans would result in greater displacements for movement of the same velocity.

All of the aforementioned problems can negatively impact the image quality, and potentially mask any benefits from going to the higher field strength (Freire and Mangin, 2001; Yakupov et al., 2017). These problems can be mitigated at two different stages, during the scan acquisition and during post-processing stage and are addressed in Section 1.5.

1.4.2 Magnetic Field Inhomogeneities

While scanner manufacturers are able to generate a nearly perfect homogenous magnetic field for an empty scanner through both active and passive shimming, the act of placing an object or a participant in the main magnetic field introduces regions of varying magnetic susceptibility. This generates inhomogeneities in the magnetic field, especially near junctions between regions of very different magnetic susceptibility. In turn, these inhomogeneities causes geometric image distortions which scale linearly with field strength, and thus, are more severe at higher field strengths.

Moreover, most BOLD fMRI methods utilized sequences with long echo times (compared to structural MRIs) and these methods are especially susceptible to signal loss due to intra-voxel dephasing (which arises due to the field inhomogeneities). In addition, the echo time can also be affected and cause spatially varying BOLD sensitivity (Josephs et al., 2002).

1.4.3 Superficial Bias

GE-EPI sequences have been widely used for fMRI studies due to their simplicity and high SNR. However, GE-EPI is also most susceptible to large draining veins in the brain (>10um) (Boxerman et al., 1995). This means that the GE-EPI sequence not only picks up the changes in deoxygenated blood arising from the neuronal activation within voxel itself, it also detects the changes in deoxygenated blood being carried in the draining veins from the deep layers of the brain to the surface. Thus, this leads to lower specificity and a superficial bias in the raw data (Fracasso et al., 2018; Yacoub et al., 2013). This can be a substantial confound for laminar analysis and can potentially end up masking real laminar effects.

1.5 Methods for Improving Data Quality

To address the aforementioned problems, multiple methods have been implemented and evaluated. Here, I give a brief overview of all the available methods and highlight the four methods that I will

evaluate in this thesis. The methods are sorted according to when they are implemented along the acquisition and processing timeline.

1.5.1 Data Acquisition

At the level of data acquisition, there are two main avenues of improving data quality: modifying the acquisition sequence and prospective motion correction (PMC).

Besides the conventional GE-EPI, spin echo EPI (SE-EPI) and gradient and spin echo EPI (GRASE) sequences have also been implemented for high resolution fMRI (Kemper et al., 2015; Yacoub et al., 2013).These sequences are primarily susceptible to the effect of capillaries, instead of draining veins, and thus, increases specificity and reduces superficial bias. However, these sequences come with a trade-off of lower SNR and higher specific absorption rate (SAR) due to the additional RF pulse present in the spin-echo sequence. Recently, there have also been a whole host of new fMRI techniques for high resolution fMRI, such as vascular space occupancy (VASO) (Huber et al., 2017b; Lu et al., 2013) which measures cerebral blood volume (CBV) and arterial spin labelling (ASL) (Huber et al., 2017b; Kashyap et al., 2019; Petcharunpaisan, 2010) which measures cerebral blood flow (CBF). While these methods are able to remove the spatial blurring due to draining veins, there are other problems associated with these sequences, such as the largest CBV changes being localized in the arteries and potential retrograde dilation in the upper layers relative to the location of neuronal activation (Uludağ and Blinder, 2018). Similar to GRASE, these methods also tend to have less sensitivity as a trade-off for their higher specificity (Huber et al., 2017b). These alternatives also require more complex scan sequences, and thus, will not be covered in this thesis.

PMC is a method of correcting for subject motion that has been gaining traction in recent years (Engstrom et al., 2015; Huang et al., 2018; Stucht et al., 2015). In PMC, the movement parameters of the participant's head are acquired concurrently with the acquisition of the imaging volume(Callaghan et al., 2015; Maclaren et al., 2012). These movement parameters are then used to update the position of the acquisition box within the participant's head prior to each RF pulse. This ensures that the same volume is being scanned regardless of the amount of participant motion. Maclaren et al., 2013 and Zaitsev et al., 2016 provide a succinct summary on the current state of the field and list the most promising techniques, some of which have demonstrated significant benefits to data quality relative to RMC (Muraskin et al., 2013; Stucht et al., 2015; Todd et al., 2015). The estimation of PMC parameters can be done by either using the internal MR data or external tracking modules. Internal MR data methods, such as k-space navigators (Van Der Kouwe et al., 2006; Ward et al., 2000) or fat-based navigators (Engstrom et al., 2015), require additional scans between each acquisition, which would reduce the temporal resolution of the data further. Meanwhile, external tracking modules,

including the optical system evaluated in this thesis, utilize a secondary system to acquire the positional data in real time and transfer the data to the scanner. This method has the benefit of adding little to no scanning time while still allowing for real-time correction of participant motion. In Chapter 3 of this thesis, I present a project testing the impact of PMC on fMRI data with minimal participant motion.

1.5.2 Post Processing

While initially developed for diffusion imaging, previous fMRI studies have shown that TOPUP correction is able to reduce the susceptibility-induced distortions (Andersson et al., 2003; Smith et al., 2013). To carry out TOPUP, a few fMRI volumes are collected with the same scan parameters except for reversing the phase encoding direction. This results in images with distortions going in the opposite direction compared to the main EPI images. By comparing the reverse phase encode images with the main EPI images, TOPUP is able to estimate the susceptibility-induced off-resonance field, which when applied to the raw images will maximize the similarity of the unwarped images. This correction is then applied to the entire fMRI time series to reduce the distortions. Given that TOPUP has already been widely adopted for distortion correction (Glasser et al., 2013; Smith et al., 2013), I will not explore alternatives for distortion correction in this thesis. TOPUP will be applied for all 7T analysis in this paper.

RMC also helps to correct for participant motion, regardless of whether PMC was employed in the acquisition stage. RMC has seen widespread use due to the simplicity of use and benefits on the data. In RMC, rigid body transformations are applied to each volume post-scan to align all acquired volumes to the same scan (Ashburner and Friston, 2003; Johnstone et al., 2006). Conventional implementations of RMC drive realignment using a cost function relying on per-voxel sum-of-square differences in intensity. In Chapter 6 of this thesis, I also present an alternative realignment cost function utilizing BBR (Greve and Fischl, 2009) and compared it against conventional realignment techniques.

1.5.3 Data Analysis

At the level of data analysis, multi-voxel pattern analysis (MVPA) methods have been gaining traction as they have been shown to be more sensitive and robust relative to commonly used univariate, voxel-wise, techniques (De Martino et al., 2008; LaConte et al., 2005; Mahmoudi et al., 2012; Misaki et al., 2010). In addition, the abstraction offered by MVPA methods also allows for comparisons across modalities (Kriegeskorte, 2008) and even species (Kriegeskorte et al., 2008). Multivariate approaches compare the pattern of activations across conditions, rather than a voxel-by-voxel or mean activation comparison utilized in univariate approaches. This results in greater statistical power for multivariate approaches while also providing information about mean differences and correlations between

conditions. Moreover, cross-validation approaches allow for higher robustness against noise and better reproducibility checks.

MVPA is a broad category and there are also multiple different techniques that can be employed for fMRI studies. For the scope of this thesis, I looked at two main techniques, support vector machines (SVM) and linear discriminant contrast (LDC). SVM (Cortes and Vapnik, 1995) utilizes the data points from the training data that are closest to the boundary between the two conditions as support vectors, hence the name. These support vectors are used to construct a hyperplane to separate the two conditions of interest and the validity of this hyperplane is tested by cross-validating on a separate set of independent testing data. SVM is one of the most widely used methods due to simplicity of application and ease of understanding. However, SVM does have a few shortcomings, including discretization of results, ceiling effects and rigid decision boundaries. This is discussed in further detail in Chapter 4.

I also presented cross-validated Linear Discriminant Contrast (LDC) (Kriegeskorte et al., 2007; Walther et al., 2016) as another MVPA technique. LDC is a continuous statistic derived from Fisher's linear discriminant. Similar to conventional linear discriminant analysis, it utilizes the training data to generate a set of representative weights for all voxels to maximize the distance between the two conditions. These weights are then applied to the testing data to form the LDC, which essentially measures the reliability of the difference between the two conditions across the training and testing data. This measure is also known as the cross-validated Mahalanobis (crossnobis) distance (Kriegeskorte and Diedrichsen, 2016). A detailed comparison of the two MVPA methods on real and simulated fMRI data is present in Section 4 of this thesis.

1.6 Summary

The field of fMRI is constantly evolving, with researchers constantly pushing towards higher field strengths, smaller voxel sizes and better image quality. We are at an exciting time in fMRI, with 7T scanners and new methods allowing us to see submillimetre data with much more clarity than before, enabling us to look at laminar and columnar profiles of various regions of interest.

However, it is important to ensure that the data quality is sufficient to support the neuroscience questions that researchers are trying to answer. To this end, I have explored various methods of improving data quality at both 3T and 7T in this thesis. For Chapters 3 and 4, I utilized a simple visual grating fMRI experiment to evaluate the effectiveness of PMC and compare two MVPA methods

respectively. For Chapters 5 to 7, the analysis was done on a visual attention task. I compared the quality of data obtained at 3T against 7T in Chapter 5 to examine the benefits of going to higher field strengths. In Chapter 6, I examined the effectives of using BBR to drive RMC realignment compared to standard voxel based methods. Finally, in Chapter 7, I examined ways to remove the superficial bias present in 7T GE-EPI data and test their effectiveness on 7T laminar data.

2 General Experimental Methods

2.1 Stimulus Design

For this thesis, I employed two overarching visual experiments. For Chapters 3 and 4, I utilized simple visual gratings experiment while for Chapters 5 to 7, I employed a visual attention task. In the present section, I described the stimuli design for both experiments.

2.1.1 Visual Gratings Experiment

The visual gratings experiment was chosen due to two main reasons. Firstly, the effect has been well-characterized and shown to be robust across participants (Alink et al., 2013; Kamitani and Tong, 2005; Tong et al., 2010) and thus, can be used to compare the various motion correction methods. Secondly, the presence of radial bias generates activations across different spatial scales (Freeman et al., 2013; Tong et al., 2010), allowing me to determine the impact of PMC across different spatial scales.

The visual gratings experiment included main experimental runs and retinotopic localizer runs. All stimuli for both runs were created using Matlab (2009a, The MathWorks, Natwick, MA, USA) and presented in the scanner using Presentation (v17.2), All stimulus types were presented within an annulus (inner radius = 1.05^{o}, outer radius = 7.15^{o}).

Main Experimental Runs

For the main experimental runs, two orientations of gratings (45^{o} clockwise or 45^{o} counter-clockwise from the vertical) were presented within each run (Figure 2-1, Panel A). Each run was divided into four sub runs, which contained eight 16s stimulus blocks each. Stimuli from each orientation were presented in alternating blocks, with the leading orientation randomized evenly across sub runs. Within each block, the 20 phase-shifted stimuli of one orientation were presented in a randomized order at a frequency of 2 Hz. Each stimulus was presented for 250ms, followed by 250ms of fixation on a blank screen. There was an 8s fixation period between each block and a 24s fixation period between each sub run. This helps to ensure that estimates obtained from each sub run are independent from each other. Uniform gratings at 45^{o} from the vertical were used as they are balanced about both vertical and horizontal orientations. Thus, a global preference map for these orientations will yield an equal global activation pattern for each grating (Furmanski and Engel, 2006; Seymour et al., 2010). The gratings were designed with a spatial frequency of 1.25 cycles per visual degree, which has been shown to strongly drive neural responses in primary visual cortex, V1 (Henriksson et al., 2008). V1 is located in the occipital lobe, in and around the calcarine fissure. For

each orientation, 20 stimuli were generated with varying spatial phases uniformly distributed between 0 and 2π.

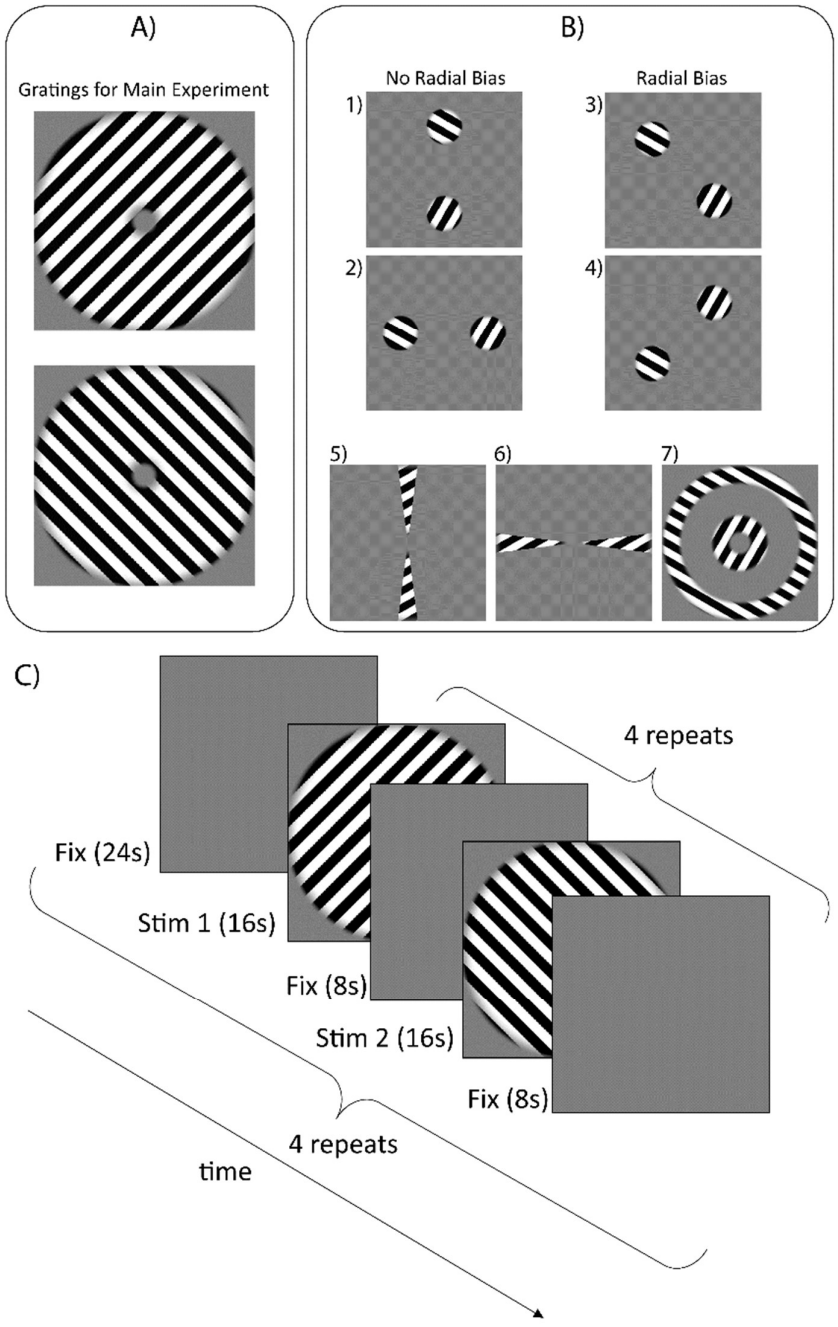

Figure 2-1: A) Uniform gratings of two different orientations (both 45° from the vertical) were used as stimuli for the main experiment. B) The seven stimuli were presented in a randomized block order during localizer scans. Stimuli 1 and 2 were used to isolate regions with no radial bias, Stimuli 3 and 4 were used to isolate regions with radial bias and stimuli 5, 6 and 7 were used to segment V1. C) An illustration of the timecourse of stimuli presentation for the main experiment. The two 16s stimulus blocks (one for each orientation) were repeated four

times each for a total of eight stimulus blocks per sub-run. The entire sub-run was repeated four times for each scan, with a gap of 24s fixation between sub runs to minimise the dependency between sub-runs.

Retinotopic Localizer Runs

The retinotopic localizer runs were designed to define all of V1 and V1 subregions with and without radial bias. I presented seven groups of dynamic gratings stimuli (Figure 2-1, Panel B) designed to optimally drive responses in selective regions of the early visual cortex: (1, 2) a patch pair stimulus consisting of two circular patches (spanning 2.40°–5.80° eccentricity) lying along the vertical or the horizontal axis, respectively; (3, 4) a patch pair stimulus identical to the previous but lying along the two diagonals, respectively; (5) a horizontal double-wedge stimulus, spanning a polar-angle range of ±15° around the horizontal meridian; (6) a vertical double-wedge stimulus of the same kind; (7) a 1.5°-wide ring peripherally surrounding the main-experimental stimulus annulus (5.65°–7.15° eccentricity), and a 1.5°-wide ring inside the annulus (1.05° –2.55° eccentricity). Each stimulus group contained linear gratings with a spatial frequency of 2Hz. Within each stimulus group, there were twelve orientations of the gratings with angular steps of 30° and within each orientation, there were four different spatial phases uniformly distributed between 0 and 2π. The stimuli were presented in 13s blocks at a frequency of 2Hz. Within each block, a random stimulus from the group was presented for 250ms and followed by 250ms of fixation. There was a total of eight blocks for each of the four patch pair stimuli and four blocks for each of the other stimuli. The order of the blocks was randomized within each run and there were a total of 2 runs per participant per session.

For both experimental and localizer runs, participants were instructed to fixate on a central blue dot (diameter:0.1° visual angle) for the entire run. At random intervals during the run, the dot turned green for 250ms at an average rate of once per 3.5s (with a minimum gap of 1.5s between consecutive changes). Participants were tasked to respond to every colour change by pressing a button on their right index finger. This helped to encourage participants to fixate on the center of the screen and also allowed us to remove participants that were not attending to the stimuli properly. I calculated the task accuracy by dividing the number of flashes that the participant responded to within 2s by the total number of flashes and excluded all participants with lower than 50% response accuracy from further analysis. The low accuracy indicates that the participants were not fixating and could potentially have drifted off to sleep.

2.1.2 Visual Attention Experiment

The visual attention experiment was utilized for the subsequent experiments as it activated both early and higher visual areas and thus allowed me to analyse multiple ROIs. Contrasting the four different

condition blocks also allowed me to observe for spatial and categorical selectivity individually while the four stimuli conditions allowed me to observe for the effect of distractors and non-specific task activations.

For the visual attention experiment, I had four different types of experimental runs, population receptive field (pRF) retinotopic localizer runs and categorical localizer runs.

Main Experimental Runs

For the main experiment, I had four different task types that was permutated at the run level: task with distractor present (TaskD+), task with distractor absent (TaskD-), fixation with distractor present (FixD+) and fixation with distractor absent (FixD-). Conditions involving the presence of distractors were alternated between runs, while the context of the task was permutated across sessions (i.e. participants attended one session with alternating runs of FixD+ and FixD- and another session with alternating runs of TaskD+ and TaskD-).

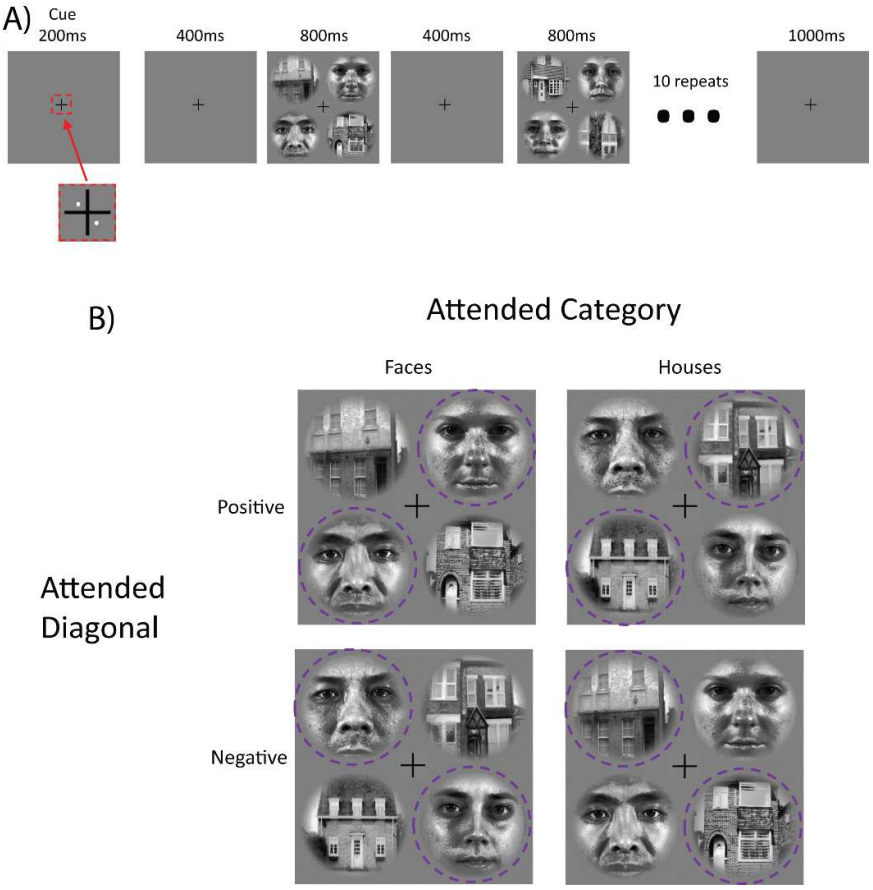

Figure 2-2: Panel A shows the experimental paradigm for each trial block. An initial pair of white dots cued participants to attend to a specific diagonal at the beginning of each task block. Ten image pairs from one category (faces or houses) appeared sequentially along the attended diagonal while image pairs from the other category appeared along the other diagonal. 'Different' cases appeared on 50% of trials. Panel B illustrates the 4 main stimuli conditions adopted. The purple dotted circle indicates the attended regions and do not appear to the participant.

Within each run, I permutated the attended location and category independently to generate four types of condition blocks (Figure 2-2, Panel B): attending to houses present in the two circular patches at 45° and 225° from the vertical (H^{45}), attending to houses present in the two circular patches at 135° and 315° from the vertical (H^{135}), attending to faces present in the two circular patches at 45° and 225° from the vertical (F^{45}) and attending to faces present in the two circular patches at 135° and 315° from the vertical (F^{135}). For simplicity, I refer to attending to the patches at 45° and 225° from the vertical as attending to patches along the positive diagonal and attending to the patches at 135° and 315° as attending to the negative diagonal. A total of 20 blocks (5 blocks of each condition) were presented during each run of the main experiment in a randomized order. At the start of each block, two white dots (visual angle = 0.18° (3T) or 0.10° (7T)) appear for 350ms indicating the diagonal along which that

the participant is tasked to attend to. This is followed by 550ms of fixation. The stimuli then appeared for 950ms. In the task condition, the participant is required to do a same-different judgement (50% chance of either occurring) between the two stimuli, followed by 550ms of fixation. This stimuli-fixation couple was repeated for a total of 10 times within each block and a rest block of fixation with minimum 1000ms was presented between each block. In the distractor absent condition, the stimuli screen only consists of two stimuli from the attended category appearing in the attended regions while in the distractor present condition, two additional stimuli from the other category appeared in the non-attended regions. Within each session, there were a total of four runs with distractors present and four runs without distractors and they were ordered in an alternating fashion.

The two fixation conditions were identical to the task conditions. However, instead of carrying out a same-different judgement, participants were tasked to focus on the fixation cross and respond to whether the fixation cross rotated 45° or remained unchanged (50% chance of either occurring). For all conditions, participants were required to respond after each trial.

All stimuli were created using Matlab (2009a, The MathWorks, Natwick, MA, USA) and presented in the scanner using Presentation (v17.2). Stimuli from the respective categories were presented in a circular patch at four locations, diagonally from the fixation cross at 45°, 135°, 225° and 315° and spanning 0.26°-3.87° eccentricity at 3T and 0.16°-2.42° eccentricity at 7T. At 3T, the stimuli were centred at the middle of the screen while the stimuli setup was shifted up from the centre of the screen by 2° in the 7T scanner due to visual obstruction of the lower segment of the screen by the head coil. Within each stimuli category (houses and faces), there were a total of 20 stimuli that can are selected from at random at each presentation. All images were presented in greyscale and histogram matched across the board to ensure both luminance and root mean squared contrast is identical for all images. This prevents any decoding due to mismatch of brightness or contrast.

pRF Retinotopic Localizer Runs

For each participant, I carried out six runs of a pRF retinotopic localizer, using the stimuli and code provided on http://kendrickkay.net/analyzePRF/ and described by Dumoulin and Wandell, 2008 and Kay et al., 2013. All stimuli were presented within a circle of radius 5.72°. The pRF retinotopic localizer works by utilizing moving bars, wedges or rings as masks to reveal an underlying pattern consisting of various coloured objects at multiple spatial scales on a pink-noise background. This was designed to drive both low-level and high-level visual areas. The underlying pattern changed at a rate of 15Hz

between 100 different randomized patterns. The masked regions were entirely mid-grey. I carried out three runs of multibars and three runs of wedges and rings, presented in alternating order.

For the multibar runs, there was a 16 second rest at the start of the run. This was followed by a bar revealing the underlying pattern sweeping from left to right in 28 seconds and a 4 second rest after that. This bar-rest combination was repeated seven more times, with the bar sweeping from bottom to top, right to left, top to bottom, bottom left to top right, bottom right to top left, top right to bottom left and top left to bottom right in that order. There was a 12 second rest after the top to bottom sweep and a 16 second rest at the end of the run. The bar took 28 seconds to sweep across the entire circle and had a width of 98 voxels, approximately 0.73°.

For the wedges and rings runs, there was a 22 second rest at the start and end of the run. This was followed by 2 full counter-clockwise revolutions of a quarter-circle wedge at 32 seconds per complete revolution. Next, there were 2 runs of expanding rings with a 4 second rest after each presentation. The expanding rings took 28 seconds to expand from the central dot to pass the limits of the circle. 2 full clockwise revolutions of a quarter-circle wedge at 32 seconds per revolution followed that. Lastly, there were 2 runs of the contracting rings with a 4 second rest after each. Similar to the expanding rings, the contracting rings took 28 seconds per run going from the limits to the circle to shrinking into the central dot.

For further details on the experiment and movie illustrations of the stimuli, please refer to http://kendrickkay.net/analyzePRF/. Throughout the experiment, the participants were instructed to focus on a dot at the centre of the screen. The dot underwent random colour changes between red, white and black and the participant was instructed to respond to every colour change by pressing a button with their right index finger. The interval between colour changes was randomly and evenly distributed between 1 to 5 seconds.

Categorical Localizer Runs

I carried out 4 runs of the category-selective localizer task, which is comprised of 5 different block presentations of faces, scenes, objects, scrambled objects, and fixation. Each of these 5 block types appeared 4 times per run in a randomized order. For each 16-second block, 20 random stimuli from the current category were presented consecutively for 800ms each. Participants carried out a 1-back matching task while fixating on a black dot in the middle of the screen.

2.2 Acquisition Methods

2.2.1 3T Prisma Scanner

All of the 3T data presented in this thesis was acquired on the Siemens 3T Prisma-Fit scanner at the MRC Cognition and Brain Sciences Unit, University of Cambridge with a 32-channel head coil. Visual presentation of the stimuli was presented on a 48-inch LCD screen at the head of the MRI scanner.

2.2.2 7T Terra Scanner

The 7T data presented in this thesis was acquired on the Siemens 7T Terra scanner at the Wolfson Brain Imaging Centre, University of Cambridge with the Nova Medical 1TX/32RX head coil. A projector at the head of the scanner projected the visual stimuli onto a translucent panel placed above the head coil.

2.2.3 Prospective Motion Correction (PMC)

I utilized a commercial optical system (Kineticor (first generation), https://kineticor.com/) to carry out PMC. This PMC system utilizes an optical camera in the bore of the scanner to track the motion of a passive Moiré phase marker at a frame rate of 80Hz (Maclaren et al., 2012). The Moiré phase marker is made up of multiple thin glass panels, with varying gratings printed on each panel. This allows the optical camera to obtain all three translational and three rotational degrees of freedom from a single marker. The precision of the translational and rotational measurements were previously reported to be 0.1mm and 0.1^{o} respectively(Maclaren et al., 2012). The measurements were calculated from the camera images on a separate computer, which then feeds the information into the scanner host computer. This is then transformed from camera to scanner coordinates using a calibrated transformation matrix acquired prior to the scan. These parameters are then used to update the imaging gradient, RF frequency and phase prior to the acquisition of each slice. This ensures that each voxel in the field of view corresponds to the same position in the brain throughout the scan.

In order to ensure that PMC functions properly, accurate marker-to-brain coupling is required. In Chapter 3, I will go over various methods of marker attachment, including check attachment and using mouthpieces to attach to the participant's teeth.

2.3 Post Processing Methods

2.3.1 Standard post processing pipeline in SPM

All data, unless otherwise specified, underwent standardized post-processing in SPM in Matlab (2009a, The MathWorks, Natwick, MA, USA). Chapters 3 and 4 utilized SPM 8, while subsequent chapters utilized SPM 12. However, the functions utilized were unchanged across versions, so there should be no inherent difference based on which version of SPM was utilized.

Firstly, the data underwent slice-time correction using temporal sinc interpolation. Next, rigid-body realignment, with a sum-of-squares cost function, was utilized to correct for between volume motion. No smoothing was carried out on the data as most of my analysis was focused on multi-variate pattern analysis.

2.3.2 TOPUP in FSL

For the 7T data, there was an additional TOPUP step after slice-time correction and prior to realignment. Prior to every EPI acquisition run on 7T, I acquired five EPI images with reverse phase encoding (revPE). These five revPE images were combined with the first five images of the fMRI time series to estimate the distortion using TOPUP (Andersson et al., 2003) in FSL version 5.0.6 (Niazy et al., 2004). This estimate is then used to correct the entire fMRI time series.

2.3.3 ROI segmentation (Visual Attention Experiment)

For Chapters 5 to 7, I utilized multiple visual ROIs for my analysis, including both early retinotopic (V1, V2 and V3) and mid-level categorically defined ROIs (scene-selective transverse occipital sulcus (TOS), parahippocampal place area (PPA), face-selective occipital face area (OFA) and fusiform face area (FFA)).

The segmentation of the retinotopic ROIs was done in Freesurfer 6.0.0. Retinotopic activation maps were generated from the retinotopic pRF localizer (Section 2.1.2) using the code described in Kay et al., 2013 and provided at http://kendrickkay.net/analyzePRF/. The maps were then projected onto a polygon-mesh reconstruction of the individual participants' cortices. V1 to V3 were manually segmented on the middle-grey layer of the surface reconstruction using the retinotopic activation maps as a reference. Each individual visual area was also manually segmented into quarter-field maps (e.g. V1 into V1v and V1d) for the purposes of functional contrast analysis.

For the categorical ROIs, activation t-maps where obtained using SPM 12 by fitting a GLM to the fMRI data from the categorical localizer runs. The face-selective areas (FFA and OFA) were obtained from a t-map of the resultant data from subtracting the object activations from the face activations. Similarly,

the scene-selective areas (TOS and PPA) were obtained from a t-map of the resultant data from subtracting the object activations from the scene activations. For each ROI, I took the 100 most differentially activated contiguous voxels in regions that correspond to their expected locations in the brain to define them.

As all localizer data was obtained at 3T, the ROIs were simply coregistered to the 3T functional data using the structural data as a reference. For coregistration to the 7T data, the 3T functional data was first coregistered the 3T structural data using the SPM coreg function. The 3T structural data was then coregistered to the 7T structural data, again using the SPM coreg function. The transformations from both coregistration steps were then applied to the ROI data. No further transformation was necessary since the BBR realignment process realigns the functional 7T data to the structural data.

2.4 Data Analysis Methods

I employed a variety of methods to assess the quality of the data. I summarized the main methods employed throughout the thesis below and will refer back to them in subsequent chapters.

2.4.1 tSNR analysis

$$tSNR = \frac{1}{n_{voxels}} \sum_{all\ voxels} \frac{Mean\ intensity\ of\ voxel}{Standard\ Deviation\ of\ voxel}$$

Equation 4: Calculation of tSNR. n_{voxels} refers to the total number of voxels that are summed across.

To obtain the tSNR for each voxel, I divided the mean voxel intensity across the entire time course by the standard deviation of the voxel intensity. This is then averaged across the whole brain, whole grey matter or region of interest to generate a mean tSNR for that region. The tSNR is a measure of the stability and strength of the signal across time and a high tSNR indicates better data quality and less noise.

2.4.2 General Linear Model (GLM)

For calculating functional contrast, fCNR (Section 2.4.4) and R2 (Section 2.4.5), I generated a GLM that modelled responses to the individual conditions (two orientations for Chapters 3 and 4, four attention conditions for Chapters 5 to 7). Each block of the GLM was modelled using a standard boxcar model and then convolved with the canonical SPM HRF. I did not include motion covariates in the GLM. Linear and first-order detrending was included in the model to remove signal drift. Non-stimulus periods were not modelled so zero corresponds to the implicit baseline. The post-processed data was fitted

to the GLM using ordinary least squares (OLS) regression, yielding individual beta estimates for each of the conditions.

2.4.3 Functional Contrast

$$Functional\ Contrast = \frac{1}{n_{voxels}} \sum_{voxels\ in\ ROI} (\beta_1 - \beta_2)$$

Equation 5: Calculation of functional contrast. β_x refers to the beta estimates for each individual condition and n_{voxels} refers to the total number of voxels that are summed across.

The functional contrast was obtained by contrasting the beta estimates of interest against other beta estimates or the implicit baseline. Due to the specificity of the definition of functional contrast, this definition is further elaborated on in the relevant sections. The functional contrast is a measure of the difference in response of the region to certain conditions relative to other conditions.

2.4.4 fCNR analysis

$$fCNR = \frac{1}{n_{voxels}} \sum_{vox\ in\ ROI} \frac{(\beta_1 - \beta_2)}{\sigma_{res}}$$

Equation 6: Calculation of fCNR. β_x refers to the beta estimates for each individual condition, σ_{res} refers to the standard deviation of the residuals of the GLM fit and n_{voxels} refers to the total number of voxels that are summed across.

For each voxel, the fCNR is obtained by dividing the functional contrast for that voxel by the standard deviation of the residual of the GLM fit. This is then averaged across the entire ROI to generate a single fCNR value for the whole region. Similar to tSNR, fCNR is also a measure of data quality, where a higher fCNR indicates that it is easier to discern between real functional activations and fluctuations due to noise.

2.4.5 R2 analysis

$$R2 = \frac{1}{n_{voxels}} \sum_{vox\ in\ ROI} \frac{\sigma_{fit}}{\sigma_{raw}}$$

Equation 7: Calculation of R2. σ_{fit} refers to the standard deviation of the model fit while σ_{raw} refers to the standard deviation of the raw data and n_{voxels} refers to the total number of voxels that are summed across.

For each voxel, the R2 was obtained by dividing the variance of the model fit by the total variance of the post-processed data. The model fit was obtained by multiplying the beta estimates for the individual conditions with the design matrix. This is then averaged across all voxels in the ROI to calculate a representative R2 value. The R2 value is a measure of the ability of the model to explain the variance in the data. A high R2 value indicates that the model is better able to explain the variance in the data and there is less noise, which gives rise to unexplained variance.

2.4.6 MVPA analysis

In addition to conventional univariate analysis, I also utilized two MVPA methods, SVM classification and LDC. MVPA analyses and compares the pattern of activations across the voxels in the ROI for different conditions, allowing it to pick up on more subtle differences relative to conventional univariate analysis. Both SVM classification and LDC are supervised machine learning algorithms. They are trained on a labelled subset of the data (training set) and tested on the remaining unlabelled data (testing set).

2.4.7 SVM classification

SVM classification has been widely used in fMRI analysis (Abdulkadir et al., 2013; Costafreda et al., 2011; De Martino et al., 2008; Hoeft et al., 2011; LaConte et al., 2005; Meier et al., 2012; Tripoliti et al., 2010; Weygandt et al., 2012) due to the simplicity of the implementation and ease of understanding. The SVM algorithm first identifies the points in the training data that are closest to the boundaries between the two classes (support vectors). These support vectors are used to calculate a decision hyperplane such that the total distance between the hyperplane and the support vectors is maximized. This hyperplane is utilized as the decision boundary where the testing data is mapped onto and assigned categories based on its position relative to the decision boundary. Despite the widespread use of SVM, I will show that with regards to fMRI data, it is a less sensitive MVPA metric compared to LDC in Chapter 4. Thus, SVM is only employed for the visual gratings experiment in Chapter 4 to compare the two MVPA techniques. In subsequent chapters, LDC is employed as the MVPA metric of choice.

I utilized the SVM classifier in the Matlab Bioinformatics toolbox for all of my SVM classification . I split each experimental run into four equal sub runs. Three of the four sub runs were combined to form the training set and the last sub run was utilized as the testing set for cross-validation. Within each set, each stimuli block was modelled as an individual epoch to generate a total of 24 data points for training and eight data points for testing. This setup was utilized to provide a larger number of samples for the training and testing data set, which would allow for a more stable estimate of classification accuracy. The 24 data points were utilized to generate the decision hyperplane using SVM, which was tested on the remaining eight data points. This was reiterated four times, leaving a different sub run out each time for cross-validation (leave-one-sub-run-out cross-validation). Above-chance classification accuracy (>50%) indicates that there is a persistent representation of the stimuli across time while fluctuations in classification accuracy would indicate changes in data quality.

2.4.8 LDC analysis

LDC is a continuous statistic that is derived from the well-known Fisher's linear discriminant and has also been adopted for fMRI analysis (Kriegeskorte and Diedrichsen, 2016; Misaki et al., 2010; Yoon et al., 2012; Zhu et al., 2008). Firstly, the training data is used to generate a set of weights to maximize the distance between the two conditions of interest (stimuli orientation, location or category). This set of weights is known as the discriminant. The LDC is a measure of the difference between the two conditions in the testing data, measured on this discriminant. This cross-validation step removes the positive bias affecting the estimates of distances (which are by definition positive) from noisy data (Walther et al., 2016). This measure is also referred to as the cross-validated Mahalanobis (crossnobis) distance (Kriegeskorte and Diedrichsen, 2016).

$$LDC = \left(\beta_{train,1} - \beta_{train,2}\right) \Sigma \left(\beta_{test,1} - \beta_{test,2}\right)$$

Equation 8: Calculation of LDC. Σ represents the error covariance matrix generated using the training data set and the product of the training contrast ($\beta_{train,1}$-$\beta_{train,2}$) with the error covariance matrix generates the weights vector. ($\beta_{test,1}$-$\beta_{test,2}$) is the test contrast vector.

Within each experiment, I partitioned the data into four equal subsets (by sub runs for the visual gratings experiment and by runs for the visual attention task). Three of the four subsets were combined to form the training set. Given that LDC does not require multiple data points to train on, all repeated blocks of the same stimulus type for the training set were modelled as a single event in the design matrix. Similarly, all repeated blocks of the same stimulus type for the testing set was modelled as a single event. This is one of the reasons why LDC is a better metric, as modelling all the presentations as a single event provides a more stable estimate of the activation pattern(Abdulrahman and Henson, 2016; Huang et al., 2018).

All data and design matrix underwent first order sinusoidal and linear detrending. The detrended training data was fitted to the detrended design matrix and used to calculate a pairwise contrast between the two conditions of interest. This generates a representational distance metric, which was then normalized using the sparse covariance matrix (Ledoit and Wolf, 2003) of the noise residuals to produce a weights vector. The LDC test statistic was calculated by taking the dot product of the weights vector with the pairwise contrast estimate from the test subset. Similar to SVM, this was reiterated four times, using a different subset for the testing data each time. I then averaged across all repetitions and normalized the metric across ROIs by dividing by the square root of the number of voxels in each ROI to obtain a final continuous performance estimate. This estimate is centred on zero under the null hypothesis of no consistent difference in response patterns between the stimuli across

subsets. A positive value indicates that there is a consistent difference in response patterns while a negative value indicates that the response patterns are anti-correlated between subsets.

2.5 Significance Testing

In order to verify whether my results were significant, I employed a variety of methods depending on the nature of the data. Throughout this thesis, I took $p<0.05$ to be significant.

2.5.1 Repeated Measures ANOVA

The results from the LDC analysis can be assumed to be continuous and approximately normally-distributed. Thus, they can be analysed using a repeated measures analysis of variance (ANOVA). Post-hoc comparisons were done using the Tukey's honest significant difference (HSD) test, which corrects for multiple comparisons. The repeated measures ANOVA models participants as a random effect (RFX), and can support inferences about the sampled population.

2.5.2 Permutation Testing

For other data that does not satisfy the assumptions of continuity or normality required for standard parametric testing, I carried out pairwise permutation testing. For results with more than two conditions (e.g. the three PMC conditions for Chapter 3), pairwise permutation testing was iterated over each pair of conditions. For each iteration, the labels for the measures used were randomized within each participant and the mean difference between the two methods was recorded. This was iterated 10000 times to generate a distribution and the actual mean difference obtained from the study was tested against the distribution. This models participants as a fixed effect (FFX) and produces similar p values as a fixed-effect T test when the Gaussian assumptions hold.

2.5.3 Wilcoxon Signed Rank Test

For the 7T data, I utilized the Wilcoxon signed rank test as the data does not satisfy the Gaussian assumptions. This was used over permutation testing due to the low number of participants, which renders permutation testing trivial. At this low sample size, the permutation testing results approaches that of the Wilcoxon signed rank test when the number of iterations approaches infinity. The Wilcoxon signed-rank test is a paired test that only requires that the data is on an interval scale and each pair of observations are random samples from a symmetric distribution. Due to the small sample size for the 7T data (six participants), my results will only be significant ($p=0.0313$) if all six participants demonstrate changes in the same direction. In all other cases, the results would not be significant ($p>0.0625$).

3 Prospective Motion Correction (PMC) at 3T

3.1 Abstract

In this chapter, I evaluated the effectiveness of PMC in improving the quality of 3T data. The PMC system utilizes an in-bore optical camera to track an external marker attached to the participant. I first compared three different forms of marker attachment and show that skin attachment is insufficiently rigid compared to the two methods of mouthpiece attachment. I used my custom-moulded mouthpiece to evaluate the effectiveness of PMC on a simple visual task with no deliberate subject motion. I showed that my custom-moulded mouthpiece is a cheaper and commercially available alternative to dentist-moulded mouthpieces and PMC helps improve the sensitivity of MVPA analyses at higher resolutions.

3.2 Introduction

As discussed in Section 1.4.1, subject motion is a pertinent issue in fMRI acquisitions. Due to the small signal of interest in most fMRI studies (Renvall et al., 2014; Runeson et al., 2013), any decrease in data quality could easily mask the signal. Moreover, stimuli-linked motion has also been shown to give rise to false positives in activation maps (Field et al., 2000).

The methods to correct for motion can be broadly classified into retrospective motion correction (RMC) and prospective motion correction (PMC). Historically, RMC has seen more widespread use. This is due to the simplicity and convenience of implementing RMC, with multiple MRI processing software (FSL, SPM, etc) having an in-built RMC function. Moreover, PMC requires the acquisition of time-linked motion data in real time which is a complex task in and of itself.

In RMC, rigid body translations and rotations (6DOF (degrees of freedom)) are utilized to realign each volume to a reference volume using the sum-of-squares cost function (Ashburner and Friston, 2003; Johnstone et al., 2006). While this is sufficient for slow motion between acquisition volumes, RMC is unable to remove artefacts that arise due to differences in spin history and k-space distortions (Goebel et al., 2006; Penny et al., 2011). These artefacts are a result of intra-volume motion. Moreover, as the acquisition box is not coupled to the brain, any motion can result in the loss of edge voxels for partial brain acquisitions.

PMC has been picking up popularity as a method to minimize the impact of motion as they have been demonstrated to perform significantly better than RMC techniques (Muraskin et al., 2013; Stucht et al., 2015; Todd et al., 2015). For PMC, the motion parameters of the participant's head are acquired

concurrently with the acquisition of the imaging volume (Callaghan et al., 2015; Maclaren et al., 2012). These motion parameters can be estimated either using internal MR data or external tracking modules. Internal MR methods, such as k-space navigators (Van Der Kouwe et al., 2006; Ward et al., 2000) or fat-based navigators (Engstrom et al., 2015) require additional acquisition in between volumes, which would further reduce the temporal resolution of the data. External tracking modules, including the Kineticor optical system evaluated in this chapter, utilizes a secondary system to acquire the motion parameters in real time and transfer the data to the scanner. As such, these modules have minimal impact on acquisition time. The motion parameters are then used to update the position of the acquisition box prior to each RF pulse such that the exact same brain volume is acquired throughout the session. Maclaren et al., 2013 and Zaitsev et al., 2016 provide a good overview on the current state of the field and highlights promising techniques. I expect PMC to improve the quality of the data relative to RMC for 2D EPI sequences (employed in this chapter) due to the following reasons. Firstly, PMC does slice-wise realignment, allowing for correction of both intra- and intervolume motion, while conventional RMC implementations only correct for intervolume motion. Additionally, accurate coupling of the acquisition box to the brain would preserve edge voxels and reduce spin-history effects(Yancey et al., 2011). This ensures accurate registration of voxels across the scan and preserves the edge voxels to allow for more data points in the model fitting.

One of the major hurdles for PMC implementation is the method of attachment of the marker to the participant. While attaching the marker to the participant's skin is easy and convenient, the coupling between the skin and the participant's brain is less than ideal and will often introduce additional errors and artefacts (Callaghan et al., 2015; Muraskin et al., 2013; Todd et al., 2015). At the other end of the spectrum, some sites utilize a dentist-moulded mouthpiece to ensure perfectly rigid coupling (Stucht et al., 2015). However, the process of creating the mouthpiece is both time-consuming and expensive as participants are required to visit a dentist more than a day prior to their scan to obtain a mould of their teeth. In this chapter, I attempt a novel method of moulding the mouthpiece on the spot using a commercially available dental putty. This is a middle ground between the two methods, allowing for more rigid coupling via attaching to the participant's teeth while also reducing time and monetary cost. I expect the custom-moulded mouthpiece to be superior to skin attachment, while showing comparable or slightly worse results compared to the dentist-moulded mouthpiece.

Another confound in the evaluation of the effectiveness of PMC on fMRI data is that most previous studies utilized deliberate participant motion (Ooi et al., 2011; Schulz et al., 2014; Todd et al., 2015). This type of motion would likely result in larger and more frequent head motion than what would be observed in a typical participant instructed to remain as still as possible. Thus, this would not be

representative of actual participant behaviour in the scanner and is likely to result in an overestimation of the benefit of PMC. Todd et al. 2015 utilized the same optical tracking system to correct 3D EPI resting state data under three different conditions- no motion, slow deliberate motion and fast deliberate motion. They observed a significant increase in tSNR for the two motion conditions but observed no differences between PMC and no PMC in the no motion condition. They also carried out PMC on a visual fMRI task and a motor fMRI task on a single subject and showed an increase in the number of significant voxels. Another group (Zaitsev et al., 2016) utilized the same system but were unable to observe any benefit in fMRI data for a simple finger-tapping task. However, the authors noted that this is potentially due to the poor adhesion of the marker as it was attached to the participant's nose rather than via a mouthpiece. Lastly, Schulz et al. 2014 showed that false positives were reduced in a leg movement task where participants were instructed to keep their heads as still as possible. Despite participants attempting to keep their head stationary, some amount of task correlated motion is to be expected, and hence, this is also unlikely to be representative to typical fMRI studies.

In this chapter, I compare the three different methods of marker attachment. Next, I evaluate the effectiveness of PMC on a typical visual fMRI experiment where participants were instructed to remain as still as possible throughout the scan. I also examine the impact of PMC using both univariate (tSNR, fCNR) and multivariate (LDC) methods. I chose to use visual gratings as my stimuli as their encoding in visual cortical response patterns is reasonably well-understood and has been shown to have high decoding accuracy (Alink et al., 2013; Kamitani and Tong, 2005; Tong et al., 2010). In addition, the gratings stimuli enable analysis of the effect of PMC on multiple spatial scales. In humans, the V1 representation of the visual stimuli occurs over different spatial scales. There is a general, coarse-grained selectivity pattern due to radial bias and additional selectivity on a finer spatial scale that is independent of radial bias. These fMRI effects arise due to the topography of the underlying neuronal population codes. Neurons that respond to radial bias appear more frequently, thus creating a global map of radial orientation frequencies. In contrast, neurons responding independently of radial bias are organized in a more fine-grained columnar map of orientation preference. This variance in spatial frequencies of these two nested organizations leads me to expect that the effectiveness of PMC can vary with the spatial scale of the fMRI measurement and with the visual field coverage of the ROI. Specifically, I expect PMC to be more beneficial in high resolution acquisition and in ROIs that do not exhibit radial bias.

3.3 Methods

3.3.1 Prospective Motion Correction (PMC)

I utilized the first generation Kineticor optical tracking system to carry out PMC. The specifics of the system were elaborated on in Section 2.2.3. In order to carry out accurate correction with PMC, rigid and accurate maker-to-brain coupling is required. I evaluated three different methods of attachment-skin attachment, custom-moulded mouthpiece and dentist-moulded mouthpiece.

Skin attachment was carried out by attaching the marker to the participant using a small piece of
880 double-sided tape. The marker was positioned on the participant's chin such that it is visible to the optical camera when the head coil is present. Nose, forehead and cheek attachment were attempted but deemed impractical as the coil would partially or completely obstruct the marker from the camera.

For my custom-moulded mouthpiece, a new mouthpiece was made for each participant prior to each session. Dental putty (Provil Novo: Putty Fast) was mixed and loaded onto a dental impression tray (Tra-Tens® Impression Trays, Waterpik). Participants were asked to bite on the tray for 2 minutes to allow the putty to harden. Once set, the tray remains firmly attached to the participant's teeth without requiring active biting. The marker was attached to the tray via a 3D printed plastic arm with three pivot points to allow flexible positioning of the marker within the field of view of the optical camera. After the scan, the tray can be removed by a hard jerk downwards with no lasting effect on the participant's teeth or gums. Images of the mouthpiece and how it is attached to a participant is shown in Figure 3-1.

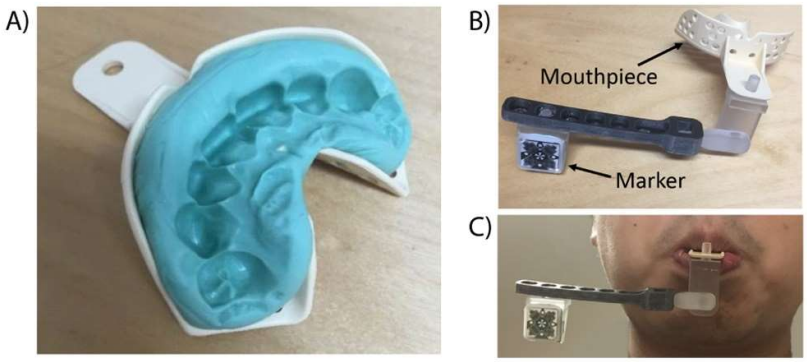

Figure 3-1: A) An example of moulded and hardened dental putty in the shape of the participant's teeth. Dental putty (Provil Novo: Putty Fast, turquoise component in the figure) was loaded onto the dental tray (white component). Participants were asked to bite down on the putty for two minutes. Once hardened, no deliberate effort was required from the participant to keep the mouthpiece in place. B) The marker is attached to the mouthpiece via an arm extension with 3 pivot points to allow for flexible positioning of the marker. C) A sample image of the entire setup when attached to a participant.

As a further point of comparison, I obtained dentist-moulded mouthpiece for two participants. This required the participants to visit a specialized dentist prior to the scan session to produce a mould of their teeth. These moulds are used to make the dentist-moulded mouthpiece for the participants.

3.3.2 Experimental Design

For comparisons between the different modes of marker attachment, I looked at the accuracy of the tracking data, residual motion after correction and resting state tSNR. I utilized a 3 x 2 x 2 factorial design: three different modes of attachment— skin attachment, custom mouthpiece and dentist-moulded mouthpiece; two motion cases— no motion and intentional motion and 2 correction manipulations— PMC On and PMC Off. I acquired 100 volumes of resting state fMRI for all permutations of cases. In the no motion case, participants were instructed to remain as still as possible to mimic a typical fMRI experiment. In the intentional motion case, participants were instructed to shift their head periodically. The range of motion was controlled such that the marker was in the field of view of the camera at all times. Due to technical limitations, the data for skin attachment were acquired during the initial session but testing with the mouthpieces took place in a separate, subsequent session.

I utilized a 2 x 3 factorial design for the main experiment: two different resolutions— 1.5mm isotropic voxels and 3.0mm isotropic voxels, and 3 different PMC cases— PMC On, Mouthpiece On (P+M+), PMC Off, Mouthpiece On (P-M+) and PMC Off, Mouthpiece Off (P-M-). In case P-M+, while PMC was not applied to the MRI data, I still collected the tracking data. The fourth case, PMC On, Mouthpiece Off was not tested because the mouthpiece was required to obtain accurate marker-brain coupling.

The three separate scan cases allowed for isolation of the following experimental effects: comparing data from cases P+M+ and P-M+ demonstrates the effect of PMC correction, while controlling for the presence of the mouthpiece, and comparing data from cases P-M+ and P-M- quantifies the effect of the mouthpiece. Most importantly, comparing the data from cases P+M+ and P-M- showcases the net benefit of implementing PMC in actual studies.

Data analysis was carried out over three distinct ROIs, the entire V1, regions with radial bias and regions without radial bias. Regions with radial bias are expected to have more coarse-grained response patterns and hence, should be more robust against motion effects. In contrast, regions without radial bias should have more fine-grained response patterns and be more sensitive to motion effects.

3.3.3 Data Acquisition

Two pilot participants were scanned at the Siemens 3T Prisma-Fit scanner to evaluate the effectiveness of skin attachment. The same two participants were scanned again for the purposes of comparing the two mouthpieces.

18 healthy participants were scanned at the Siemens 3T Prisma-Fit scanner for this experiment (8 females, age range 20-41 years). Participants provided informed consent under a procedure approved by the Cambridge Psychology Research Ethics Committee. Each participant was present for three repeat sessions under each of the three cases, P+M+, P-M+ and P-M-. The order of the cases was randomized across participants and all other scan sequences and procedures were preserved across sessions. Participants were blinded as to whether PMC was applied (P+M+ vs P-M+) to prevent bias, but were aware when no mouthpiece was present. In all sessions, participants were instructed to remain as still as possible so as to mimic the conditions of a typical fMRI experiment. The interval between session was not controlled due to restrictions imposed by participant and scanner availability. The range of intervals between consecutive sessions was 1-20 days.

MPRAGE structural images were acquired at the start of each session (TR=2250ms, TE=2.22ms, TI=900ms, GRAPPA=2, FOV=256mm*256mm*192mm, Matrix size=256*256*192, FA=9^{o}, ToA=~5mins). This was followed by a total of four functional task scans: two main experimental scans and two localizer scans. For the main experimental scans, the participants were scanned while viewing the gratings in a block design, once each at voxel resolutions of 3mm and 1.5mm. The data from these scans were used to compare the data quality across cases. The acquisition order for the two resolutions was randomised across participants but remained constant across the three repeat sessions for the same participant. The two localizer scans were carried out at 3mm resolution and used to generate a retinotopic map for the segmentation of ROIs. Each session was followed by an eight minute resting state scan for each participant. Upon completion of scanning for each session, the participants were asked to fill out a short questionnaire with regards to the comfort of the mouthpiece.

Field-of-view (FOV) parameters for both resolutions were chosen such that the same brain volume (192mm*192mm*90mm) was acquired across scans. Imaging parameters for the 3mm isotropic EPI were: TR=1260ms, TE=30ms, FA=78^{o}, Matrix size=64*64*20, ToA=~11mins. Imaging parameters of the 1.5mm isotropic EPI were: TR=3050ms, TE=30ms, GRAPPA=2, FA=78^{o}, Matrix size=128*128*40, ToA=~11mins. Imaging parameters for the 3mm resting state EPI were: TR=2000ms, TE=30ms, FA=78 o, Matrix size=64*64*32, ToA=~8mins.

The stimulus utilized in this experiment is described in full detail in Section 2.1.1. Three participants with lower than 50% response accuracy for the task were excluded from further analysis.

3.3.4 Data Analysis

The first three image volumes for each scan were discarded to allow the signal to reach steady-state. The time series then underwent pre-processing in a standard pipeline using SPM8 (Penny et al., 2011). Temporal sinc interpolation was used to correct for slice time differences and then rigid body realignment was applied to correct for head motion. Linear and first order sinusoidal detrending were applied to the data to remove signal drift. To evaluate the impact of PMC on fMRI data quality, I looked at several metrics, including residual motion using SPM motion parameters, tSNR, fCNR and LDC. The methodology behind tSNR, fCNR and LDC are described in Section 2.4 and significance testing was done using repeated measures ANOVA (Section 2.5.1) for LDC and pairwise permutation testing (Section 2.5.2) for all other measures.

Task accuracy for each participant was also calculated by dividing the number of correct responses by the total number of colour changes. Three participants with lower than 50% response accuracy for any run were completely excluded from further analysis.

3.3.5 ROI Segmentation

All ROI segmentations were done in Freesurfer 5.3.0. I obtained the activation t-maps in SPM by fitting a GLM to the fMRI data from the localizer runs. The maps were then projected onto polygon-mesh reconstructions of individual participants' cortices. V1 was the main region of interest for this study. The boundaries of V1 were obtained by contrasting the t-maps for the vertical wedges against horizontal wedges and contrasting the t-maps for the localizer rings against all four patch pairs respectively.

To further probe regions with and without radial bias, the regions were segmented based on their response to patch pairs 1 and 2 and patch pairs 3 and 4 (Figure 2-1, Panel B). Boundaries for each patch pair were obtained by contrasting the patch-pair of interest against all other patch pairs and the localizer rings (see Figure 3-2). As both orientations of the grating stimuli form an angle of 45 degrees with respect to the axis joining the centre of the circular patch to the centre of the stimuli for patch pairs 1 and 2, there should be minimal effect of radial bias in these regions. In contrast, the grating stimuli lie either perpendicular or parallel to the axis on which the patch pair lies for patch pairs 3 and 4, hence resulting in maximal radial bias. Due to the difference in spatial frequency of the activation patterns, regions driven by radial bias are expected to be more robust against motion effects as compared to regions with no radial bias. When the whole V1 is employed for classification training,

regions responding to radial bias would be expected to strongly drive classification performance and this could mask subtle differences in regions with no radial bias arising from small amounts of motion. Hence, data analysis was carried out on regions with and without radial bias individually, as well as the entire V1.

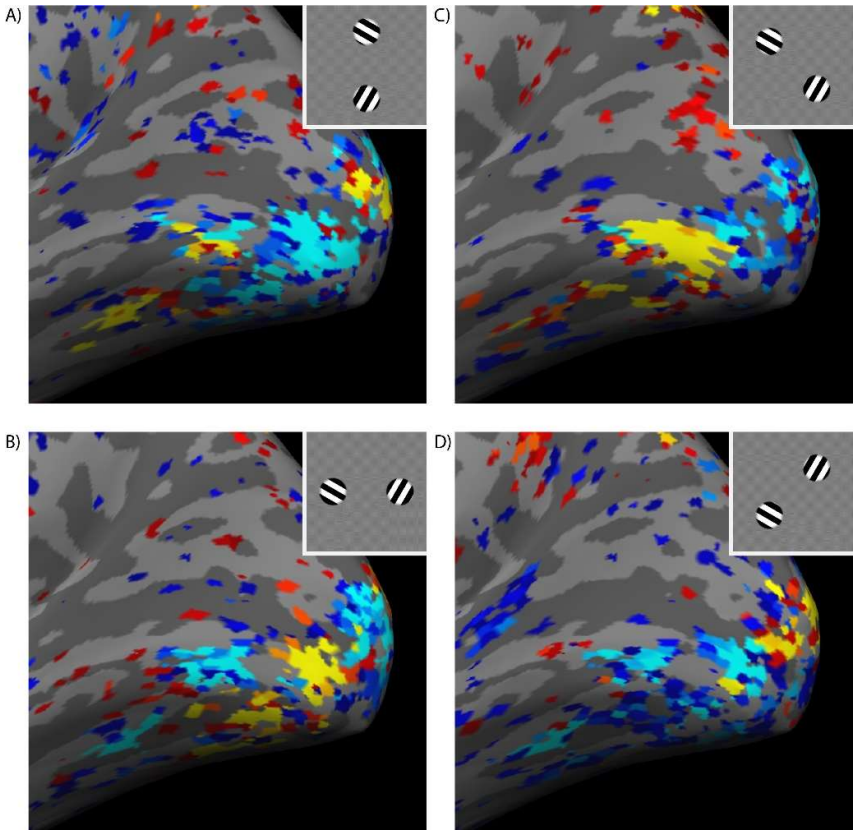

Figure 3-2: Example contrast maps of a participant's V1 shown on an inflated brain map in Freesurfer. Panels A-D show the activated regions (warm regions) corresponding to the inserted stimuli. These contrast maps are then used to segment out solid regions that correspond to each stimuli.

3.3.6 Analysis of SPM Motion Parameters

The realignment parameters for each run were extracted from SPM and analyzed. In case P+M+, this measure indicates the amount of residual motion that PMC failed to correct. For cases P-M+ and P-M-, this measure indicates the underlying amount of motion. Comparing case P-M+ and case P-M- allowed for quantification of the impact of the mouthpiece. To simplify the analysis, I combined data from all six degrees of freedom into one integrated motion metric per scan. Rotation angles were converted into displacement measures using a rotational radius of 5.7cm (which is reasonable considering the typical head size of an adult, Todd et al., 2015), and the square root of the sum of squares of the resulting six displacement parameters were calculated per unit time.

3.4 Results

3.4.1 Methods of Attachment

I first examined the data by evaluating the residual motion in SPM for both attachment methods when PMC was applied. The magnitude of the SPM realignment parameters would be indicative of the residual motion that PMC is unable to correct. In the no motion case, skin attachment performed the worst, with a residual integrated motion metric of 0.75±0.46 mm/s. My custom mouthpiece and the dental mouthpiece showed similar improvements, with a residual integrated motion metric of 0.22±0.08 mm/s and 0.24±0.01 mm/s respectively. In the motion case, skin attachment was again the worst performer (1.17±0.38mm/s). Both my custom mouthpiece (0.28±0.12mm/s) and the dentist moulded mouthpiece (0.27±0.13mm/s) showed substantial improvements relative to skin attachment. A sample illustration of the residual motion parameters is shown in Figure 3-3.

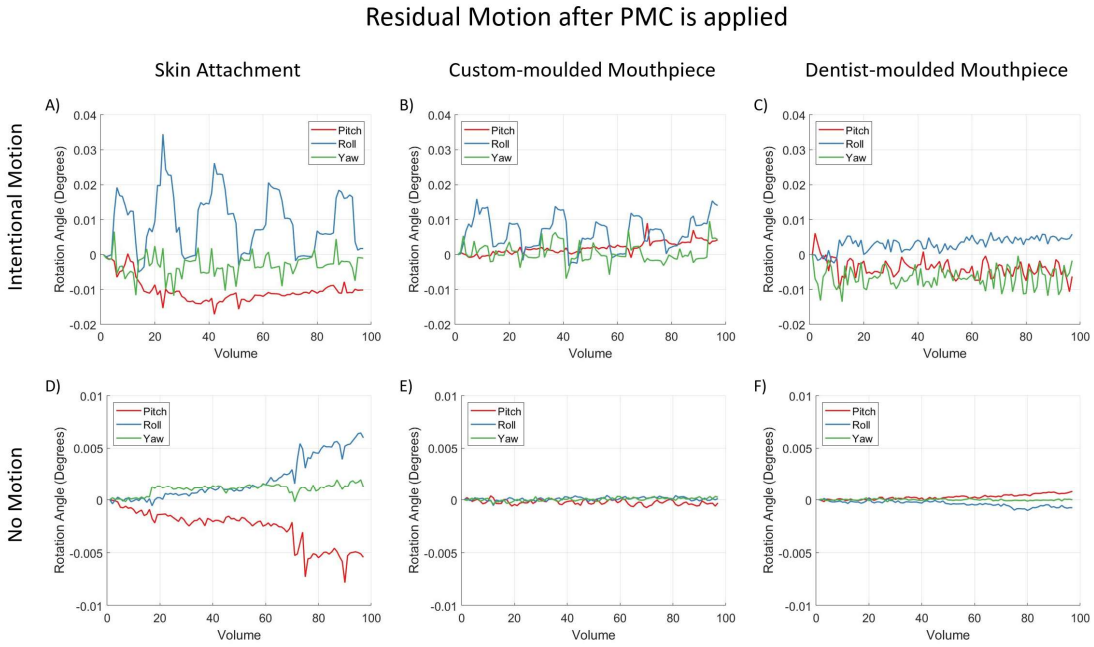

Figure 3-3: Illustration of SPM realignment parameters for one of the participants when PMC is applied. All panels show the rotation parameters. Panels A-C correspond to the scans where the participant was instructed to move their head periodically while Panels D-F correspond to the scans where the participant was instructed to remain as still as possible. The marker was attached to the participant's skin for Panels A and D, attached via the custom-moulded mouthpiece for Panels B and E and attached via a dentist-moulded mouthpiece for Panels C and F. Skin attachment performs worse than mouthpiece attachment for both cases.

Given that skin attachment is insufficiently rigid, it was excluded from subsequent analysis. Next, I compared the SPM realignment parameters with the motion parameters obtained from the camera,

shown in Figure 3-4. In both motion and no motion cases, there is a strong agreement between the SPM realignment parameters and the camera parameters for both mouthpieces. This suggests that for both mouthpieces, the marker is rigidly coupled to the brain and accurately reflecting the movement of the brain. There are some subtle differences between the two metrics, and this is likely due to the camera parameter reflecting the position of the brain at that point, while the realignment parameter reflects the realignment applied to the volume (i.e. a non-uniform average of the brain position for the period of acquisition for that volume.)

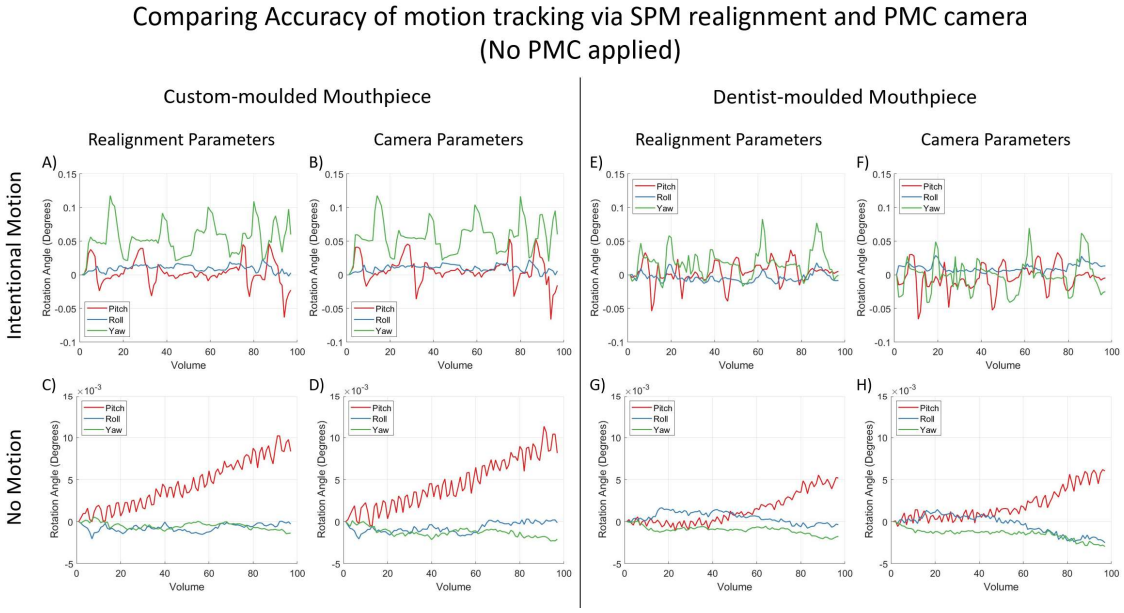

Figure 3-4: Using the data when PMC is not applied, I compared the SPM realignment parameters (Panels A,C,E and G) against the camera parameters (Panels B, D, F and H) to determine the accuracy of tracking. I compared the accuracy of the custom-moulded mouthpiece (Panels A-D) against the dentist-moulded mouthpiece (Panels E-H) for cases when the participant was instructed to move periodically (Panels A, B, E and F) and when the participant was instructed to remain as still as possible (Panels C, D, G and H). All panels show the rotation parameters. There is a strong agreement between realignment and camera parameters for both mouthpieces, indicating accurate tracking of brain motion.

Looking at the residual motion in the no motion case without PMC, I also note that the participants moved slightly more with my custom moulded mouthpiece (0.58±0.30 mm/s) as compared to the dentist-moulded mouthpiece (0.45±0.12mm/s). However, it is important to note that this does not translate to a difference in residual motion after PMC, where both mouthpieces showed comparable residual motion after PMC is applied.

Lastly, looking at the tSNR distribution (Figure 3-5), both mouthpieces showed similar results with no appreciable difference between them. The median tSNR for both mouthpieces were also similar, with the custom moulded mouthpiece having a median tSNR of 74 while the dentist moulded mouthpiece has a median tSNR of 73. The custom moulded mouthpiece is shown to be superior to skin attachment and comparable to dentist moulded mouthpiece, while been cheaper and more convenient. As such, the main study was carried out with the custom moulded mouthpiece.

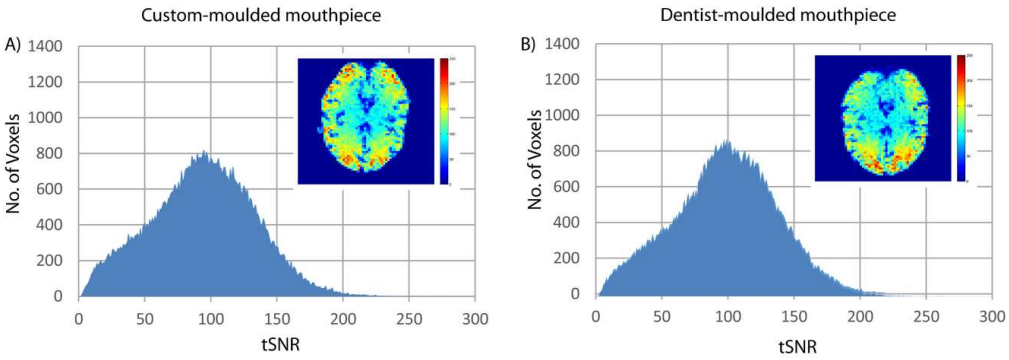

Figure 3-5: tSNR histograms for resting state fMRI comparing the custom-moulded mouthpiece against a dentist-moulded mouthpiece. The tSNR values were pooled from both participants into one histogram for each case. A representative slice through the tSNR map of one participant is shown as an inset for each case.

3.4.2 Participant Comfort

Based on the feedback that participants provided at the end of each session, most participants were relatively comfortable with the mouthpiece, rating it an average of 3.1 (min:0, max:7) on a scale of 0 to 10 with 10 being extremely uncomfortable. Half the participants reported that they had slight trouble swallowing with the mouthpiece. 94% of the participants indicated that they were willing to wear the mouthpiece for future scans, of which 88% expressed no reservations and 13% would only do so if it improved data quality. Participant ratings across sessions were consistent, indicating that repeated use of the mouthpiece did not substantially alter the experience for the participants.

3.4.3 Analysis of SPM motion parameters

For the main study, I calculated average integrated motion metric for each participant and plotted the results in Figure 3-6. All participants, with the exception of S07 and S11, demonstrate qualitatively similar motion profiles, with most residual motion for case P-M+ and least residual motion for case P+M+. There was a significant increase in motion between case P-M+ (mean: 2.84mm/s) and case P-M- (mean: 2.07mm/s) which shows that the mouthpiece causes a slight increase in participant motion ($p = 0.02$, FFX permutation test). However, the average motion metric showed a significant decrease in the P+M+ case when PMC is applied (mean: 0.90mm/s) and was significantly lower than both case

P-M+ (p = 0.0001, FFX permutation test) and case P-M- (p=0.0002, FFX permutation test). This indicates an overall beneficial impact of the PMC system on uncorrected head motion relative to a normal scan, despite the mouthpiece inducing participants to move slightly more.

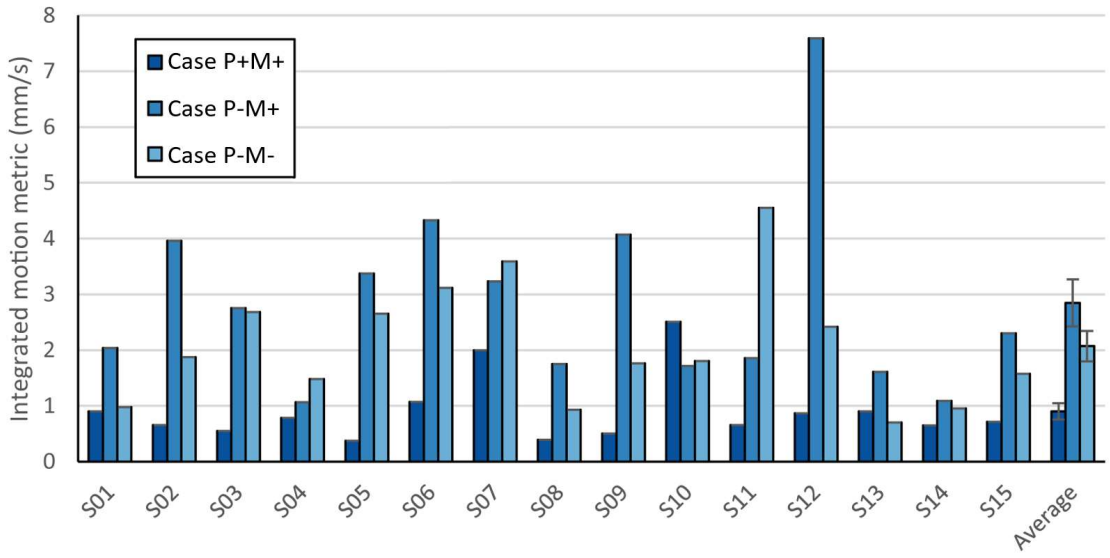

Figure 3-6: Plots of integrated motion metric of residual motion picked up by SPM post-processing for all participants. Most participants exhibit the common trend of least residual motion in Case P+M+, followed by Case P-M- and most residual motion in Case P-M+. Error bars in the average integrated motion metric indicate standard error over participants.

3.4.4 tSNR analysis of rsfMRI

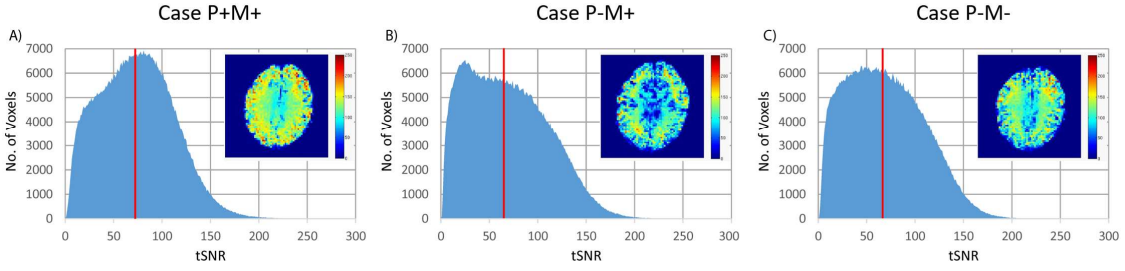

Figure 3-7: tSNR histograms for resting state fMRI comparing the three cases. The tSNR values were pooled from all 15 participants into a single histogram for each case. The vertical red line indicates the median tSNR across all participants. A representative slice through the tSNR map of one participant is shown as an inset for each case.

The tSNR results were obtained from the rsfMRI runs and are plotted in Figure 3-7. Data from all 15 participants were pooled for the histograms and the insets in the top right corner show a

representative slice through the tSNR map of a typical participant. Case P+M+ (median tSNR = 73) shows a clear shift in distribution towards voxels with higher tSNR values as compared to the other two cases. I also noticed a slight increase in voxels with low tSNR between 10 to 40 in case P-M+ relative to case P-M-, which may be a consequence of slightly increased head motion due to the mouthpiece. However, this difference is not reflected in the median tSNR values for cases P-M+ (median tSNR=65) and condtion P-M- (median tSNR=66). Pairwise permutation testing revealed that the tSNR from case P+M+ was significantly higher than that of case P-M+ (p=0.043, FFX permutation test) and case P-M- (p-0.022, FFX permutation test). There was no significant difference between condtions P-M- and P-M+ (p=0.309, FFX permutation test).

3.4.5 fCNR analysis

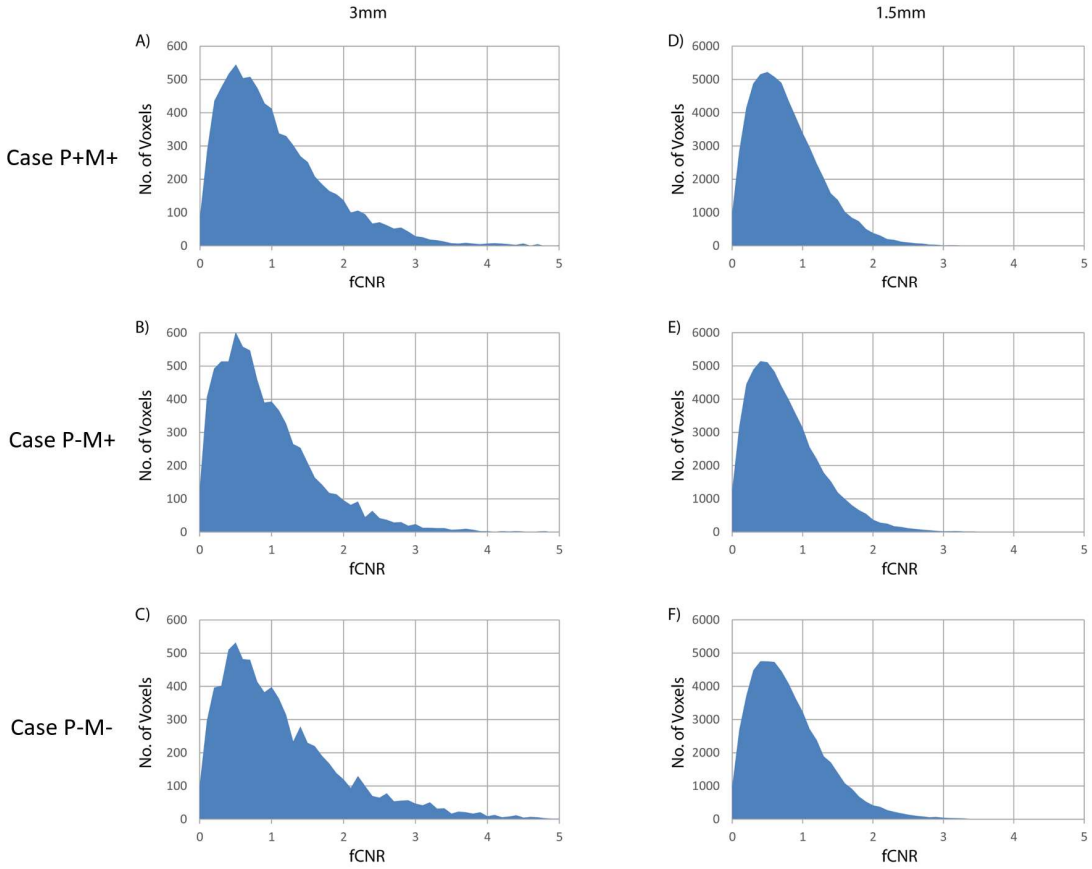

Figure 3-8: Histograms of fCNR comparing the three cases and two resolutions. The fCNR values were pooled from all 15 participants into one histogram for each graph. The graphs appear to have no observable differences and similar conclusions were drawn from permutation testing (see main text).

Analysis using the univariate fCNR method on V1 shows similar values for the individual cases at both 3mm (mean fCNR of cases P+M+, P-M+ and P-M-: 1.1, 1.0 and 1.1 respectively) and 1.5mm resolution

(mean fCNR of cases P+M+, P-M+ and P-M-: 0.82, 0.81 and 0.84 respectively). The fCNR plots are shown in 42Figure 3-8. Pairwise permutation testing showed no significant differences between the three cases at both resolutions (all p>0.15, FFX permutation test).

3.4.6 LDC analysis

The LDC results (Figure 3-9) show that there is indeed a benefit of using PMC, but this depended on the acquisition resolution. By carrying out a three-way repeated measures ANOVA (Table 3-1), I showed that there is no main effects of resolution or case (p>0.08). The only significant main effect is the main effect of region (F(2,14)=10.559, p=0.0004). Post-hoc Tukey's HSD tests after pooling data across PMC cases and resolutions (Supplementary Table 3-1A) showed that radial bias ROIs had a higher LDC compared to the entire V1 and ROIs without radial bias (p=0.0055 and p=0.0296 respectively, Tukey's HSD test).

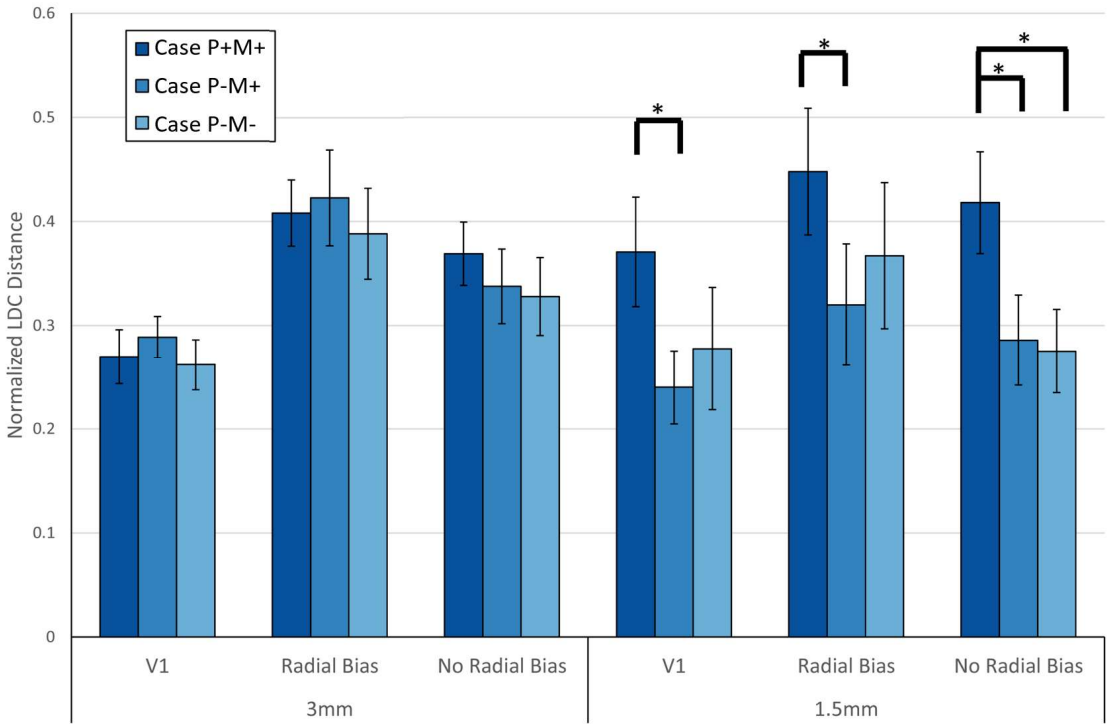

*Figure 3-9: Plot of normalized LDC distance per case, resolution and ROI. The distance measures were averaged across all 15 participants. Error bars indicate standard error over participants. * indicates p<0.05 (corrected for multiple comparisons, Tukey's HSD test).*

While the main effects of resolution and case was not significant, there was a significant two-way interaction (F(2,14)=5.6633, p=0.0086) between the two parameters, suggesting that the

effectiveness of motion correction is dependent on the resolution of the data. I interrogated this interaction further using post-hoc Tukey's HSD tests by pooling data across regions. A significant improvement in LDC was observed for case P+M+ relative to case P-M+ at 1.5mm (p=0.0086, Tukey's HSD test, Supplementary Table 3-1B). There were no significant differences observed at 3mm resolution (all p>0.5, Tukey's HSD test). All remaining two-way and three-way interactions were statistically insignificant (p>0.06).

Within each region and resolution, comparing the three cases showed that case P+M+ had a significant improvement in LDC relative to case P-M- for all regions at 1.5mm (p=0.022, p=0.045 and p=0.010 for the entire V1, regions with and without radial bias respectively, Tukey's HSD test, Supplementary Table 3-1C). Moreover, in regions with no radial bias at 1.5mm, Case P+M+ produced a significantly higher LDC relative to case P-M- (p=0.031, Tukey's HSD test). There were no significant differences (p>0.06) across cases for all other regions and resolutions. These analyses indicate that PMC improved the LDC metric, but this advantage was specific to high-resolution data. However, I was unable to show that this effect is also region-specific.

	Sum of Squares	DF	Mean Square Error	F	p
(Intercept)	30.772	1	30.772	95.4790	1.24E-07
Error	4.5122	14	0.3223		
(Intercept):Resolution	0.0043	1	0.0043	0.1275	0.7264
Error(Resolution)	0.4712	14	0.0337		
(Intercept):Case	0.2501	2	0.1251	2.7434	0.0817
Error(Case)	1.2764	28	0.0456		
(Intercept):Region	0.5208	2	0.2604	10.5590	0.0004*
Error(Region)	0.6906	28	0.0247		
(Intercept):Resolution:Case	0.1977	2	0.0989	5.6633	0.0086*
Error(Resolution:Case)	0.4888	28	0.0175		
(Intercept):Resolution:Region	0.0327	2	0.0163	2.9710	0.0676
Error(Resolution:Region)	0.1539	28	0.0055		
(Intercept):Case:Region	0.0177	4	0.0044	0.8313	0.5110
Error(Case:Region)	0.2978	56	0.0053		
(Intercept):Resolution:Case:Region	0.0150	4	0.0038	1.2524	0.2996
Error(Resolution:Case:Region)	0.1679	56	0.0030		

*Table 3-1: Repeated measures ANOVA results for LDC distance. * indicates p<0.05 (corrected for multiple comparisons, Tukey's HSD test)*

3.5 Discussion

Subject motion during an fMRI scan has been a constant issue for researchers. Across two different fMRI resolutions, I showed that utilizing PMC improves the quality of data at higher resolutions (1.5mm). Given the increasing interest in laminar structures and fine scale functional specialization that are only visible at sub-millimetre resolution(Kashyap et al., 2018; Kok et al., 2016; Xing et al., 2012), it is likely that PMC will become crucial for advancements in these endeavours.

Rigid marker attachment is critical to proper implementation of PMC. Here, I showed that skin attachment is insufficient and does not correct the data properly due to brain-independent motion, replicating the results of multiple previous studies (Callaghan et al., 2015; Muraskin et al., 2013; Todd et al., 2015). Comparisons between my custom-moulded mouthpiece and dentist-moulded mouthpiece showed that they yield similar benefits to data quality. While both participants felt slightly more comfortable with the dentist-moulded mouthpiece, this was not reflected in the post-processing motion parameters nor the tSNR estimates. This suggests that the cause of motion is due to the inherent presence of a foreign object in the mouth, independent of the type of attachment used, rather than due to participant's discomfort.

My results show that this commercially available alternative for marker attachment has comparable results with the more expensive dentist moulded mouthpieces employed in other sites. Moreover, this custom-moulded mouthpiece has the added benefits of accessibility and convenience as it is relatively inexpensive and can be moulded on the spot just minutes prior to the scan session. A dentist is also not required for my mouthpiece. Given that an overwhelming majority of participants were willing to use the mouthpiece in future scans, I believe that this would be extremely helpful in reducing the cost and complexity barriers to implementation of PMC for MRI scans.

I observed a benefit in resting state tSNR relative to the two control cases, replicating the results from Todd et al., 2015. However, I did not notice any significant differences in fCNR between cases. This behaviour is expected because the univariate ROI analysis only looks at the average activation over all the voxels within the ROI. Thus, in paradigms with robust activation patterns, the data will not be significantly affected by slight motion (which will only affect a subset of the voxels averaged). Moreover, participants were instructed to remain as still as possible, which would result in smaller differences across cases.

LDC analysis showed that regions with radial bias generates the largest LDC, consistent with results from previous studies by Freeman et al., 2013; Tong et al., 2010. These results suggest that decoding in the visual cortex is strongly driven by radial bias, rather than the fine-grained response patterns. There was also an interaction between resolution and case, indicating that there is a benefit of PMC specific to 1.5mm data. Moreover, there was also a numerical trend that improvements due to PMC were stronger in V1 sub-regions without radial bias, which were expected to have a more fine-grained spatial activation pattern. However, this difference was not significant when tested for using the three-way repeated measures ANOVA. In conclusion, I have shown that the advantage of PMC is more apparent at higher resolution but I was unable to demonstrate a dependence on the expected spatial frequency of the activation patterns.

There are three main limitations to my study. Firstly, I only employed 2D EPI sequences, and the benefits might vary depending on the sequence used. However, other studies have shown similar benefits of PMC with 3D EPI (Todd et al., 2015) and diffusion weighted imaging (Herbst et al., 2012), albeit using different forms of marker attachment. Secondly, the PMC implemented here assumes a perfectly homogenous B_0 and B_1 field. This is not true in a real MRI scanner, and head motion through inhomogeneous B_0 and B_1 fields can give rise to artefacts that PMC is unable to correct. For example, field distortions due to the sharp changes of magnetic susceptibility at tissue boundaries will give rise to signal dropouts and geometric distortions (Hutton et al., 2013). These issues require further correction, which can be implemented alongside or independently of PMC (Glover et al., 2000; Lutti et al., 2013). Lastly, I did not utilize alternative methods of PMC (Dietrich et al., 2016; Engstrom et al., 2015) and thus is unable to compare between the various methods.

3.6 Conclusion

As the field advances towards higher resolutions and more powerful fields, subject motion during fMRI will remain a pertinent issue. In this chapter, I have shown that PMC has great promise for being able to reduce the impact of subject motion by continuously tracking the participant head and updating the scanner. This agrees with previous work on PMC and further extends it by showing that the benefit is present even when participants are instructed to keep as still as possible, similar to a typical fMRI experiment. I also introduced a custom moulded mouthpiece option for marker attachment, which is shown to be superior to skin attachment and produces comparable results to a dentist moulded mouthpiece. This custom mouthpiece can greatly reduce the cost and inconvenience for marker attachment and can potentially lead to a more widespread adoption of the PMC system.

3.7 Supplementary Materials

Table A

ROI 1	ROI 2	Difference	Standard Error	p	Lower (95% confidence)	Upper (95% confidence)
Entire V1	Radial Bias	-0.1075	0.0285	0.0055*	-0.1822	-0.0329
Entire V1	No Radial Bias	-0.0509	0.0212	0.0742	-0.1063	0.0046
Radial Bias	No Radial Bias	0.0567	0.0196	0.0296*	0.0055	0.1079

Table B

Resolution	Case 1	Case 2	Difference	Standard Error	p	Lower (95% confidence)	Upper (95% confidence)
3	P+M+	P-M+	-0.0008	0.0272	0.9996	-0.0720	0.0705
3	P+M+	P-M-	0.0230	0.0310	0.7441	-0.0582	0.1042
3	P-M+	P-M-	0.0237	0.0223	0.5496	-0.0345	0.0820
1.5	P+M+	P-M+	0.1303	0.0369	0.0086*	0.0339	0.2268
1.5	P+M+	P-M-	0.1057	0.0530	0.1498	-0.0329	0.2443
1.5	P-M+	P-M-	-0.0246	0.0452	0.8507	-0.1429	0.0937

Table C

Reso-lution	ROI	Case 1	Case 2	Difference	Standard Error	p	Lower (95% confidence)	Upper (95% confidence)
3	Entire V1	P+M+	P-M+	-0.0190	0.0249	0.7296	-0.0841	0.0461
3	Entire V1	P+M+	P-M-	0.0079	0.0282	0.9583	-0.0660	0.0817
3	Entire V1	P-M+	P-M-	0.0269	0.0170	0.2837	-0.0175	0.0713
3	Radial Bias	P+M+	P-M+	-0.0146	0.0401	0.9297	-0.1196	0.0904
3	Radial Bias	P+M+	P-M-	0.0198	0.0444	0.8969	-0.0965	0.1361
3	Radial Bias	P-M+	P-M-	0.0344	0.0278	0.4503	-0.0383	0.1072
3	No Radial Bias	P+M+	P-M+	0.0314	0.0309	0.5800	-0.0496	0.1124
3	No Radial Bias	P+M+	P-M-	0.0412	0.0301	0.3818	-0.0375	0.1200
3	No Radial Bias	P-M+	P-M-	0.0098	0.0282	0.9355	-0.0641	0.0838
1.5	Entire V1	P+M+	P-M+	0.1308	0.0428	0.0219*	0.0187	0.2428
1.5	Entire V1	P+M+	P-M-	0.0933	0.0587	0.2827	-0.0604	0.2469
1.5	Entire V1	P-M+	P-M-	-0.0375	0.0547	0.7755	-0.1806	0.1056
1.5	Radial Bias	P+M+	P-M+	0.1279	0.0480	0.0456*	0.0024	0.2535

1.5	Radial Bias	P+M+	P-M-	0.0808	0.0634	0.4310	-0.0850	0.2467
1.5	Radial Bias	P-M+	P-M-	-0.0471	0.0568	0.6920	-0.1958	0.1016
1.5	No Radial Bias	P+M+	P-M+	0.1323	0.0383	0.0101*	0.0321	0.2326
1.5	No Radial Bias	P+M+	P-M-	0.1430	0.0497	0.0308*	0.0129	0.2731
1.5	No Radial Bias	P-M+	P-M-	0.0107	0.0375	0.9563	-0.0874	0.1088

*Supplementary Table 3-1: Multiple Comparison Results for the normalized LDC distance. Table A shows comparisons between ROIs, pooling results across resolutions and cases. Table B shows comparisons between cases for each resolution, pooling results across ROIs. Table C shows comparisons between cases for each resolution and ROI. * indicates p<0.05 (corrected for multiple comparisons, Tukey's HSD test)*

4 LDC vs SVM: Comparing MVPA Methods

4.1 Abstract

Multi voxel panel analysis (MVPA) has become increasingly popular as a method to analyse fMRI data due to higher sensitivity and the ability to investigate the multidimensional information present in the pattern of voxel activations. MVPA treats the fMRI experiment as a supervised learning problem, where a classifier is trained on the fMRI data to differentiate the experimental conditions. Here, I examined two different MVPA methods— linear discriminant contrast (LDC) and support vector machines (SVM), and compared their sensitivity using both real fMRI data and simulated fMRI data. My analysis shows that LDC is a better metric than SVM for fMRI data, despite the latter being more commonly used.

4.2 Introduction

To perform most methods of analysis on fMRI data, an activation map of the brain is required. This is generated by searching individual voxels for linear correlations between the voxel's fMRI time course and the activation model (GLM matrix). This activation map informs researchers of how each voxel is expected to behave when exposed to specific experimental conditions and is utilized for further analysis.

In conventional fMRI analysis, statistical analysis is then carried out on each voxel individually and iteratively to identify voxels or regions whose BOLD responses display statistically significant effects (Friston et al., 1994; Kindermann et al., 2002). This method is also referred to as mass univariate analysis. Due to the large number of voxels, the significant level needs to be controlled for multiple comparisons, using methods such as Bonferroni correction. Alternative methods to account for correct for family-wise errors include Gaussian random field theory (Brett et al., 2003), which utilizes the smoothness of the activation map to generate clusters of voxels with an assigned p-value, instead of individual voxels.

In contrast, MVPA probes the voxel activation maps for reproducible spatial activation patterns that differentiate the various experimental conditions (Detre et al., 2006; Kamitani and Tong, 2005; Kriegeskorte et al., 2008; Savoy and Cox, 2003). The MVPA can be considered as a supervised classification problem, where a classifier is trained to capture the relationship between the spatial patterns of fMRI activity and the experimental conditions. More specifically, MVPA attempts to determine a classification function, F, that utilizes the values of all the voxels activations as "features"

to predict the experimental condition as the "label" for the data. To obtain the function F, the classifier is trained on a subset of the data, referred to as the training set. The classifier models the relationship between the features and the labels by assigning a weight to each feature, where the magnitude of the weight corresponds to the predicted contribution of that feature to successfully differentiate the two conditions. This classifier is then tested on the independent subset of the data excluded from the training, referred to as the testing set. The performance is evaluated by comparing the predicted labels with the real labels.

MVPA confers a few advantages compared to univariate analysis. Firstly, univariate analysis treats each voxel independently and disregards any information stored in the pattern of activations. This means that univariate analysis can fail to detect activation when voxels in a region respond in different ways to the experimental conditions (Diedrichsen et al., 2013). In contrast, MVPA tests how the distribution of BOLD activations vary across voxels in relation to experimental variables, and thus is sensitive to a broader range of task-related effects. Univariate analysis is also limited by the need to correct for multiple comparisons. While necessary to prevent the detection of false positives, such corrections inherently reduce the sensitivity of univariate analysis and/or makes underlying assumptions about the spatial distribution of activations. Moreover, voxel-wise analysis has been shown to be susceptible to subject-level differences. Davis et al., 2014 showed that increasing variance between participant responses resulted in decreasing statistical significance for univariate analysis whereas MVPA statistical tests remained independent of subject-level differences. An added benefit of MVPA is the ability to cross-validate. Cross-validation is done by repeating the MVPA methods and utilizing a different subset as the testing set each time (leave-one-sub-run-out cross-validation). This process removes the positive bias on my estimates due to noisy data (Walther et al., 2016) and hence ensures that any differences in metrics are a result of real difference in activations, rather than variations in noise across sessions. While cross-validation can theoretically also be done on univariate analysis, it has not been done as far as I am aware. At the same time, it is important to be aware that MVPA and univariate analysis are sensitive to different aspects of activation patterns and have different noise susceptibility. Thus, while it is tempting to conclude that MVPA reveals a complex underlying multidimensional response when MVPA results are significant but univariate analysis is not, differences between the two methods, on their own, are not definitive in concluding the presence of a complex underlying process (Coutanche, 2013; Davis and Poldrack, 2013). This also highlights the importance of carrying out both univariate and multivariate analysis on fMRI data.

Here, I present two methods of MVPA— SVM and LDC and evaluate their effectiveness. SVM classifiers are a type of supervised machine learning algorithm that has seen widespread use in fMRI studies

(Abdulkadir et al., 2013; Costafreda et al., 2011; De Martino et al., 2008; Grotegerd et al., 2013; Hoeft et al., 2011; LaConte et al., 2005; Meier et al., 2012; Tripoliti et al., 2010; Weygandt et al., 2012). SVM utilizes the training data to generate a linear decision boundary described by a weights vector (Cortes and Vapnik, 1995; LaConte et al., 2005). The weights vector is determined by maximizing the separation between the decision boundary and the data points closest to the boundary, as illustrated by Figure 4-1. The testing data is then mapped onto the same space and assigned one of the two condition labels based on its position relative to the decision boundary. The assigned labels are compared to the real labels and used to calculate the accuracy of the classifier.

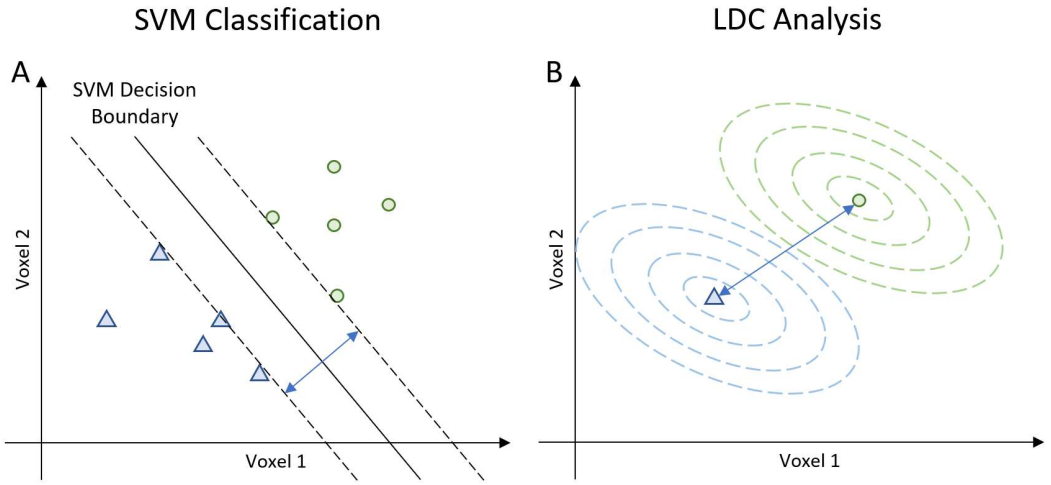

Figure 4-1: A simple two voxel illustration of how SVM (Panel A) and LDC (Panel B) trains the classifier. SVM generates a decision boundary such that it maximizes the separation of the two groups of data perpendicular to the decision boundary (illustrated by the dotted lines). LDC combines all repeats of one condition into a single data point, and the weights vector (blue arrow) is generated by the separation of the two points, normalized by the noise covariance matrix. The dotted ellipsoids are iso-probability density contours for the LDC: any point on a contour has the same probability of belonging to the experimental condition.

LDC also utilizes the training data to generate a weights vector, although the method of generation of these weights differs from SVM. The LDC weights are chosen by normalizing the distance metric between the two conditions from the training data by the sparse covariance matrix (Ledoit and Wolf, 2003) of the noise residuals. This biases the weights such that voxels with more stable differences between conditions are given a higher weight while the impact of voxels with high variance are minimized, generating weights that should produce maximum sensitivity to the difference between the two conditions. The distance between the two test conditions is then mapped onto this weights vector using the dot product to generate the contrast vector. The magnitude of the contrast vector gives the estimate of the stability of the differences between the two conditions. While LDC is a newer

technique, it has been gaining traction in the fMRI community(Kriegeskorte and Diedrichsen, 2016; Misaki et al., 2010; Yoon et al., 2012; Zhu et al., 2008).

Under the null hypothesis of no reliable pattern difference between the two conditions, I would expect a classification accuracy of 50% (chance level) and an LDC centred on zero. Above chance classification accuracy and positive LDC values are indicative of a positive correlation between the training data and testing data.

I expect that LDC will perform substantially better than SVM due to the following three factors: continuous estimate, no absolute threshold and robustness against trial-to-trial variability. Firstly, the LDC provides a continuous estimate of the reliability of the pattern. Thus, it does not suffer from the discretization problem faced by SVM, where small fluctuations that do not affect the classification are not detected. Moreover, there is no ceiling effect since the maximum representational distance is not capped. In contrast, SVM classification is capped at 100% accuracy and thus, would be insensitive if classification results are in that regime. This difference is illustrated using a simplified 2 voxel example in Figure 4-2, Panels A and B.

Secondly, LDC utilizes a dot-product between the weights vector and the contrast estimate from the test data. Thus, this generates an estimate of the coherence of the data without needing to establish a threshold parameter. On the other hand, SVM classification utilizes a rigid absolute threshold. As the data in fMRI are unitless and the magnitude of responses can vary significantly between runs due to factors such as scanner drift and participant motion, it is plausible that classification errors could result from an SVM classifier that learnt the correct weights for the voxels but applied an incorrect threshold due to inter-run variations of activation magnitudes. This is illustrated using a simplified 2 voxel diagram in Figure 4-2, Panels C and D.

Lastly, LDC only requires a single estimate for each condition. This allows for all repeat presentations of the same condition to be modelled as a single event in the design matrix. For SVM, a larger number of training data is needed to drive the classifier and a larger number of testing data is also needed to allow for a more stable estimate of classification accuracy. Thus, SVM requires each presentation of a condition to be modelled as an individual event in the design matrix to generate enough data points. However, this method of estimation of activations is less stable as compared to modelling all repeats as a single event as in LDC (Abdulrahman and Henson, 2016).

SVM and LDC were chosen as my two MVPA methods of interest because SVM classification has seen widespread use in fMRI data and appears to be the default MVPA method for many research groups. LDC analysis was chosen because I believe it to be the optimal MVPA method for fMRI data.

To compare the two MVPA methods, I utilized the fMRI data from Chapter 3 and also computer simulations with similar design and noise profiles as the fMRI data. This allows me to check the reproducibility of my results. I also repeat the LDC analysis, with individual regressors instead of a single regressor for each condition, to illustrate the impact of the stability of contrast estimates. This allows me to separate the inherent benefits of LDC (no decision boundary and continuous representation) from the stability of the contrast estimates, a tangential source of benefit for LDC.

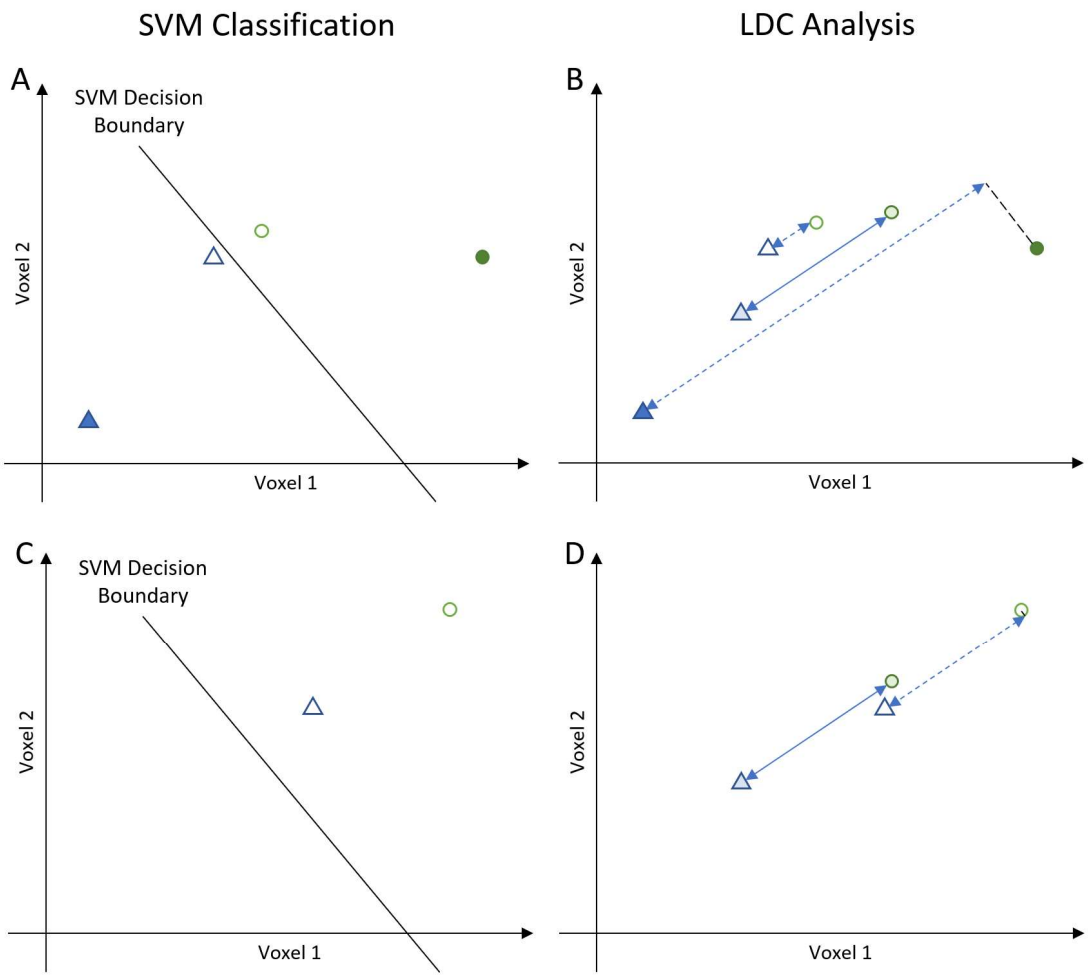

Figure 4-2: Illustration of the shortfalls of SVM (Panels A, C) and how they are addressed in LDC (Panels B, D) using a simple 2 voxel example. Firstly, due to the discretization of results by SVM, the metric is insensitive to two pairs of points that are slightly different (hollow shapes) and substantially different (solid shapes, Panel A). In contrast, the LDC generates a weights vector using the mean response to the two different conditions (shaded shapes) and generates the contrast by taking the dot product. This measures the distance indicated by the dotted lines (Panel B), showing that it would be sensitive to the difference in distance between the two pairs of points. Secondly, SVM has a rigid decision boundary. Thus, if the pair of testing data has the same differential activation pattern as the training data but is offset by a large amount (Panel C), the SVM classifier would inaccurately

classify one of the points, in this case, the blue triangle. In contrast, LDC simply measures the distance between the two points along the axis of the weights vector (dotted line), and hence is irrelevant under any offset.

4.3 Methods

4.3.1 MVPA methods

The implementations of SVM and LDC are described in Sections 2.4.7 and Sections 2.4.8. Briefly, the data was partitioned into the four sub-runs. Three of the sub-runs were utilized as the training data and the last sub-run was utilized as the testing data.

For SVM, each presentation of the stimuli was modelled as an individual epoch to generate a design matrix comprising 12 regressors per condition for training and four regressors per condition for testing. In contrast, the LDC modelled all repeats of each condition within the training data as a single event in the design matrix. Similarly, all repeats of each condition within the testing data was also modelled as a single event. Lastly, to address the differences that arise from the stability of activation patterns due to different modelling, I also repeated the LDC analysis with individual regressors. In this case, each presentation of the stimuli was modelled as an individual block, similar to SVM. All beta estimates for each condition were averaged to generate a single value for the training and testing data individually. This provides a singular estimate for each condition for the training and testing data, which then underwent identical analysis as the LDC with a single regressor per condition.

In all cases, both the post-processed data and the design matrix underwent linear and sinosodial detrending. The detrended data was then fitted to the design matrix using ordinary least squares regression to obtain beta values (fitted parameter estimated for each voxel for each condition or presentation).

For LDC (both single and multiple regressors), a pairwise contrast was calculated between the beta values of the two conditions and normalized using the sparse covariance matrix (Ledoit and Wolf, 2003) to generate a representational distance metric. This is also referred to as the weights vector and the dot product between the contrast estimate from the testing data and the weights vector generates the LDC test statistic. For SVM, the classifier is trained using the 24 data points in the training data and then tested on the remaining eight data points in the testing data.

For all three methods, the process was reiterated four times, leaving a different sub-run out each time, a cross validation method referred to as leave-one-sub-run-out cross-validation.

4.3.2 fMRI Data

The fMRI data used for this analysis is described in Chapter 3. Data was acquired at two resolutions— 1.5mm and 3mm isotropic, with three different cases of motion correction— PMC On, Mouthpiece On (P+M+), PMC Off, Mouthpiece On (P-M+) and PMC Off, Mouthpiece Off (P-M-). i expect case P+M+ to show improvements in data quality relative to the other two metrics and that the benefits should be larger at 1.5mm isotropic resolution. Data analysis was also carried out over three ROIs— entire V1, regions with radial bias and regions without radial bias. I evaluated this using a three-way repeated measures ANOVA, and repeated it thrice, once for each MVPA method.

4.3.3 Computer Simulation

In addition to the fMRI data, a set of computational simulations was also carried out and used to compare the different MVPA methods. This was done by generating an array of 100 simulated fMRI datasets and carrying out both LDC and SVM analysis on each dataset. I simulated the fMRI response to a similar stimuli setup as the fMRI experiment— two stimuli, presented in an altering sequence for four sub-runs. I generated a design matrix with two regressors (one regressor per stimuli). This design matrix was preserved across all simulated participants and iterations.

Within each of the 100 iterations, I generated 15 sets of data, simulating 15 different participants, identical to the size of the dataset of the fMRI experiment. Each set of data consisted of 500 voxels, which is equivalent to the average number of voxels. For each voxel, the activation response to each stimulus was obtained by sampling from independent Gaussian distributions of with mean 0 and standard deviation 1. This generates a vector centred around 0, with an expected mean absolute difference between conditions of $2/\sqrt{\pi}$. This expected mean is calculated by integrating abs(x_1-x_2)*P(x_1)*P(x_2) across all possible values of x_1 and x_2, where x_1 and x_2 are the activation responses to each stimuli. This was normalized to give a mean absolute contrast of 1 to generate the contrast vector. The design matrix was multiplied by the contrast vector to simulate the activation timecourse of this voxel. This was repeated 500 times to create a simulated, noiseless fMRI dataset for one participant. This was then repeated 15 times to simulate 15 different participants for one iteration.

I added three types of noise to each dataset. Firstly, at the level of the activations, noise (mean 0, standard deviation 1) was added to each presentation block to reflect variations in attention to the stimuli by the participant. Secondly, thermal noise was modelled using independent Gaussian noise for each voxel and each timepoint (mean 0, standard deviation 1.8). The first two sources of noise were assumed to be constant in variance across all repeats. Lastly, the physiological noise, arising due to factors such as heartbeat, respiration and head motion, was modelled by generating 10

independent Gaussian noise vectors for the entire time course (mean 0, standard deviation 1), and projecting a randomly weighted combination of these 10 vectors onto each voxel. The underlying physiological noise time courses were independent across sub-runs, but the projection of the vectors onto the voxels was held constant for a given participant, thus providing a reliable covariance structure that the discriminant methods could exploit. I varied the physiological noise level to simulate the effect of PMC on the data in the fMRI experiment.

The variance of the thermal noise in my model was estimated based on the ratio the thermal noise to total noise in the fMRI data. This was done by first measuring the fluctuations in signal intensity outside the brain to generate an estimate of the thermal noise in the fMRI data. I then calculated the ratio of thermal noise to total noise in the real data and obtained a standard deviation of 1.8 for thermal noise using a fCNR value of 1.8 (similar to that of the 3 mm data).

This model makes a few implicit assumptions. Firstly, I assume that the underlying response to a stimulus is identical across repetitions both within and across runs and any difference in response is due to noise. Secondly, I assumed that activation and thermal noise remained constant across repeats and are independent of changes in physiological noise. Lastly, the simulation approach assumes that the effect of PMC is to reduce physiological noise in the data, without affecting other noise sources.

The noise model was designed by myself, with inputs from my supervisors, to attempt to accurately capture all aspects of the noise in the data. The initial variance in activation response reflects variations in the participant's attention levels. The thermal noise reflects the gaussian noise present in fMRI data and is also derived from the real fMRI data. Lastly, the physiological noise reflects global physiological effects (motion, drifting, respiratory and cardiac) that affect all voxels, albeit in different ways.

Each simulated participant's data were then passed through both LDC and SVM analysis. Simulated group-level differences in discriminant performance were then assessed with pairwise t-tests conducted across varying fCNR. Finally, I calculated rejection probability for each fCNR pairing as the proportion over the 100 simulated iterations where difference between the outputs are statistically significant($p<.05$). The thermal and physiological noise sources were scaled to achieve two objectives: First, a mean fCNR over voxels that matched the real data (namely an fCNR of 1.6 for 1.5 mm data and 1.8 for 3 mm data); Second, a sufficiently wide range of fCNR differences (i.e., strength of physiological noise manipulation) such that it is possible to observe the full range of rejection probabilities. Note that these values of fCNR values listed here are distinct from the fCNR calculated in Chapter 3 because of a difference in contrast definitions. The fCNR contrasts in Chapter 3 measure the presence vs

absence of stimuli, while here, I contrast as the difference in activation between the two stimulus orientations.

4.4 Results

4.4.1 fMRI Data

I analysed the fMRI data using the three different methods and compared their ability to detect improvements due to PMC. Analysis with LDC results were presented in Section 3.4.6, and replotted here (Figure 4-3) for convenience of comparison. I note that there is no clear or consistent trend for 3mm isotropic data, while for 1.5mm data, the LDC detects a significant improvement for P+M+. This is supported by a significant two way interaction between resolution and type of PMC (Table 3-1).

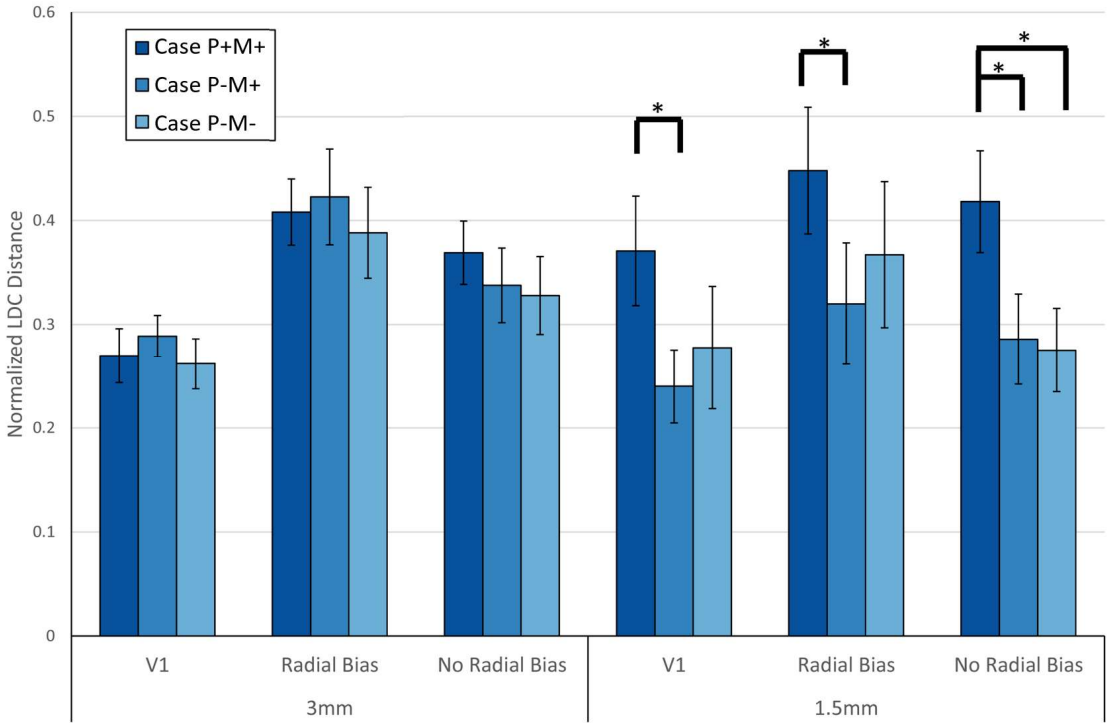

*Figure 4-3: Plot of normalized LDC distance per case, resolution and ROI. The distance measures were averaged across all 15 participants. Error bars indicate standard error over participants. * indicates p<0.05 (corrected for multiple comparisons, Tukey's HSD test).*

Repeating the LDC analysis with individual regressors (Figure 4-4) instead of multiple regressors yielded a graph with similar overall profile, with no clear trend for 3mm isotropic data and a constant

trend of P+M+ outperforming the other two PMC types at 1.5mm. However, the differences between the types of PMC is no longer significant (Supplementary Table 4-1). This supports the theory that individual regressors result in a less stable estimate of the contrasts, and hence is less sensitive to differences in data quality. In addition, all LDC values are smaller across the board for LDC with individual regressors as compared to standard LDC.

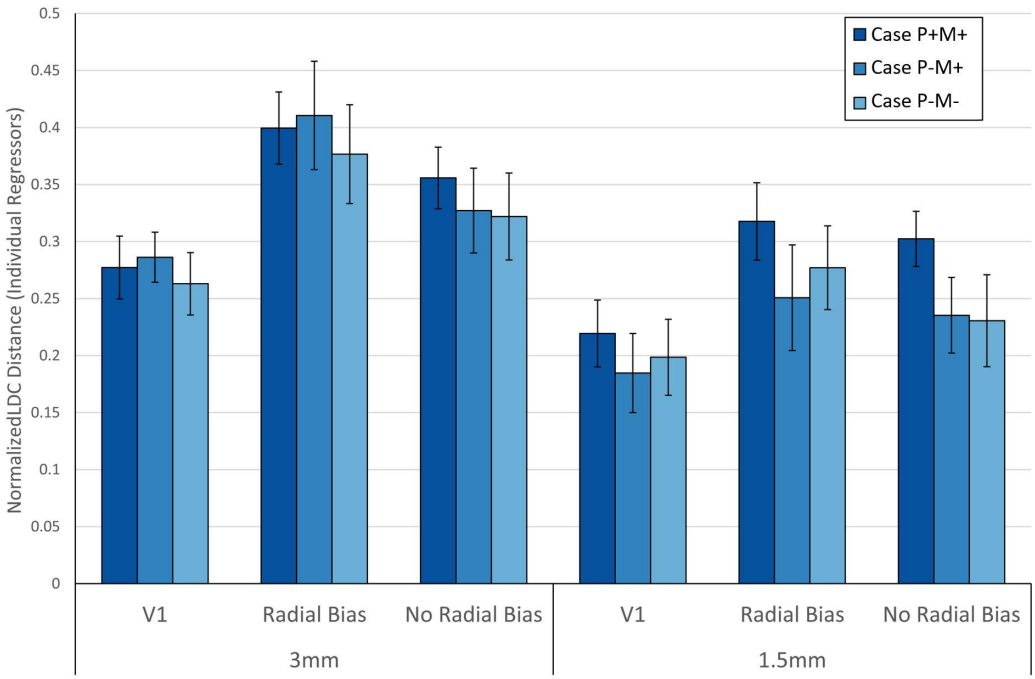

Figure 4-4: Plot of normalized LDC distance, using individual regressors, per case, resolution and ROI. The distance measures were averaged across all 15 participants. Error bars indicate standard error over participants.

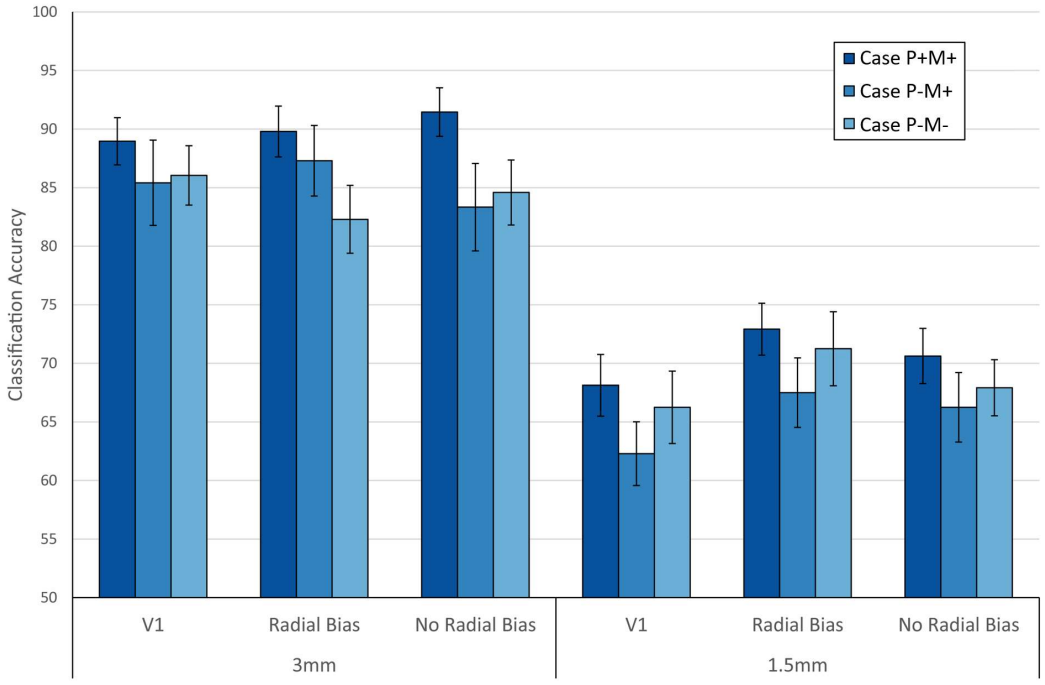

*Figure 4-5: **Plot of classification accuracy using SVM per case, resolution and ROI. The classification accuracies were averaged across all 15 participants. Error bars indicate standard error over participants.***

Lastly, SVM classification (Figure 4-5) shows a numerical benefit of case P+M+ for all cases, both resolutions and all three ROIs. However, under a repeated measures ANOVA (Supplementary Table 4-2), these differences were shown to be not significant. There is only a significant main effect of resolution ($F(1,14)=135.3$, $p=1.39*10^{-8}$), indicating that the classification accuracy for the 1.5mm data is significantly worse than the classification accuracy for the 3mm voxels.

4.4.2 Computer Simulations

My simulation results show a good agreement with the fMRI data. The plots (Figure 4-6) illustrate the rejection probabilities of the comparison between two datasets with varying fCNR using the various metrics. The rejection probability is obtained by calculating the proportion of 100 simulated iterations that yielded a significant paired t-test ($p<0.05$) for the given fCNR pairing. In this context, higher rejection probability for a given method indicates higher sensitivity to changes in fCNR. For the colour scale utilized in Figure 4-6, a metric with perfect sensitivity to any changes in fCNR would reject all cases when the fCNR are not equal, producing a plot with yellow squares in all off-diagonal cells and a strip of dark blue squares along the diagonal. In contrast, a metric that is insensitive to changes in fCNR would show dark blue cells across the entire plot.

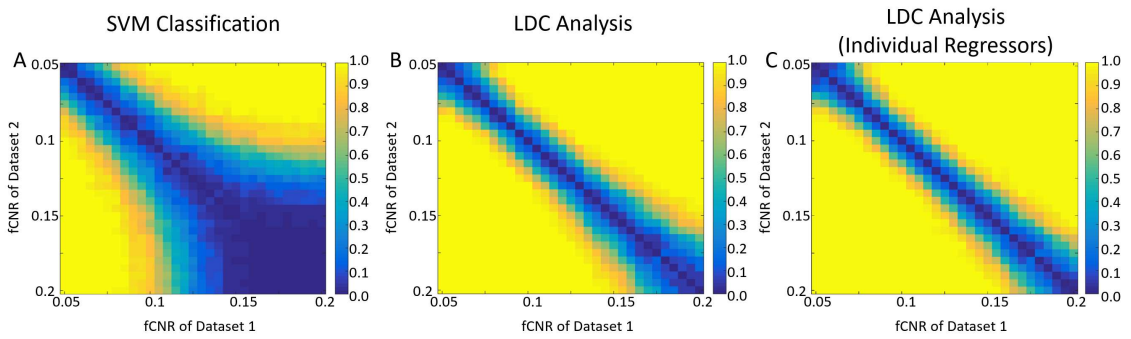

Figure 4-6: Heatmaps of the rejection probability of the null hypothesis of no significant differences between fCNR when comparing two datasets with the respective fCNRs over 100 iterations. This was repeated with three different metrics— SVM classification (Panel A), LDC analysis (Panel B) and LDC analysis with individual regressors (Panel C). A value of 1 indicates that the null hypothesis is rejected for all 100 iterations while a value of 0 indicates the null hypothesis is not rejected for all 100 iterations.

I observe that the SVM classification accuracy is much less sensitive than both LDC metrics, as seen by higher rejection probability of the null hypothesis for the same change in fCNR for LDC. This difference in sensitivity is amplified at regions with higher fCNR, as seen by the fanning out of the blue regions (low rejection probabilities) in the SVM heatmap at high fCNR. LDC analysis with a single regressor shows very similar results as LDC analysis with individual regressors, with the latter performing marginally better. This is in conflict with my expectations from theory and the fMRI data and could be due to failure of the model to capture all aspects of the noise.

4.5 Discussion

In this chapter, I compared SVM classification with LDC analysis and demonstrated that LDC is more sensitive to changes in noise for both real and simulated fMRI data. For real fMRI data, standard LDC analysis was able to show a significant improvement in data quality when PMC is applied to high resolution fMRI data, while LDC analysis with individual regressors and SVM classification were only able to show a numerical (but insignificant) trend of PMC-corrected data performing better. This is in line with the theoretical expectations of LDC being a more sensitive metric than SVM, as described in Section 4.2. LDC analysis with individual regressors demonstrated similar trends as standard LDC analysis, albeit with lower LDC values. This supports my assertion that utilizing individual regressors results in less stable estimates of the contrast and is agreement with previous work (Abdulrahman and Henson, 2016).

My computer simulations also show a similar increase in sensitivity for LDC compared to SVM. This difference is present throughout the range of fCNR, and becomes more pronounced at higher fCNR, likely due to ceiling effects decreasing the sensitivity of SVM in that regime. The LDC results with individual regressors seemed to be more sensitive compared to standard LDC analysis, in direct contrast with my theoretical expectations and the fMRI results. I believe that this is because my model did not account for all sources of noise. I assumed that all sources of noise remained constant across sub-runs. However, this might not be accurate since other factors such as participant's motion between sub-runs and scanner drifts can affect the relative amounts of noise. Moreover, the amount of noise added per block at the activations level was arbitrarily set at unity. It is possible that higher amount of variance per block would decrease the stability of the estimates from LDC with individual regressors.

Together, my fMRI and simulation results support my theoretical assertions of the benefits of utilizing LDC over SVM. This supports and extends previous work on the benefits of LDC on fMRI data. Mandelkow et al., 2016 showed that LDC is able to achieve the highest classification accuracy of a wide range of movie stimuli as compared to other algorithms such as Gaussian Naïve Bayes (GNB) and k-Nearest Neighbours (kNN). However, they did not include conventional SVM classification in their analysis due to the large number of stimuli classes, which SVM does not handle well. Misaki et al., 2010 tested six different classification methods (KNN, GNB, LDC, pattern-correlation classifier, linear SVM and SVM with a radial-basis function kernel). Their results showed that linear classifiers outperformed the non-linear classifiers, suggesting that non-linear classifiers are overfitting the data. They also showed that LDC achieved the best classification accuracy, which is in agreement with my findings here.

It is important to note that I am only comparing the sensitivity of the two metrics here. There are also other metrics of comparison that are not accounted for here. LDC assumes that the magnitude of noise remains constant throughout the experiment, with an underlying correlation across voxels that can be exploited by the covariance matrix. However, if these assumptions do not hold true (such as in realms where thermal noise dominates with heavy fluctuations), it is possible that SVM might perform better. Moreover, while the usage of a sparse covariance matrix greatly reduces the computation time for the inversion of the noise matrix, it can still become computationally costly for large ROIs (>1000 voxels). This could also be addressed by the usage of searchlights instead of the whole ROI for LDC (Kriegeskorte et al., 2006; Ontivero-Ortega et al., 2015).

4.6 Conclusion

The feat of compressing large amounts of raw fMRI data into a few singular numerical metrics for comparison is not only a difficult task, but also one in which utmost care needs to be taken to ensure that useful information is not lost in the process. MVPA has been shown to be a very powerful tool for fMRI analysis, being able to provide increased sensitivity and unmasking pattern information stored in activation maps. In this chapter, I show that LDC outperforms SVM as a MVPA metric in terms of sensitivity and justify the usage of LDC throughout the rest of the thesis.

4.7 Supplementary Materials

	Sum of Squares	DF	Mean Square Error	F	p
(Intercept)	22.835	1	22.835	181.79	2.07E-09*
Error	1.7585	14	0.1256		
(Intercept):Resolution	0.5359	1	0.5359	12.068	0.0037*
Error(Resolution)	0.6217	14	0.0444		
(Intercept):Case	0.0615	2	0.0308	0.9063	0.4156
Error(Case)	0.9502	28	0.0339		
(Intercept):Region	0.4578	2	0.2289	10.789	0.0003*
Error(Region)	0.5940	28	0.0212		
(Intercept):Resolution:Case	0.0325	2	0.0163	1.0024	0.3798
Error(Resolution:Case)	0.4540	28	0.0162		
(Intercept):Resolution:Region	0.0208	2	0.0104	2.1061	0.1406
Error(Resolution:Region)	0.1383	28	0.0049		
(Intercept):Case:Region	0.0125	4	0.0031	0.7588	0.5565
Error(Case:Region)	0.2300	56	0.0041		
(Intercept):Resolution:Case:Region	0.0082	4	0.0020	0.6939	0.5994
Error(Resolution:Case:Region)	0.1647	56	0.0029		

*Supplementary Table 4-1: Repeated measures ANOVA results for LDC distance (individual regressors). * indicates p<0.05 (corrected for multiple comparisons, Tukey's HSD test).*

	Sum of Squares	DF	Mean Square Error	F	p
(Intercept)	1.62E+06	1	1.62E+06	3113.2	7.56E-18*
Error	7264.4	14	518.89		
(Intercept):Resolution	22975	1	22975	135.3	1.39E-08*
Error(Resolution)	2377.2	14	169.8		
(Intercept):Case	1234	2	617.01	1.5679	0.2262
Error(Case)	11019	28	393.52		
(Intercept):Region	243.56	2	121.78	1.5355	0.2329
Error(Region)	2220.6	28	79.308		
(Intercept):Resolution:Case	233.58	2	116.79	0.7888	0.4642
Error(Resolution:Case)	4145.8	28	148.06		
(Intercept):Resolution:Region	323.86	2	161.93	3.0894	0.0613
Error(Resolution:Region)	1467.6	28	52.414		
(Intercept):Case:Region	107.78	4	26.946	0.9255	0.4558
Error(Case:Region)	1630.5	56	29.116		
(Intercept):Resolution:Case:Region	186.78	4	46.694	2.0529	0.0993
Error(Resolution:Case:Region)	1273.7	56	22.745		

*Supplementary Table 4-2: Repeated measures ANOVA results for classification accuracy. * indicates p<0.05 (corrected for multiple comparisons, Tukey's HSD test)*

5 3T vs 7T: Analysing differences due to field strength using an attention paradigm

5.1 Abstract

3T MRI scanners are currently the main workhorse for MRI research, but more and more 7T MRI scanners are emerging around the globe. Given the high cost of setting up and acquiring data on the 7T scanners, it is important to identify the benefits of using 7T MRI over 3T MRI scanners for fMRI studies. Here, I used a visual attention paradigm to demonstrate that both 3T and 7T GE EPI were able to detect spatial and categorical selectivity responses across all visual ROIs and showed similar results, with no clear advantage in terms of sensitivity for 7T. However, the 7T data was acquired at a much higher resolution, and thus would be needed for analysis of laminar layers or columns.

5.2 Introduction

Since the first whole-body human MRI scanner (MRI Scanner Mark One) was built by John Mallard team in Aberdeen (Mallard et al., 1979), the quality of MRI scanners have improved in leaps and bounds, both in terms of image quality and field strength. While the first few MRI scanners did not even exceed a single tesla in field strength, today 1.5T and 3T scanners have become commonplace for clinical use, with the first 7T scanner (Siemens 7T Terra) being cleared for clinical use in late 2017 (Caccomo, 2017). In late 2018, the Minnesota 10.5T MRI scanner was cleared for human use and the first human was scanned at 10.5T (Nowogrodzki, 2018). Pushing the envelope even further, two sites (US National Institute of Health (NiH), Maryland and NeuroSpin Centre, France) are in the process of setting up their own 11.7T scanners. A quick search on PubMed of the terms “1.5T MRI”, “3T MRI” and “7T MRI” from 2010 onwards demonstrate that the majority of MRI research is currently conducted at fields strengths of 3T, while 7T MRI has been picking up interest in recent years. Currently, there are over 70 7T MRI scanners operational worldwide.

The appeal of going towards higher field strengths is apparent. With higher field strengths, researchers are able to obtain a much stronger SNR for the same voxel size and acquisition time. Thus, it is possible to acquire submillimetre voxels while maintaining a reasonable SNR, allowing researchers to probe the finer structures of the brain, such as cortical layers and columns. Stucht et al., 2015 showed some beautiful images of the resolution that can be achieved with 7T MRI with PMC. Submillimetre resolution is needed for researchers to probe the brain for differences across cortical columns and layers given that the thickness of the cortex varies from 2mm to 5mm depending on the brain region.

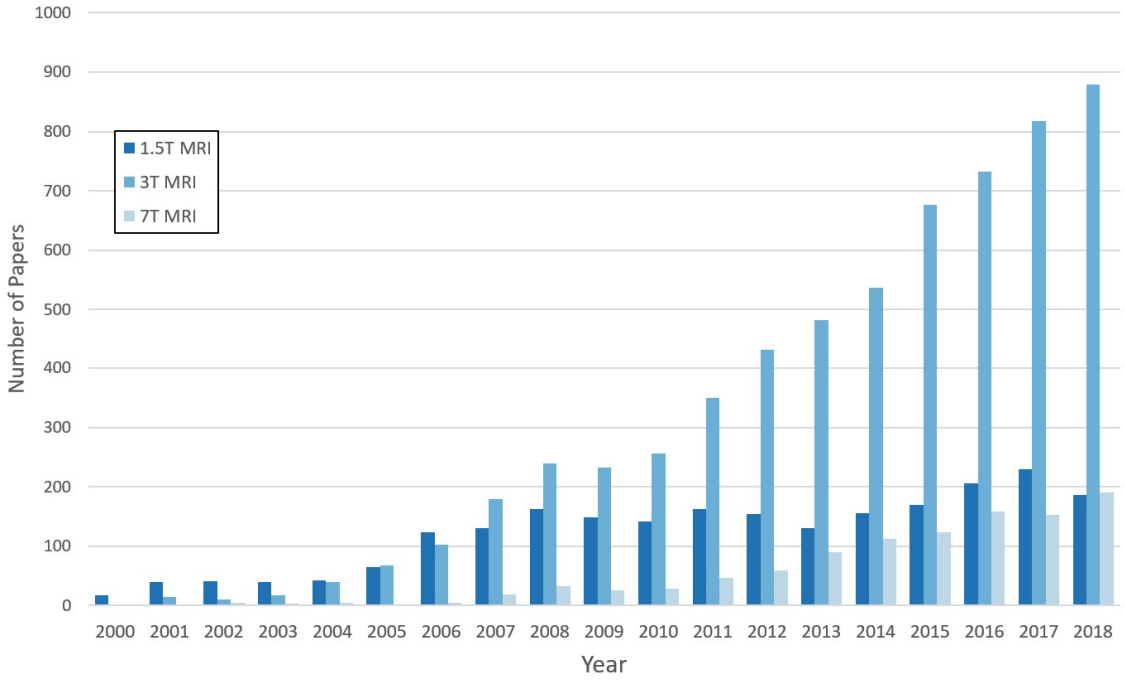

Figure 5-1: Plot of the number of papers on PubMed with the text "1.5T MRI", "3T MRI" and "7T MRI" present. This provides a rough gauge of the amount of research being carried out on scanners with various field strengths.

However, the higher resolution of 7T also causes the images to be more sensitive to any motion. Even the best trained participants will have small drifts across time and unavoidable physiological motion due to respiration and heartbeat (Maclaren et al., 2012), which might have a larger impact on 7T data. Moreover, most 7T studies (including the present study) only acquire partial brain volumes. Thus, any motion can result in the loss of information in edge voxels. Secondly, the higher magnetic field also amplifies the geometric distortions due to magnetic field inhomogeneities, resulting in more artefacts. Lastly, RF pulses with shorter wavelengths (hence higher energy) are needed to excite the hydrogen nuclei at higher fields. This results in higher SAR for the sequences, and thus might require compromises or alterations of the sequences used to ensure that the MRI scan does not cause any tissue overheating (Olman and Yacoub, 2011).

As such, it is not immediately obvious that the data acquired on the 7T scanner will be inherently better than the data acquired on the 3T scanner, especially if the higher resolution is not necessary for the analysis. In this chapter, I present the results from a visual attention study that was carried out on both a 3T Prisma scanner and a 7T Terra scanner and compare the quality of the data obtained. The images acquired at both scanners were obtained using 2D GE-EPI sequences and the same six participants were scanned at both scanners. The exact same experimental paradigm was repeated

across scanners to ensure that any differences observed were due to the scanner and sequence differences.

I chose a visual attention paradigm for this task. Concurrently, I wanted to probe the segregation of location and categorical selectivity across the visual ROIs. The standard two-streams hypothesis was proposed in the seminal paper by Ungerleider and Mishkin, 1982. Their work suggested that the dorsal stream is primarily concerned with the location of the stimulus ('where') while the ventral stream is primarily concerned with the identity of the stimulus ('what'). However, this definition has been continuously revised and re-evaluated over time (Freud et al., 2016), especially in light of a growing body of work (Bracci and Op de Beeck, 2016; Vaziri-Pashkam and Xu, 2017) demonstrating categorical effects in the dorsal stream and location representations in the ventral stream.

5.3 Methods

5.3.1 Experimental Design

I utilized the visual attention task described in Section 2.1.2 and acquired data at both 3T and 7T. Briefly, I permutated four task types across runs (four runs of each task type)— task with distractors present (TaskD+), task without distractors (TaskD-), fixation with distractors present (FixD+) and fixation without distractors (FixD-). Conditions involving the presence of distractors were alternated between runs, while the context of the task was permutated across sessions (i.e. participants attended one session with alternating runs of task types FixD+ and FixD- and another session with alternating runs of task types TaskD+ and TaskD-). Note that when distractors were present, the distractors were taken from the opposite category and presented in the opposing spatial location. I expect to see consistent contrasts in all task types except FixD+, where all contrasts should be close to zero if the stimuli is properly counterbalanced. Within each run, I permutated four stimuli conditions (five blocks of each condition per run)— attending to houses at 45° and 225° (H^{45}), attending to faces at 45° and 225° (F^{45}), attending to houses at 135° and 315° (H^{135}) and attending to faces at 135° and 315° (F^{135}). These four permutations of conditions allowed me to extract both location and categorical selectivity.

Also, it is important to note that the size and position of stimuli presentation was different across scanners. In 3T, the stimuli spanned from -3.87° to +3.87° visual angle, while in 7T, the stimuli spanned from -2.42° to +2.42° visual angle, with a vertical shift up by 2° due to obstruction of the lower half of the visual field by the head coil.

5.3.2 Data Acquisition

Participants provided informed consent under a procedure approved by the institution's local ethics committee (Cambridge Psychology Research Ethics Committee). Six participants (two females, age range 20-41) were scanned for two sessions each at both the Siemens 3T Prisma-Fit scanner and the Siemens 7T Terra scanner. The two sessions (one session of task runs, and one session of fixation runs) was repeated at 3T and 7T. Due to logistical constraints, both 3T sessions were carried out prior to the 7T sessions for all participants. In addition, one additional session for localizers was acquired at 3T, as described in Section 2.1.2.

Prior to the experiment, participants underwent behavioural training with eyetracking using an SMI high speed eye tracker. The participants attempted the same task and received feedback on their fixation levels after each run. This was repeated until the participant was able to fixate consistently (<0.5^{o} visual angle difference between the attended and the non-attended axis) for 2 consecutive runs. As eyetracking was not available in the 7T scanner, the behavioural training was important to ensure that participants were able to perform the task while maintaining fixation.

The EPI parameters for the 3T data were as follows: 3mm isotropic voxels, TR=2000ms, TE=30ms, FA=78^{o}, Matrix size=64*64*32, ToA=~11mins. The EPI parameters for the 7T data were as follows: 0.8mm isotropic voxels, TR=2390ms (2440ms for two participants), TE= 24ms (24.4ms for two participants), FA=80^{o}, GRAPPA = 3, Matrix size= 200*168*84, ToA=~11mins. The two participants used a longer TE and TR due to the peripheral nerve stimulation threshold being exceeded in the scanner.

5.3.3 Data Analysis

MRI Data Post-processing

The 3T data underwent the standard post-processing in SPM as described in Section 2.3.1. The 7T underwent similar post-processing, with the addition of TOPUP, also described in the same section. In addition, each fMRI volume was individually realigned to the structural using Boundary-Based Registration (BBR) (Greve and Fischl, 2009). This process used the structural as a reference to ensure that the volumes are realigned with each other. This method was chosen because it provided the best realignment within and across runs, as shown in Chapter 6.

The ROI segmentation was described in Section 2.3.3.

Spatial and Categorical Selectivity

I used spatial and categorical selectivity as the metric of interest. First, the postprocessed data from all four runs with the same task type were combined. I generated a GLM that modelled responses to each of the four different attention conditions with linear and first-order sinusoidal nuisance regressors. The combined data was fitted to the GLM with ordinary least squares (OLS) regression to produce a beta estimate for each of the four conditions. This allowed me to extract both location selectivity (by taking the mean of F^{45} and H^{45} estimates and subtracting the mean of F^{135} and H^{135} estimates) and categorical selectivity (by taking the mean of F^{45} and F^{135} estimates and subtracting the mean of H^{45} and H^{135} estimates) for each ROI. The signs of the selectivity estimates were flipped to align with the region's expected preference (e.g. $F^{45}+F^{135}-H^{45}-H^{135}$ for FFA and $H^{45}+H^{135}-F^{45}-F^{135}$ for PPA). For retinotopic ROIs, each ROI was segmented into quarter-field maps (e.g. V1 into V1d and V1v for left and right hemispheres individually) and the signs of the selectivity estimates were flipped to align with each quarter-field map's expected preference. The quarter-fields were then re-combined and plotted as a single ROI in the analysis. For categorical selectivity, the signs of the selectivity estimates were flipped to align with each ROI's expected preference. Note that I only tested retinotopic ROIs for spatial selectivity and categorical ROIs for categorical selectivity as there are priors for the expected preference.

5.4 Results

5.4.1 3T ROI results

The 3T data was plotted in Figure 5-2. For task type TaskD+, strong spatial selectivity was observed in all the retinotopic ROIs (V1, V2 and V3). Strong categorical selectivity was also observed in the categorical ROIs (TOS, PPA, OFA and FFA). This data demonstrates that spatial attention was represented in the early visual areas, while categorical attention was represented in the higher visual areas, along both the dorsal and ventral streams.

For task type FixD+, no consistent difference was observed across all ROIs for both category and location selectivity. This indicates that my stimuli were properly counterbalanced and there is no stimuli representation in the distractor present cases. This also affirms that the effects observed in task type TaskD+ reflected attention modulation effects.

For task type TaskD-, similar trends were observed as that of task type TaskD+, but with a higher magnitude. V1, V2 and V3 demonstrated consistent location selectivity while strong category selectivity was observed in TOS, PPA, OFA and FFA. The higher magnitudes were expected since the

lack of distractors meant that this combined selectivity metric is representing both attention modulation and stimuli representation effects.

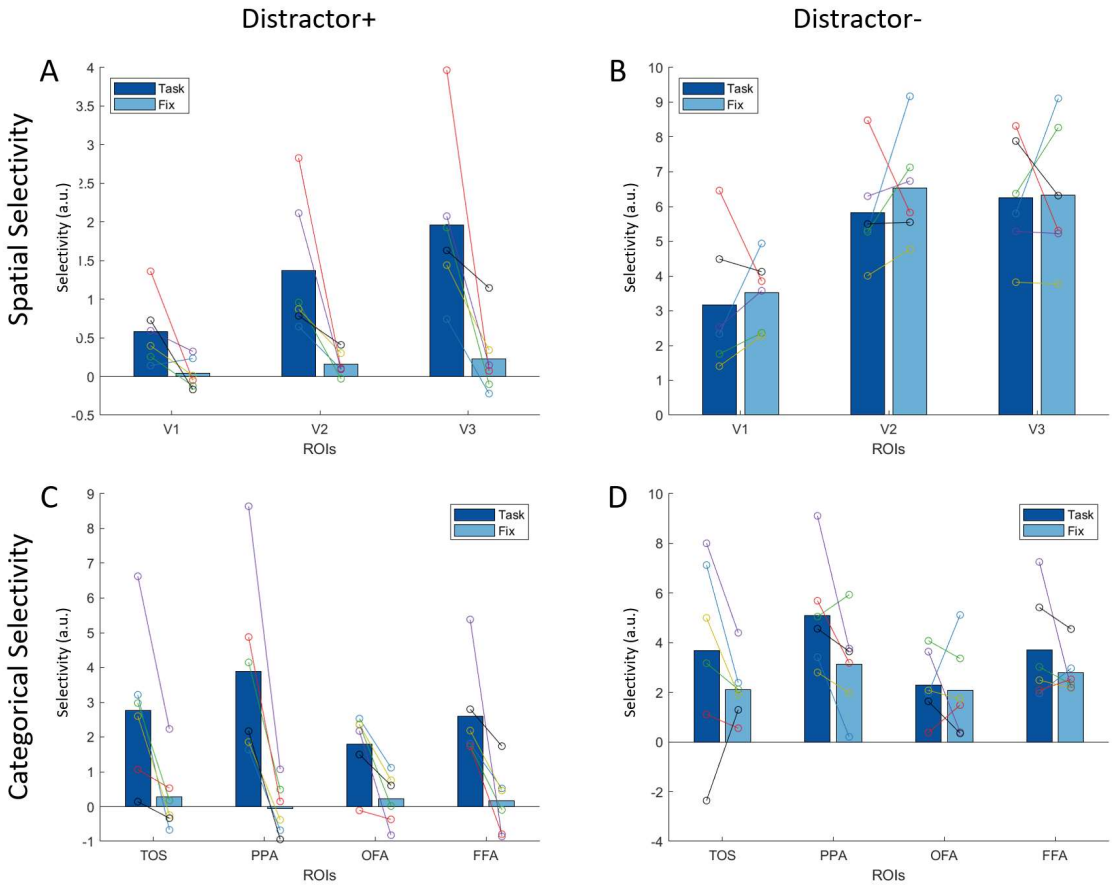

1700 *Figure 5-2: Plots of the two selectivity estimates across the visual ROIs at 3T under the different task types: location selectivity with distractors (Panel A), location selectivity without distractors (Panel B), category selectivity with distractors (Panel C) and category selectivity without distractors (Panel D). The bars represent the average of all six participants, with the blue bars representing the task runs and the teal bars representing the fixation runs. Each pair of joint circles represent an individual subject, with the same colour representing the same participant throughout all plots. Note that the sign of the contrast is flipped such that a positive contrast indicates the ROI responds to the expected preference (e.g. faces for OFA and FFA and houses for TOS and PPA)*

For task type FixD-, I observed similar results to that of task types TaskD+ and TaskD- — stimuli-driven location selectivity in V1, V2 and V3 and stimuli-driven categorical selectivity in TOS, PPA, OFA and FFA. These results suggest that attention modulation and stimuli representation engaged similar ROIs. Interestingly, the magnitude of selectivity estimates for task type FixD- was lower than that of the task type TaskD- estimates for categorical ROIs, whereas for spatially-selective ROIs, the magnitude of the task type FixD- response was comparable to that of the task type TaskD- response. If I assume that the selectivity exhibited in task type TaskD- reflects both stimuli representation and attention modulation

effects while the task type FixD- selectivity is purely driven by stimuli representation, the response to task type TaskD- should be consistently larger than the response to task type FixD- within each ROI.

5.4.2 7T ROI results

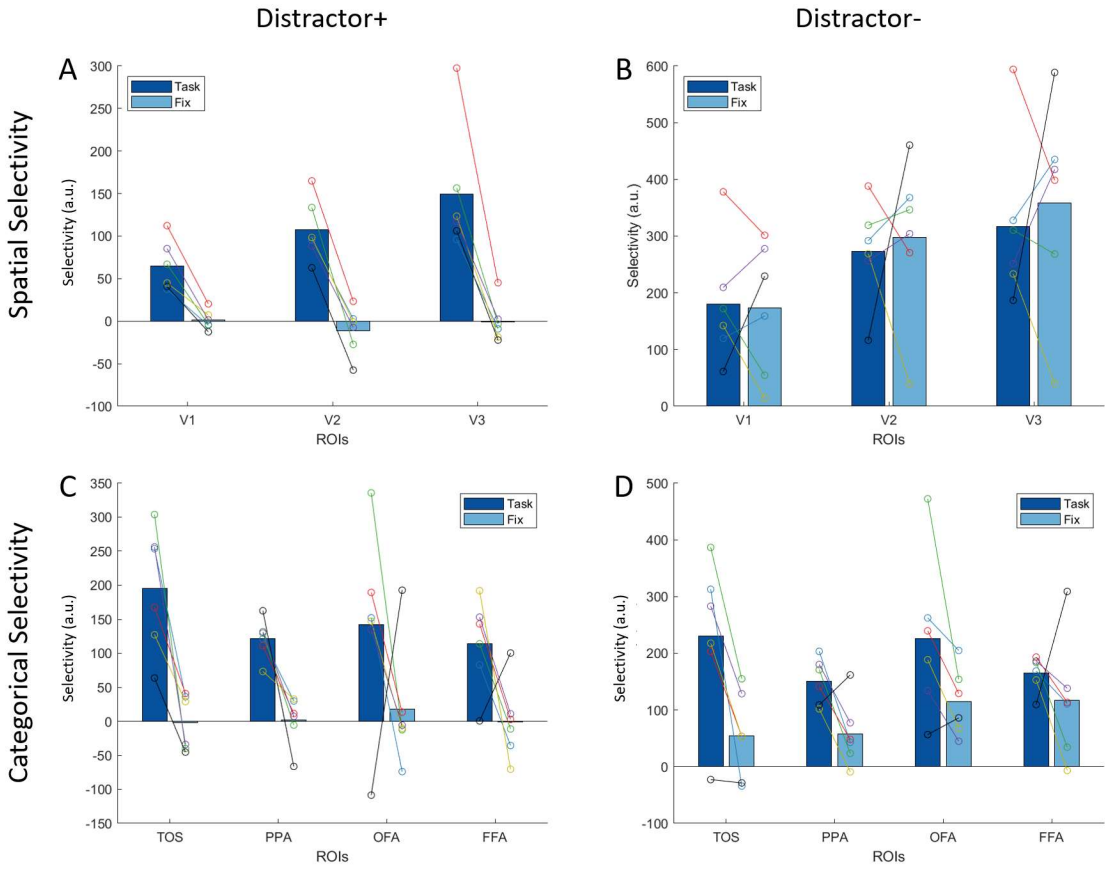

Figure 5-3: Plots of the two selectivity estimates across the visual ROIs at 7T under the different task types: location selectivity with distractors (Panel A), location selectivity without distractors (Panel B), category selectivity with distractors (Panel C) and category selectivity without distractors (Panel D). The bars represent the average of all six participants, with the blue bars representing the task condition and the teal bars representing the fixation condition. Each pair of joint circles represent an individual subject, with the same colour representing the same participant throughout all plots. Note that the sign of the contrast is flipped such that a positive contrast indicates the ROI responds to the expected preference (e.g. faces for OFA and FFA and houses for TOS and PPA)

The 7T results were plotted in Figure 5-3. For task type TaskD+, I observed a strong attention-driven location selectivity in V1, V2 and V3 while the higher visual areas did not exhibit any location selectivity. TOS, PPA, OFA and FFA all exhibit strong attention-driven categorical selectivity and the early visual areas show no categorical selectivity. These trends were similar to what was observed at

3T. The runs of task type FixD+ showed no consistent selectivity for both location and category across all ROIs, similar to the 3T results.

Similar to the 3T case, the task type TaskD- data at 7T exhibited the same behaviour as the task type TaskD+, but with a higher magnitude. Strong location selectivity was observed in V1, V2 and V3 while TOS, PPA, OFA and FFA all exhibited strong categorical selectivity. I expect the runs of task type TaskD- to reflect to both attention modulation and stimuli representation, which would explain the higher selectivity magnitudes relative to task type TaskD+ which solely represented attention modulation.

For task type FixD-, I observed strong stimuli-driven location selectivity in V1, V2 and V3 and strong categorical selectivity in TOS, PPA, OFA and FFA, again echoing what was observed at task type TaskD+ and TaskD-. Similar to the 3T results, the location selectivity response in V1, V2 and V3 for FixD- was close in magnitude to the response in task type TaskD- while the categorical selectivity in TOS, PPA, OFA and FFA was significantly larger in task type TaskD- relative to task type FixD-.

Taken together, these results were highly consistent with the 3T data, exhibiting similar trends across ROIs and task types. It was interesting to note that the selectivity magnitudes were approximately 50 times larger in 7T relative to 3T. However, this increase in selectivity magnitude was accompanied by a similar increase in between-subject variance (approximately 50 times as well).

5.4.3 Qualitative comparison of 3T and 7T ROI results

Across all ROIs and task types, there was a good correlation between the 3T and 7T contrast estimates. Scatterplots of location and categorical contrast of 3T against 7T was generated using the ROIs with expected attention selectivity to the respective contrast (V1, V2 and V3 for spatial selectivity and TOS, PPA, OFA and FFA for categorical selectivity) and is shown in Figure 5-4. For each scatterplot, I obtained the best fit line using Deming regression, which accounts for noise in both the dependent and independent variable. ROIs that demonstrate a strong contrast at 7T also demonstrate a strong contrast at 3T for TaskD+, TaskD- and FixD- task types. For task type FixD+, the points were randomly distributed around zero, an expected behaviour since there should be no underlying difference to pick up on. These results indicate that both 3T and 7T scans were able to pick up on the same selectivity responses for all ROIs, despite the 7T data being acquired with 64x smaller voxels.

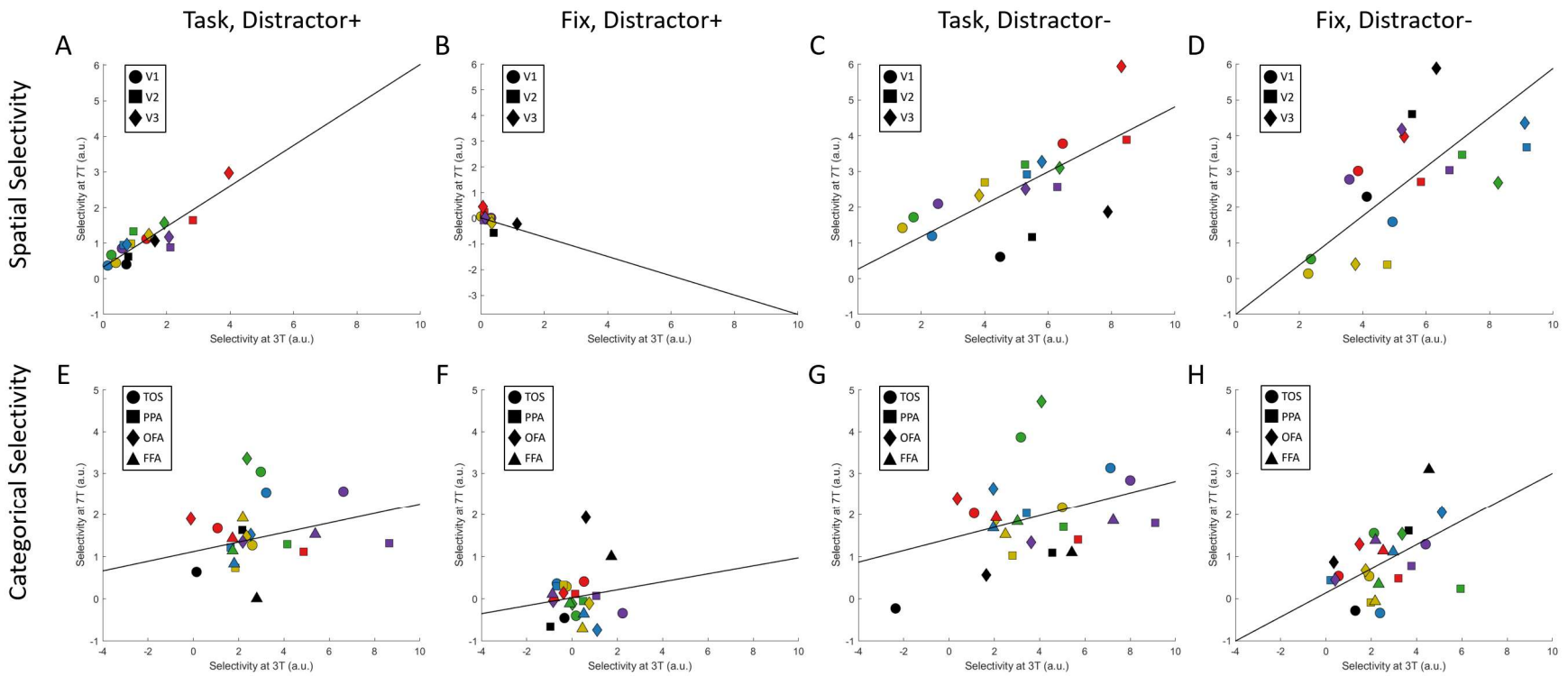

Figure 5-4: Comparison plots of contrasts obtained at 7T against the contrasts obtained at 3T. The 7T data was divided by 100 so as to be on the same scale as the 3T data to allow the Deming regression to converge properly. Panels A-D compare location selectivity across scanners under the different run types: task with distractor (Panel A), fixation with distractor (Panel B), task without distractors (Panel C) and fixation without distractors (Panel D). Panels E-H compare category selectivity across scanners under the different run types: task with distractor (Panel E), fixation with distractor (Panel F), task without distractors (Panel G) and fixation without distractors (Panel H). The black line represents the best fit line obtained by Deming regression and the R-squared value is included in the plot. Each shape represents a different ROI while each colour corresponds to a different participant. Graphs within the same row are scaled to the same axis.

5.5 Discussion

In this chapter, I showed that results obtained from both 3T and 7T scanners were similar. ROIs exhibited attention and stimuli-driven selectivity for the same visual property across scanners, with similar activation profiles across conditions and task types. Even subtle trends were consistent across scanners, such as task type TaskD- selectivity being greater than task type FixD- selectivity in categorical ROIs while exhibiting comparable selectivity for retinotopic ROIs. These results showed that both scanners were picking up on similar activations and no additional information was present in the 7T data.

The magnitude of the selectivity responses was substantially different across scanners, with approximately a 50-fold increase for 7T data. However, this increase was accompanied by a similar increase in between-subject variance. Thus, it would be difficult to predict whether the 7T scanner would be more sensitive to smaller effects than 3T.

While I was unable to ascertain the benefits of 7T in terms of sensitivity, the 7T data was acquired at a much higher resolution (0.8mm isotropic vs 3mm isotropic voxels). Given that both datasets showed similar sensitivity, the higher resolution of the 7T data would allow researchers to probe smaller brain structures, such as cortical columns or layers while being reassured that there is little to no loss of signal relative to a 3T acquisition at the lower resolution. In addition, note that it is possible to acquire 7T data at lower resolutions, which could confer advantages in signal strength and sensitivity (Sengupta et al., 2017). Further work by the same group (Sengupta et al., 2018) showed that when resolution were matched across 3T and 7T scanners, data acquired from the 7T scanner had higher classification accuracy.

For the neuroscience segment of this study, I observed strong location selectivity in the early visual area and strong categorical selectivity in the higher-visual areas, along both ventral and dorsal streams for both 3T and 7T. These results suggest that the classic dorsal-ventral segregation of “where” and “what” (Ungerleider and Mishkin, 1982) provides only a partial explanation for the functional organization of visual processing and that the large-scale organization for spatial and categorical selectivity appears to also have an anterior-posterior axis, similar to results observed in previous studies (Bracci and Op de Beeck, 2016; Vaziri-Pashkam and Xu, 2017).

Moreover, I also noted that the ROIs exhibited similar category and location selectivity across task types TaskD+, TaskD- and FixD-. This provided evidence that each ROI demonstrates stimuli preference and attention modulation for identical visual properties, similar to the results observed in Kanwisher, O’Craven, & Downing, 1999 for the higher visual areas. For example, regions V1, V2 and V3, which

were activated when participants attend to different spatial regions (task type TaskD+), were also activated when the stimulus differ spatially (task type FixD-).

I also observed that the selectivity responses in task type TaskD- were consistently larger for all ROIs relative to the selectivity exhibited in task type TaskD+. This is in line with my expectations as the task type TaskD- selectivity response arises as a combination of attention modulation and stimuli representation, whereas the task type TaskD+ selectivity was a result of pure attention modulation. I expect the two effects to have a combinative effect, potentially additive, based on their relative magnitudes. Similarly, the selectivity responses in task type FixD- was smaller than the responses in task type TaskD- for categorical ROIs, supporting the assertion that attention modulation and stimuli representation has a combinative effect.

However, the spatially selective ROIs in task type FixD- showed similar, or higher, response magnitudes as compared to the response in task type TaskD- for both 3T and 7T, contrary to my expectations based on the above theory. A possible explanation could be due to the slight increase in eye motion in the runs of task type TaskD- relative to the runs of task type FixD- (Supplementary Figure 5-1). Thus, the retinotopic representations in task type TaskD- would be less robust compared to task type FixD-, resulting in a lower selectivity response. The categorical ROIs were less affected by the increased eye motion because only stimuli from the attended category was present for both task types FixD- and TaskD-. Thus, the same category of stimuli would still be present regardless of eye movement and the stimuli representation for categorical ROIs would be minimally affected. While eyetracking data was only available at 3T, it is not a stretch to assume that similar difference in eye motion would be present at 7T given that the stimuli and experimental conditions were otherwise identical. In addition, the runs of task type FixD- were conducted in a separate session from the runs of task type TaskD-, and between-session noise would be a possible additional confound, reducing the difference between runs of task type FixD- and TaskD-.

5.6 Conclusion

I showed that data acquired at 3T (3mm isotropic voxels) and 7T (0.8mm isotropic voxels) yielded similar and consistent results and neither scanner showed significant benefits in terms of sensitivity. However, the higher resolution afforded by the 7T scanner would be useful in probing laminar layers or other cortical structures, which would not be visible at 3mm resolution. In addition, I also demonstrated that there exists an anterior-posterior segregation for spatial and categorical selectivity and that the same ROIs were recruited for stimuli representation and attention selectivity for the same visual property (location or category).

5.7 Supplementary Materials

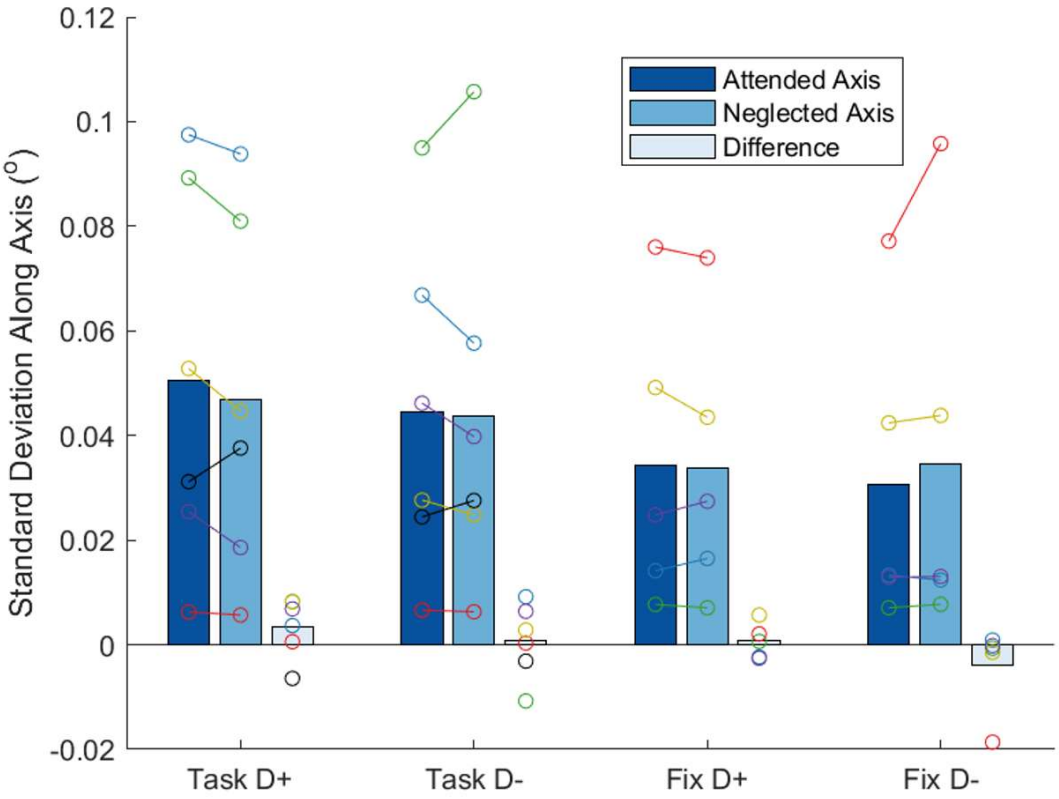

Supplementary Figure 5-1: Plot of the standard deviation of the eye movement of the six participants along the attended axis, the neglected axis and the difference between the two axis. The eye movement was measured in degrees visual angle. Each set of connected circles indicate an individual participant. Due to technical issues, eyetracking data was unavailable for one of the participants (black) during the fixation session. While this data shows that there is no significant difference between eye movement along the attended and neglected axis, there is poorer fixation for task type TaskD+ and TaskD- relative to task types FixD+ and FixD-. This difference in fixation could be part of the explanation of why stronger selectivity was observed in FixD- relative to TaskD- for retinotopic ROIs.

6 BBR Realignment

6.1 Abstract

Moving towards higher field strengths has allowed researchers to acquire fMRI data with submillimetre voxels. However, in order to interpret the data clearly, accurate correction of head motion and the resultant distortions is crucial. In this chapter, I presented a novel application of Boundary Based Registration (BBR) to realign fMRI data and evaluated its effectiveness on a set of 7T submillimetre data. I also tested the effectiveness of BBR on millimetre 3T data for comparison. BBR utilizes the boundary information from high contrast present in structural data to drive registration of functional data to the structural data. In my application, I realigned each functional volume individually to the structural data, effectively realigning them to each other. In addition, this realignment method removes the need for a secondary aligning of functional data to structural data for purposes such as laminar segmentation or registration to data from other scanners. I demonstrated that BBR realignment outperforms standard realignment methods across a variety of data analysis methods. Further analysis shows that this benefit is an inherent property of the BBR cost function and not due to the difference in target volume. My results showed that BBR realignment is able to accurately correct head motion in 7T data and can be utilized in preprocessing pipelines to improve the quality of 7T data.

6.2 Introduction

Participant motion is a significant confound in functional magnetic resonance imaging (fMRI) (Andre et al., 2015), and this problem is further exacerbated when data is acquired at higher field strengths and submillimetre resolution (Maclaren et al., 2010). Even the best trained participants will often have unavoidable drift and unconscious motions due to respiratory (~1mm) and cardiac activity (~100um) (Maclaren et al., 2012) which can impact data quality (Hutton et al., 2011), especially at higher resolutions. Participant motion is a multi-faceted problem that is persistent in fMRI studies (Friston et al., 1996) and results in degrading data quality in a multitude of ways. Participant motion can affect the magnetic field, in turn causing distortions (Jezzard and Clare, 1999) and intensity variations (Friston et al., 1996) in the acquired volumes. Motion artefacts can also affect the image in non-rigid ways and hence, standard rigid body realignment techniques might not be sufficient. Since field inhomogeneities scales with field strength, the aforementioned distortions will also become amplified at higher fields.

Furthermore, submillimetre resolution voxels also increase the impact of participant motion. While smaller voxel sizes are useful for analysis of brain substructures (e.g. cortical layers), they are also more susceptible to motion, as the magnitude of the motion becomes larger relative to the voxel size. As most fMRI analyses assume that the same voxel corresponds to same location in the brain throughout the session. This assumption is invalidated by motion and could result in missed effects and/or false positives (Field et al., 2000; Schulz et al., 2014). Moreover, studies acquiring data at sub-millimetre resolutions generally only obtain partial brain volumes to maintain a reasonable repetition time (TR). This compounds the problem because the reduced field-of-view provides less information to drive the realignment. As such, I believe that the conventional realignment methods currently used might be insufficient to ensure the quality of submillimetre data. Numerous improvements have been suggested and implemented, both at the acquisition stage (Huang et al., 2018; Todd et al., 2015) and the post-processing stage (Gallichan et al., 2016; Yarach et al., 2015).

There are two main categories of motion correction methods: Prospective Motion Correction (PMC) and Retrospective Motion Correction (RMC). In PMC, real-time motion information of the participant's head is obtained concurrently with the acquisition of the imaging volume. This information is used to update the co-ordinates of the acquisition volume before each radiofrequency (RF) pulse to ensure that the exact same voxels are being acquired across time. Recent reviews (Maclaren et al., 2013; Zaitsev et al., 2016) provide a good overview of the PMC field. I discussed the various methods of implementing PMC and demonstrated the effectiveness of PMC using the Kineticor optical tracking system in Chapter 3. PMC has some notable advantages, such as being able to ensure that edge voxels are consistently captured in cases of partial brain volume acquisition and ability to correct for intra-volume motion. However, PMC is still a relatively novel field and specialized equipment (such as an in-bore optical camera, dentist-moulded mouthpieces for marker attachment, etc) is often not widely available. Moreover, implementation of PMC requires additional modifications to standard scanning sequences.

In contrast, RMC has consistently been part of post-processing pipelines for over 15 years and has been streamlined into most post-processing pipelines, such as that in the SPM software (www.fil.ion.ucl.ac.uk/spm). Most implementations of RMC also do not require additional acquisitions or alterations to the scan sequence. Currently, most RMC methods utilize a cost function relying on intensity differences per voxel across the volumes to drive realignment, henceforth referred to as Voxel-Based Registration (VBR) methods. There have also been attempts to address the non-rigid body nature of motion artefacts through more advanced realignment methods (Andersson et al., 2001; Chambers et al., 2015).

In this chapter, I propose a novel application of Boundary-Based Registration (BBR) to generate an accurate realignment of an fMRI time series to improve on conventional RMC techniques. BBR (Greve and Fischl, 2009) was originally developed to coregister images across different imaging modalities or functional contrasts, and has been shown to be more effective than standard VBR methods. However, to the best of my knowledge, BBR has not been used to realign time series data. I utilized the Freesurfer implementation of BBR in my realignment pipeline by coregistering each fMRI volume to the same structural volume, thereby aligning each fMRI volume to every other fMRI volume in the process. I evaluated the performance of BBR realignment against a standard VBR approach, in this case SPM's conventional fMRI realignment, which has been used for high-resolution 7T data (O'Brien et al., 2017; Tak et al., 2018).

In BBR, the grey matter boundaries (taken from a cortical surface reconstruction using the structural data) are used to align the EPI image such that the maximum change of intensity in the EPI image is perpendicular to that of the boundary. By repeating this procedure for each fMRI volume, this realigns the fMRI volumes to each other and to the structural at the same time. For VBR, the fMRI volumes are directly aligned to each other (without using a structural image), and importantly, the cost function is based instead on the sum of squared differences in intensity values across all voxels within a pair of fMRI volumes. I hypothesise that the fact that the BBR cost function depends only on grey-matter boundaries would benefit alignment of 7T sub-millimetre data, since it would be more robust to distortions introduced by signal inhomogeneities at medial white-matter and subcortical locations.

The 7T data from Chapter 5 will be utilised for this chapter and analysed using the two different realignment methods (BBR vs SPM's VBR). I looked at four different metrics of data quality: three univariate metrics – temporal signal to noise ratio (tSNR), functional contrast to noise ratio (fCNR) and the coefficient of determination for the model fit (R2) – and the cross-validated linear discriminant contrast (LDC) as a multivariate metric (Huang et al., 2018). The stimuli were designed to probe multiple regions of interest (ROIs), in both early and higher visual areas, so as to allow for comparison of the realignment methods for different brain regions. I will also carry out three additional realignment approaches that are intermediary between the two main methods to attempt to isolate the source of any differences between the two realignment methods. These intermediary methods utilize 1) a brain mask for SPM realignment (reducing the influence of non-brain voxels on the realignment), 2) a reduced brain mask for SPM realignment and 3) realignment via coregistering each fMRI volume to the structural image, analogous to BBR, but using SPM's between-modality, voxel-based coregistration (where the cost function is based on mutual information rather than sum-of-squares). Finally, I also apply the BBR realignment technique to 3T data (whose acquisition is described

in Chapter 3) in an attempt to establish whether any differences or improvements are restricted to high-field 7T data, or generalizable to other type of fMRI data.

6.3 Methods

6.3.1 7T Experiment

For the 7T experiment, I utilized the data from the 7T experiment described in Chapter 5. I chose to focus my analysis on the runs of task type TaskD- because I expect that to have the largest contrast between conditions, and hence be more sensitive to any changes in data quality due to the varying realignment methods. Briefly, I examined six participants, each of whom underwent four runs of task type TaskD-. Within each run, there were 4 types of stimuli conditions, where participants were required to attend to varying stimuli category (faces vs houses) and location (along either diagonals). This allowed me to probe the effectiveness of the different realignment methods across both retinotopic (using location selectivity) and categorical (using categorical selectivity) ROIs.

6.3.2 3T Experiment

For the 3T experiment, I utilized the data from the PMC experiment described in Chapter 3. I chose to utilize the data from the PMC experiment instead of the latter visual experiment because of the larger sample size (18 participants) in the PMC experiment. This would increase the power and sensitivity of the analyses. Moreover, the PMC data was acquired at 2 resolutions and thus, can potentially allow me to differentiate between the effect of scanners and resolutions. Briefly, the participants attended to black and white gratings presented in an annulus, with varying orientation.

6.3.3 Realignment Methods

After initial post-processing (slice time correction for both 3T and 7T and TOPUP for 7T, described in Section 1.5.2), the fMRI volumes underwent five different realignment methods— two main methods and three subsidiary methods. Note that for all realignment methods, the volumes were only repositioned using their individual methods. All realignment methods utilizes the SPM reslice function to resample the voxels into the same space, hence removing any confounds that could arise due to different interpolation methods.

Main Realignment Methods

The two main methods were functional-structural BBR realignment and functional-functional VBR realignment in SPM 12. For functional-structural BBR realignment, I applied the Freesurfer 6.0.0

implementation of the BBR function in a two-step process. First, all of the fMRI images were averaged across volumes to generate the mean fMRI image, which was aligned to the structural using BBR to generate an initial realignment matrix. Next, each fMRI volume was aligned to the structural using BBR with the initial realignment matrix as the seed. Utilizing the mean image realignment as the initial seed would help to reduce computation time and minimize the probability of convergence failures due to local minima. This operation combined the motion correction of functional images with the coregistration to the structural image in one processing step.

For functional-functional VBR realignment, I used standard rigid-body realignment based on a sum-of-squares cost function as implemented in SPM12, which I refer to as the functional-functional VBR approach subsequently. Previous studies (Morgan et al., 2007; Oakes et al., 2005) have shown that while there are subtle differences between the various software packages (SPM, Analysis of Functional Neuroimages (AFNI), BrainVoyager and FMRIB Software Library (FSL)), the quality of the realignment showed similar performances across all packages. To minimize resampling of the functional data, the structural was then coregistered to the functional data using BBR, analogous to the functional-structural BBR method above. The same transformation was applied on the ROIs mentioned in Section 3cii to map them into functional space. However, note that in this case, the ROIs and structural data were transformed into functional space for coregistration so as to ensure that the fMRI data was only resampled once, similar to the functional-structural BBR realignment approach. In contrast, the functional-structural realignment procedure transforms and coregisters the functional data to the structural data in the structural space in a single resampling step.

Subsidiary Realignment Methods

In order to probe the cause of the differences between the two main realignment methods, I evaluated three additional realignment methods. Firstly, I repeated the functional-functional VBR realignment, while restricting the motion estimation to a full brain mask (both shaded area in Figure 6-1) or a small brain mask (red area in Figure 6-1). These methods are referred to as functional-functional VBR realignment with full brain mask and functional-function VBR realignment with small brain mask, respectively. Lastly, I realigned every fMRI volume at each timepoint to the structural using the SPM's between-modality coregistration function with a Normalized Mutual Information (NMI) cost function (functional-structural VBR). By doing so, I repeated the BBR realignment procedure, except that SPM's coregistration function replaced the BBR coregistration.

The two functional-functional VBR realignments with brain masks served to remove the potential confound of non-brain voxels negatively affecting the standard SPM realignment. Note that since BBR

realignment is driven solely by boundaries, the method is already robust against the majority of the intensity changes in out-of-brain voxels. The definition of both masks is discussed in the net section. A smaller brain mask (in which more voxels outside the brain surface were removed) was also utilized because preliminary analysis at some 7T sites have shown that this method results in better realignment. These two methods would help determine if the improvements seen in BBR realignment were due to ignoring out-of-brain voxels. Concurrently, comparisons using the functional-structural VBR realignment isolated whether differences between the two main methods were due to a methodological difference (realigning within a time series vs realigning via a structural template) or whether the benefit was inherent to the different cost functions used.

6.3.4 Brain Masks

The full brain mask was obtained by combining the grey matter and white matter voxels from the Freesurfer reconstruction and then coregistered to the functional volumes using BBR. Next, the full brain mask underwent dilation of two voxels and subsequent erosion by two voxels to fill in the sulci voxels and ensure a continuous brain mask. The small brain mask was obtained by eroding the full brain mask by 10 voxels. A sample volume of both brain masks superimposed on the mean fMRI image is shown in Figure 6-1.

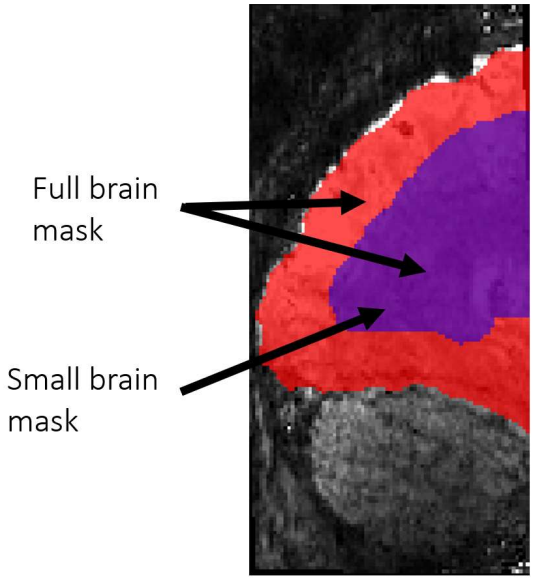

Figure 6-1: An illustration of the two brain masks utilized for the subsidiary realignment methods. The full brain mask consists of both the red and purple areas while the small brain mask consists of only the purple area.

I also created a grey matter mask solely for tSNR analysis. This was obtained by combining all the grey matter voxels from the Freesurfer reconstruction and coregistering it to the functional volume using

BBR. Note that coregistration to the functional volume is not required for applying the masks to datasets realigned using BBR realignment.

2020

6.3.5 Data Analysis

I analysed the processed data using the following four metrics— tSNR, fCNR, R2 and LDC. The implementation of these metrics was described in Section 2.4. Note that due to the small sample size for 7T (six participants), my results will only be significant under Wilcoxon signed rank test (p=0.0313) if all six participants demonstrate changes in the same direction. In all other cases, the results would not be significant (p>0.0625). This restriction does not apply to the 3T data.

6.4 Results (Two main realignment methods)

6.4.1 tSNR analysis of 7T fMRI data

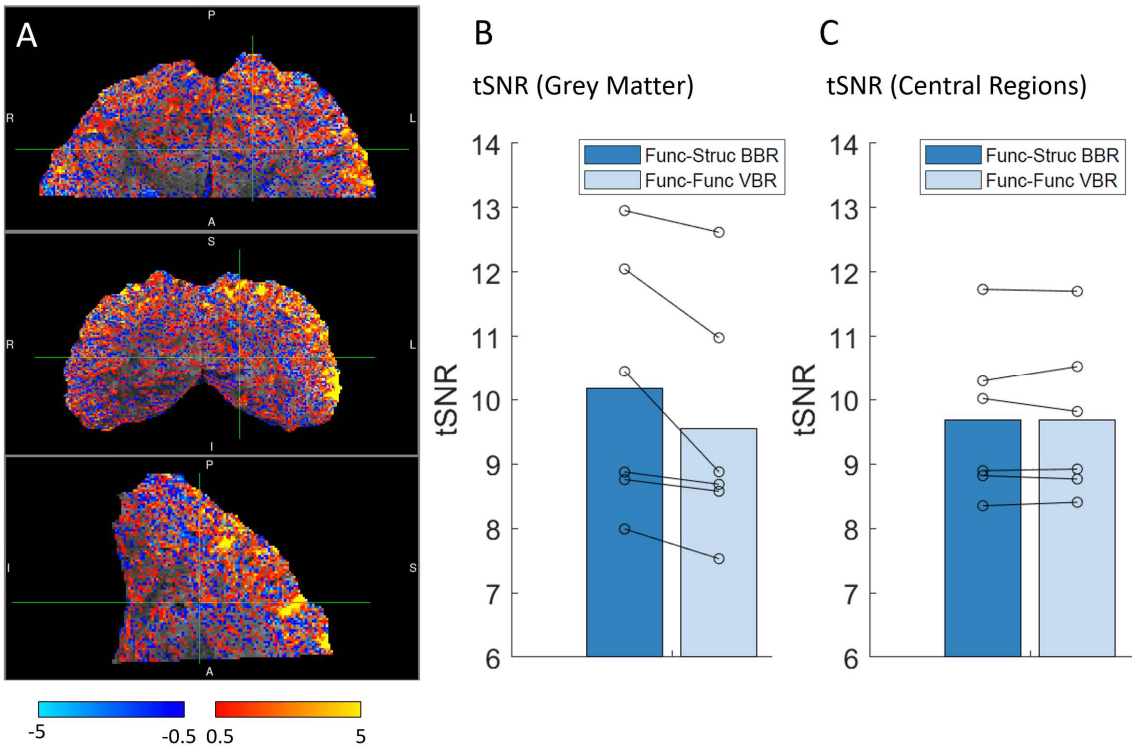

Figure 6-2: Panel A shows a comparison of the tSNR of the two main methods using a sample participant. The heatmap is generated by subtracting the functional-functional VBR tSNR from the functional-structural BBR tSNR. Red-yellow areas indicate regions where functional-structural BBR performs better while blue-teal areas show regions where functional-functional VBR performs better. Panel B shows the tSNR of the grey matter across all 6 participants when the two main realignment methods were used. Panel C shows the tSNR of the two main

realignment methods when the small brain mask (Figure 1) is applied. For both Panel B and C, each pair of connected circles indicate single participant results while the bar shows the group average.

I analysed the tSNR of the resultant data when the two main realignment methods were applied (see Figure 6-2, Panel A for a comparison map between the two methods on a sample participant). Improvements due to BBR realignment are heavily localized on the brain surface, in agreement with my expectations since BBR is boundary driven. In the central regions of the brain, there is no visually discernible advantage of either method and voxels showing improvements due to either method were most likely reflecting random fluctuations in the data. When the tSNR was averaged over all grey-matter voxels, I found that BBR significantly outperforms VBR under the Wilcoxon signed-rank test (Figure 6-2, Panel B). In contrast, when the tSNR was averaged over the central (mostly white matter) brain regions using the small brain mask, both methods yielded very similar results (mean=9.69 for both, Figure 6-2, Panel C). These results are consistent with the visual interpretation of the heatmap in Figure 6-2 and with my expectations that the benefit of BBR would be more localized towards boundaries.

6.4.2 fCNR analysis of 7T fMRI data

Analysis of the fCNR in the visual ROIs provided further evidence that BBR realignment outperforms the standard VBR approach (Figure 6-3, Panel A). When I averaged the fCNR across all ROIs within each participant, the Wilcoxon signed-rank test indicated that BBR realignment significantly benefits my data relative to VBR realignment. For individual ROIs, only V1 and V2 showed significant benefits of BBR realignment under Wilcoxon signed-rank testing. All other ROIs had a general trend of BBR realignment being better than standard VBR realignment, although this improvement is not consistent across all participants.

6.4.3 R2 analysis of 7T fMRI data

The results of the R2 analysis (Figure 6-3, Panel B) showed similar results to the fCNR analysis, which is expected since these two metrics are closely related. After I averaged the R2 results across all ROIs within each participant, BBR realignment significantly outperformed VBR realignment under the Wilcoxon signed-rank test. Individual ROI results showed significant differences for V1, V3 and TOS, while all other ROIs showed a small, but non-significant, benefit of BBR realignment over standard VBR realignment.

6.4.4 LDC analysis of 7T fMRI data

Similar to R2 and fCNR results, the average LDC across all ROIs showed a significant improvement for BBR realignment under Wilcoxon signed-rank test (Figure 6-3). Furthermore, for all individual ROIs,

the LDC from the BBR realignment data was significantly higher than that of VBR realignment data under Wilcoxon signed-rank test. These results suggest that there is a consistent benefit of BBR realignment across all ROIs.

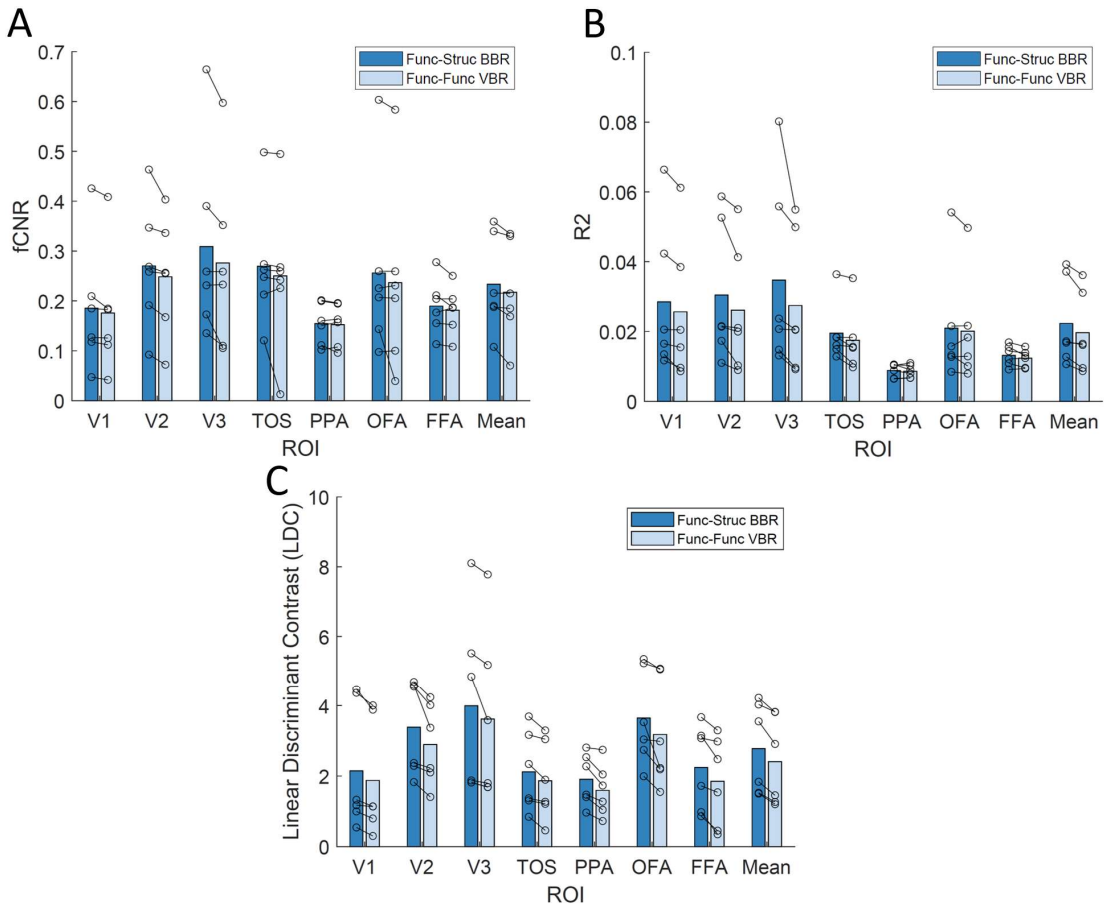

Figure 6-3: These plots compare functional-structural BBR against functional-functional VBR across multiple metrics— fCNR (Panel A), R2 (Panel B) and Linear Discriminant Contrast (Panel C). The mean plots indicate average pver Each pair of connected circles indicate single participant results while the bar shows the group average.

6.4.5 tSNR analysis of 3T fMRI data

When the main realignment methods were applied to the 3T data, I obtained substantially different results (Figure 6-4). At 1.5mm (Panel A), both methods showed very similar tSNR results across all three sessions and no significant differences were observed when the Wilcoxon signed rank test was carried out (p=0.47). At 3mm (Panel B) BBR realignment performed significantly worse than standard
2080 VBR realignment for all 3 sessions (p = 0.00049 under Wilcoxon signed rank test). These findings applied regardless of whether PMC was applied to the data or not; for further elaborations on the

three cases, see Chapter 3. These results indicate that there was no benefit to using BBR realignment for 3T data and that it could even be detrimental (in the case of 3mm isotropic fMRI data). Given that I did not observe any benefit of BBR realignment at the level of tSNR, I did not carry out further analysis with other metrics or subsidiary methods. Moreover, due to the difference in the nature of the two tasks, I would be unable to draw any conclusions from comparing between the 3T and 7T data for fCNR, R2 and LDC.

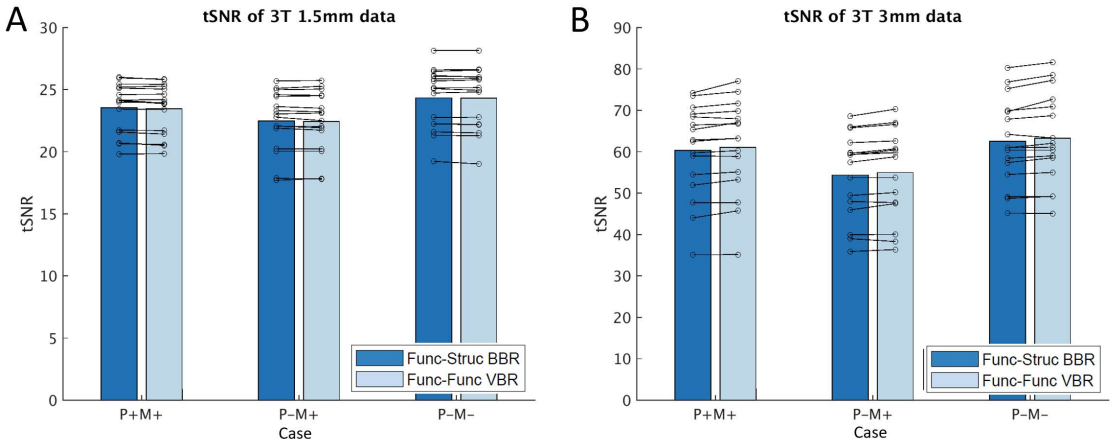

Figure 6-4: These plots compare the tSNR of functional-structural BBR against functional-functional VBR for 3T data at 1.5mm isotropic resolution (Panel A) and 3mm isotropic resolution (Panel B). The three cases on the x-axis corresponds to the type of PMC used- PMC On, Mouthpiece On (P+M+); PMC Off, Mouthpiece On (P-M+); PMC Off, Mouthpiece Off(P-M-). The fourth condition (PMC On, Mouthpiece Off) was not carried out because PMC was unreliable in the absence of the mouthpiece. Each pair of connected circles indicate single participant results while the bar shows the group average.

6.5 Results (Subsidiary methods)

To attempt to resolve the source of the difference between the VBR and BBR realignment results, I designed three subsidiary analyses to bridge the gap between the two main analyses. These analyses were not included in the main analysis section as they are not standalone methods of improving fMRI realignment, but rather additional analyses to help determine the cause of the differences between the functional-functional VBR and functional-structural BBR results. The three methods were: functional-functional VBR realignment with a full brain mask, functional-functional VBR realignment with a smaller brain mask and functional-structural VBR realignment. These analysis methods were discussed in detail in Section 6.3.3.

6.5.1 tSNR analysis of 7T fMRI data

The tSNR results of the three subsidiary methods were plotted together with the two main methods in Figure 6-5, Panel A. The functional-structural BBR realignment (leftmost bar) was significantly better than the other four methods. The results from the functional-functional VBR realignment using SPM with the two masks (full brain and smaller brain, middle and second bar from the right) were very similar to that of the standard VBR realignment results with no mask applied (second bar from the left). This was confirmed by the Wilcoxon signed-rank test showing no significant difference between the VBR realignment with and without mask in SPM, indicating that there is no significant benefit of removing non-brain voxels.

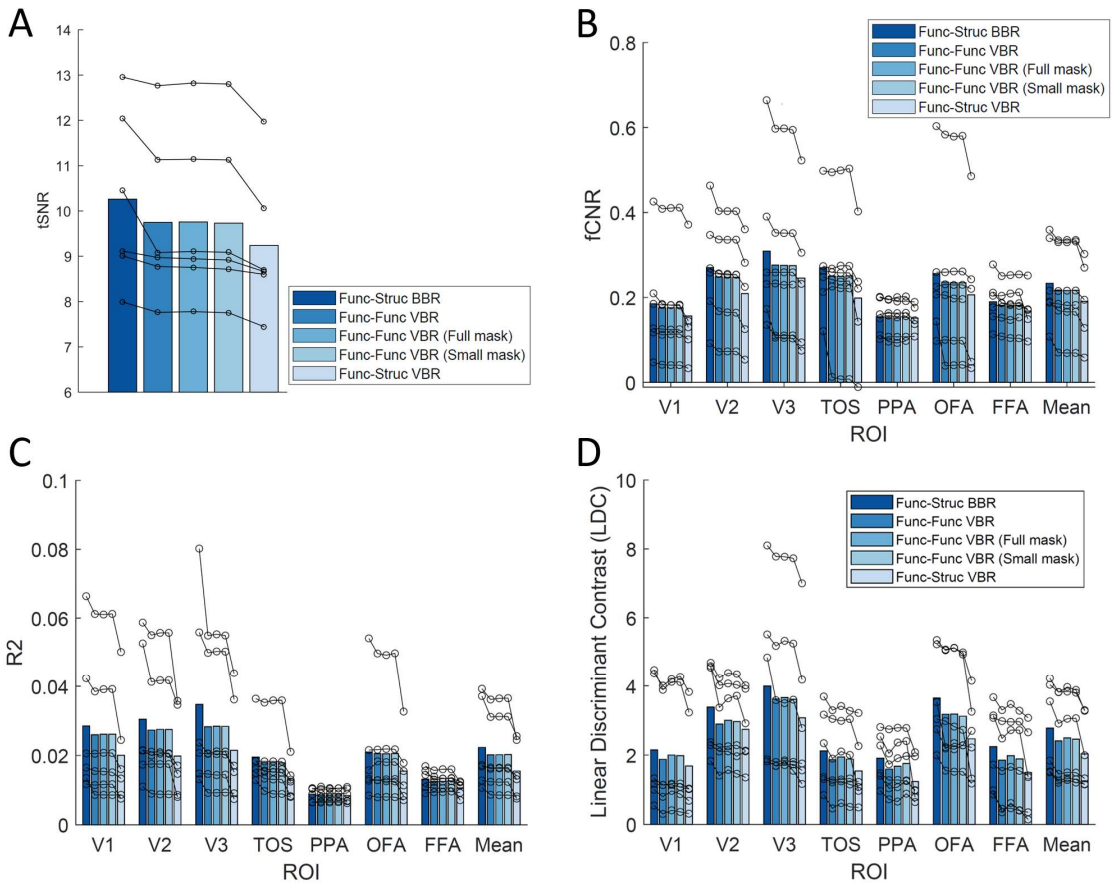

Figure 6-5: These plots compare the five different realignment methods across multiple metrics- tSNR (Panel A), fCNR (Panel B), R2 (Panel C) and Linear Discriminant Contrast (Panel D). Each set of connected circles indicate single participant results while the bar shows the group average.

When the data was realigned using the functional-structural VBR realignment process (rightmost bar) is used, the tSNR results were significantly worse than both the functional-structural BBR realignment and the functional-functional VBR realignment results. This result showed that using VBR realignment

to the structural is worse than standard VBR realignment and that the benefit of BBR realignment did not arise from the functional-structural nature of the realignment process, but rather an inherent benefit of the BBR cost function, which emphasizes accurate registration of cortical boundaries.

6.5.2 fCNR and R2 analysis of 7T fMRI data

Subsidiary analyses on the fCNR and R2 metrics echoed my findings from the tSNR results (Figure 6-5, Panels B and C). When either brain masks were utilized for functional-functional VBR realignment (middle and second bar from the right), the results were similar to that of VBR realignment without any mask (second bar from the left). No significant difference was detected across all ROIs between the three functional-functional VBR methods via pairwise comparison using Wilcoxon signed-rank test for both fCNR and R2. Moreover, comparisons between the results from BBR realignment (leftmost bar) and the two functional-functional VBR realignments with either mask were similar to the comparison between the two main methods, with significant improvements in the early visual areas but no significant difference in the higher visual areas.

Similar to the tSNR results, functional-structural VBR realignment (rightmost bar) produced results that were significantly worse than all other realignment techniques for both R2 and fCNR analysis. This result further affirmed that there is no benefit inherent to a functional-structural realignment, and that the benefit of the BBR realignment is intrinsic to the cost function. Overall, my fCNR and R2 analysis results are in agreement with the tSNR results that BBR realignment is the best realignment method of all five used, and that masking generates little to no benefit for conventional SPM realignment.

6.5.3 LDC analysis of 7T fMRI data

Subsidiary analysis using the multivariate LDC measure (Figure 6-5, Panel D) shows that utilizing a mask (middle and second bar from the right) improves the quality of the data slightly when functional-functional VBR was carried out relative to the no mask case (second bar from the left). This improvement is consistent, but not significant, across all ROIs except OFA. The effect of masking also does not fully account for the differences between the main BBR and VBR realignment methods as BBR realignment still outperforms all VBR realignments, with or without masks. Similar to the other analyses, functional-structural VBR realignment (rightmost bar) produced results significantly worse than all other methods across all ROIs.

6.6 Discussion

RMC is a critical step for ensuring data quality. While I have demonstrated in Chapter 3 that PMC is more successful at correcting motion than RMC, the usage of one does not necessarily preclude the other. As seen from the residual motion charts (Figure 3-6) from PMC, PMC is unable to fully correct for all motion, and thus it is highly probable that a combination of PMC and RMC would generate the optimal correction. In this chapter, I show that BBR realignment outperforms more conventional VBR realignment techniques for realigning 7T submillimetre data. Given the increasing interest in localizing differences in functional activations across different cortical layers and columns and probing fine-scale functional specialization, it is important to ensure proper data realignment to prevent the masking of real effects or being misled by false positives (Yakupov et al., 2017).

Initial comparisons of realigning 7T submillimetre data using the two main methods (BBR realignment and standard whole-image VBR) showed a benefit of using BBR realignment and this benefit was observed across all four metrics used, tSNR, fCNR, R2 and LDC. All benefits were shown to be significant according to Wilcoxon signed-rank testing when averaged across all ROIs. When I looked at individual ROIs using fCNR and R2 analysis, I noted the greatest numerical improvements in ROIs near the surface of the brain, namely the early visual areas. Most of these areas also showed a significant improvement under Wilcoxon's signed-rank test. This is in agreement with the tSNR comparison heatmap, which showed the greatest benefit of BBR realignment being in the proximity of the brain surface. Moreover, when I restricted my analysis to the central regions of the brain, both methods yielded similar tSNR results. This is in line with my expectations since BBR is driven by realigning the boundaries of the brain and hence, the largest benefit should be observed on and around the boundaries. However, in the LDC analysis, all ROIs showed significant improvements when BBR realignment is utilized. Since I expect LDC to be more sensitive than the univariate metrics, these results suggest that while the major benefits of BBR realignment were localized to the brain's surface, there were also more subtle improvements in the deeper brain regions.

Evaluating the effectiveness of the two main realignment methods on 3T data showed no difference between realignment methods for 1.5mm isotropic data and a significant decrease in tSNR for BBR realignment for 3mm isotropic data. This agrees with my expectations that BBR realignment should be most beneficial at higher resolutions since BBR requires clearly defined boundaries to drive the realignment. At lower resolutions (especially 3mm isotropic voxels), there is a lack of fine structural detail to inform the realignment and thus, could result in inaccurate realignment by the BBR algorithm. There are also more severe geometric distortions at 7T due to field inhomogeneities. This could partly explain why BBR was more beneficial at 7T relative to 3T.

To further query the source of the benefit for BBR realignment, I carried out three subsidiary realignment methods. Functional-functional VBR realignment with a full brain mask or a smaller brain mask showed similar results to standard VBR realignment without a mask under univariate analysis. When LDC was carried out, functional-functional VBR realignment showed a slight benefit of masking over the standard VBR realignment without masking, but the results were still significantly worse than functional-structural BBR realignment. Taken together, these results show that masking out non-brain voxels slightly benefits VBR realignment, and this benefit is only observable under more sensitive multivariate analysis. This benefit is also minor and not sufficient to explain the discrepancy between VBR realignment and BBR realignment, suggesting that the advantage of BBR realignment does not simply reflect the smaller subset of brain voxels used but rather reflects an inherent improvement due to the BBR cost function used.

Functional-structural VBR generated much poorer realignment of data as compared to the other four methods. This is reflected by a significant decrease in tSNR and significantly worse fCNR, R2 and LDC values across most ROIs. This is in line with my expectations since the SPM coregistration function is not designed for the purposes of time series realignment. Nonetheless, these results confirm that the advantage of BBR realignment is inherent to the BBR cost function and not an artefact arising from realigning to the structural instead of between functional volumes.

Given that functional-structural VBR realignment was the worst performing realignment method, it is worth considering if functional-functional BBR realignment is possible. This would allow me to utilize the benefit of the BBR cost function, while potentially removing the drawbacks of a functional-structural coregistration across modalities (e.g. different spatial distortions in functional and structural volumes). However, BBR requires one image to have a clear definition of the grey matter boundaries (normally the higher-resolution structural image) and I believe that the fMRI volumes do not typically have sufficient contrast to define these boundaries to drive BBR. Moreover, in the Freesurfer implementation of BBR, a surface reconstruction is needed to generate the boundary definition, which requires a structural image or an image with structural-like contrast. However, there is potential to address these distortion issues through newer sequences such as multi-inversion-recovery time echo planar imaging (MI-EPI) (Kashyap et al., 2018). MI-EPI generates an image with structural-like contrast, but is distortion matched to standard EPI sequences. Thus, this could be helpful in addressing some of the issues with functional-structural BBR realignment.

In this chapter, I showed that BBR realignment is beneficial for 7T submillimetre data, especially if the regions of interest is near the surface of the brain. I also demonstrated that the benefits of BBR realignment is inherent to that of the BBR cost functional and not due to other methodological

differences. However, there are a few limitations to this study. Firstly, I used a relatively unconventional FOV due to the need to capture both higher and early visual areas with minimal TR. Future studies using different FOVs could help further establish the advantages of using BBR realignment. Secondly, BBR realignment does not, on its own, deal with other artefacts caused by head motion, such as within-volume motion and interactions with field inhomogeneities, which cause non-rigid deformations of the image. Thus, BBR realignment could be further complimented by other motion correction techniques, such as slice-based PMC (Chapter 3, Huang et al., 2018; Schulz et al., 2014) and higher order corrections for field inhomogeneities (Andersson et al., 2003; Chambers et al., 2015; Yarach et al., 2015).

6.7 Conclusion

As the field shifts towards higher resolutions and smaller voxels, participant motion during fMRI will remain an important and pertinent problem. In this chapter, I presented results that show BBR realignment of fMRI volumes helps to remove inter-volume motion for fMRI time sequences and thereby improves the quality of the data, as measured by four different metrics (tSNR, fCNR, R2 and LDC). I believe that this, together with other motion correction tools, will be critical as fMRI acquisitions move towards higher resolutions.

7 Cleaning Up 7T data for laminar analysis

7.1 Abstract

GE sequences have allowed researchers to acquire sub-millimetre resolution data using 7T with reasonable spatial coverage, TR and SNR, enabling researchers to probe the finer structures of the brain, such as cortical layers and columns, for functional and structural differences. However, the issue of superficial bias is an important confound that needs to be addressed prior to interpreting any differences across laminar layers. In this chapter, I presented a novel method of utilizing Deming regression, in conjunction with the exclusion of "venous" voxels, to address the issue. I demonstrated that the application of both methods on 7T fMRI data acquired with GE sequences was able to remove superficial bias and unmask the underlying flat laminar profile of attentional modulation. In addition, I also utilized a computational simulation to justify the usage of Deming regression over other normalization methods employed in the current literature.

7.2 Introduction

One of the major appeals of going to higher resolutions is the ability to discern differential activations across laminar layers. Previous neuroanatomical work (Markov et al., 2014; Rockland and Knutson, 2000; Rockland and Virga, 1989) have shown that different laminar layers receive input from different sources. Bottom-up signals have been observed to be more localized towards the middle layers, while feedback connections are shown to project into both superficial and deep layers. As such, there is a growing interest in using high resolution 7T fMRI data to corroborate these neuroanatomical findings and discern between bottom-up and top-down effects. Previous 7T fMRI studies (Kok et al., 2016; Lawrence et al., 2019; Muckli et al., 2015; Polimeni et al., 2010) have suggested that such top-down modulation differentiate between laminar layers, but there is a disagreement to the exact laminar layers where the feedback information is projected to. Kok et al., 2016 utilized the Kaniza triangle illusion and observed strongest feedback effects in the deep layers. In contrast, Muckli et al., 2015 used partially occluded images to demonstrate that above chance decoding of feedback information only occurred in superficial layers. Lastly, Lawrence et al., 2019 showed attention effects in all laminar layers, with slightly stronger effects in the superficial layers. These discrepancies across studies could reflect a dissociation between superficial and deep layers in terms of the type of feedback they receive, or could arise due to different methodologies resulting in different sensitivities and biases. This highlights the importance of ensuring data quality and removing biases in the data so allow researchers to reliably interpret the data.

Furthermore, there is also disagreement in the field as to the best method of acquiring data for laminar analysis. Gradient echo (GE) sequences (Yacoub et al., 2013) provide the strongest signal to noise ratio (SNR) but are also most susceptible to the effect of large draining veins on the cortical surface (Boxerman et al., 1995). This susceptibility to draining veins leads to lower specificity and a superficial bias in the raw data, which complicates the interpretation of raw estimates over layers. In contrast, spin echo (SE) and gradient and spin echo (GRASE) sequences (Feinberg et al., 2015) are primarily susceptible to capillaries, making them more specific and less prone to superficial bias. However, these sequences have much lower SNR, making it harder to distinguish the effects of interest and can potentially mask small activations. Moreover, SE and GRASE sequences are also more vulnerable to participant motion, especially between the RF pulses for each TR. Newer fMRI techniques have also emerged to study laminar effects, such as vascular space occupancy (VASO) (Huber et al., 2017b; Lu et al., 2013), measuring cerebral blood volume (CBV), or arterial spin labelling (ASL) (Huber et al., 2017b; Kashyap et al., 2019; Petcharunpaisan, 2010), measuring cerebral blood flow (CBF). While these methods are able to remove the spatial blurring due to draining veins, they come with their own host of problems, such as the largest CBV changes being localized in the arteries and potential dilation retrogradely in the upper layers relative to the location of neuronal activation (Uludağ and Blinder, 2018). Similar to GRASE, these methods also tend to have less sensitivity as a trade-off for their higher specificity (Huber et al., 2017b). Moreover, VASO and ASL generally have longer TRs than GE and are unable to utilize parallel imaging acceleration factors. Therefore, they are generally restricted to a much smaller field of view, approximately 30~50% of what is obtainable with GE (Huber et al., 2017a).

In this chapter, I attempted to demonstrate the ability to resolve laminar data using a GE sequence and applied two methods of correction to address the superficial bias. I chose to use a GE sequence because it is a straightforward sequence and offers the strongest SNR. Moreover, the larger FOV of GE sequences was needed to capture both early and higher visual areas for the neuroscience aspect of this study. There is also a physiological understanding of what drives superficial bias in GE sequences (Bianciardi et al., 2011; Fracasso et al., 2018; Kashyap et al., 2017), thus making it possible to address it directly in the post-processing stage. Previous studies using GE sequences have attempted to account for the superficial bias by different types of normalization— dividing by mean activation (Liu et al., 2019), z-scoring (Lawrence et al., 2019) or taking the ratio of two conditions (Kashyap et al., 2017). However, the validity of these corrections is unclear. Here, I employed a Deming regression and exclusion of "venous" voxels to address the superficial bias. I utilized a visual attention task (described in Section 2.1.2) to attempt to discern the laminar profile of feedback attention effects and to validate the effectiveness of the normalization employed. I also included a computational simulation to

demonstrate that Deming regression is more robust and accurate compared to the other methods of normalization.

7.3 Methods

7.3.1 Computational Simulation

I generated a computer simulation to compare the accuracy and precision of the different metrics of attention modulation. The script simulates the effects of attention on single neuron responses, and how such modulations manifest after pooling into coarse fMRI measurements. These fMRI measurements were then normalized across layers using four different metrics (raw ratio, Attention Modulation Index (AMI) and two metrics based on Deming regression). To validate the accuracy of the metrics, I tested how well each metric recovered the true underlying task-specific attention modulation.

I simulated a ROI with three layers, and 100 voxels per layer that has more face-responsive cells compared to house-responsive cells (e.g. FFA, OFA). Note that this simulation assumed nothing inherently specific to face- or house-responsive cells, and thus would also be applicable to retinotopic ROIs by simply treating the face- and house-responsive cells as being responsive to one of the two diagonals.

$$Voxel\ Response = L_{Bias} * (Response_{Face} * Att_{Face} * Salient_{Face} * Density_{Face} + Response_{House} * Att_{House} * Salient_{House} * Density_{House} + Noise_{Stim} + Noise_{General})$$

Equation 9: Expression for the calculation of each voxel's response to the various stimulus conditions.

First, I obtained the single cell response to each stimulus category by multiplying the task-specific attention modulation (Att_X) with the non-specific salient modulation ($Salient_X$). I assumed that if the participant is passively viewing the stimuli, the single cell response ($Response_X$) is one. I set the single cell response ($Response_X$) to zero if there was no stimulus from that category present. I then calculated each voxel's response by multiplying the density of the stimulus-responsive cells ($Density_X$) by the single cell response and combined the results for both stimulus categories. Next, I added both stimuli-specific noise ($Noise_{Stim}$) and shared noise ($Noise_{General}$, due to factors like poor-baseline estimate) to the voxel estimate. Lastly, I multiplied the voxel estimate by the superficial bias (L_{Bias}) to give us the stimulated response of a voxel to a specific stimulus representation.

This simulation made several simplifying assumptions, which I list here for clarity: neurons are purely responsive to faces or houses only; both saliency and attention modulate responsive cells only by

applying a gain factor; BOLD responses are simple sums over populations of face- and scene-cells; noise arises only at mapping from neural to BOLD signal; superficial bias can be modelled as a gain factor on responses, including the noise component. I did not account for thermal noise (i.e. noise independent of superficial bias), however I do not expect this to affect the comparisons since the impact of thermal noise on every metric should be similar.

I carried out these computations for all voxels in each layer of the ROI for the three task types (TaskD+, TaskD- and FixD-) and calculated the results obtained from the various metrics. Task type FixD- is nearly identical to task type TaskD-, with the exception that participants were instructed to fixate on the centre of the screen instead of attending to the prompted diagonals. I then attempted to use the individual metrics to recover the true underlying task specific attention modulation in the simulated
2340 neurons from the voxel responses. I iterated this simulation over various levels of noise, attention modulation and saliency, to check the impact of any of these parameters on the final estimate. For each individual set of parameters, I repeated the simulation 1000 times to obtain the mean and variance of the estimates.

Lastly, I chose the parameters to best resemble my 7T data by visually comparing the scatterplots of TaskD+ against TaskD- such that the simulated and actual data have similar distributions. Sample scatterplots from the simulation (Figure 7-1, Panel A) and 7T data (Figure 7-1, Panel B) are shown below. The parameters used were 2x noise, 0.5 proportion of shared noise and 1.5x salient modulation.

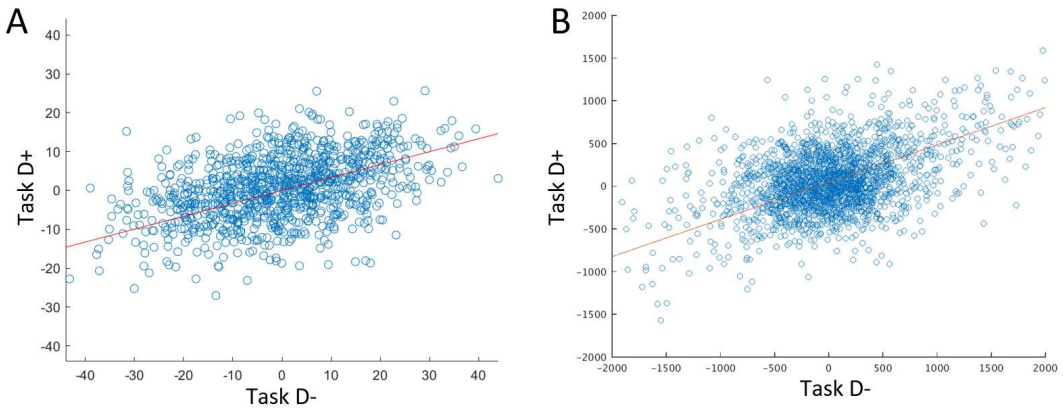

Figure 7-1: Scatterplots of the voxel responses to TaskD+ against TaskD- comparing my simulated data (Panel A) against the real 7T data (Panel B). Both scatterplots looks similar, suggesting that my simulation is capturing the behaviour of real voxels. The difference in scale does not matter since the absolute value of the selectivity response is inconsequential, I am only interested in the relation of the values across task types.

From the 7T data, I estimated that attention modulation in retinotopic areas can be approximated by a (neural) gain factor of 1.5 in retinotopic areas, and a factor of 3 in categorical areas. I used these estimates to simulate various conditions to compare the different metrics. First, I verified that my simulation was indeed able to reproduce the superficial bias observed in the data using a null case. I then tested the ability of the various metrics to recover the underlying attention modulation in a null case (constant attention modulation across layers) and my predicted laminar profile (stronger attention modulation in the superficial and deep layers).

7.3.2 Attention metrics for computational simulation

The four metrics compared in the simulation were described below:

Raw Ratio

The raw ratio utilizes the direct approach of calculating the raw ratio of TaskD+ contrast against TaskD- contrast for each voxel and averaging these ratios across the entire layer. I expect the mean ratio to be heavily influenced by voxels whose response in TaskD- is close to zero, rendering the ratio unstable. However, this method is included as a baseline metric.

Attention modulation Index (AMI) of Task D+

To calculate the AMI for each layer, I divided the TaskD+ contrast by the mean activation of the voxel in the TaskD+ condition. This metric has been employed in previous studies (Liu et al., 2019). Relative to the raw ratio and Deming Regressions, I expect the AMI of TaskD+ to be more sensitive to baseline inaccuracies and shared noise across responses.

Deming Regression of TaskD+/TaskD-

The Deming regression of TaskD+ against TaskD- accounts for errors in both x and y values and is also stable against values of TaskD- near zero. This method is further elaborated on in Section 7.3.7. I believe that the Deming regression of TaskD+/TaskD- will be the most accurate and stable measure of attention effects.

Deming Regression of TaskD-/FixD-

I also investigated the Deming regression of TaskD- against FixD-. I considered including this addition manipulation in my experimental design, but it was excluded on the basis of the results of this simulation. While the Deming regression of TaskD- against FixD- should exhibit similar stability as TaskD+ against TaskD-., it is susceptible to non-selective attention modulation (non-specific enhancement of responses due to e.g., increased arousal, task engagement, alertness), also referred

to as salient modulation. Thus, the Deming regression of TaskD- against FixD- may overestimate attention selectivity.

I did not include z-scoring method as the normalization employed in z-scoring does not allow me to recover the attention modulation and hence, unable to evaluate its precision. Moreover, as I did not simulate the timecourse, I do not have a measured noise estimate per voxel for z-scoring. However, I did attempt to utilize z-scoring on the real 7T data which was unsuccessful in eliminating the superficial bias (Figure 7-10).

7.3.3 Experimental Design

I utilized the 7T data acquired in Chapter 5. Here, I focused only on runs of task types TaskD+ and TaskD-. In both task types, participants were required to attend to the stimuli as prompted and make a same-difference judgement. Task type FixD+ was excluded as the stimuli were perfectly counterbalanced and there should be no consistent contrast between conditions (as seen in Figure 5-3). The runs with task type FixD- were also excluded due to the results of the simulation (presented below) showing that the Deming regression of TaskD- against FixD- would be susceptible to non-specific attention modulation to the task (referred to as salient modulation) and noisier than the Deming regression of TaskD+ against TaskD-. Moreover, TaskD- and FixD- were acquired on different sessions, and thus variations in external factors between sessions would also affect the results and disrupt the normalization.

Briefly, I examined six participants, each of whom underwent four runs of task type TaskD+ and four runs of task type TaskD-. Within each run, there were 4 types of stimuli conditions, where participants were required to attend to varying stimuli category (faces vs houses) and location (along either diagonal). For runs of task type TaskD+, distractors were present along the contrasting diagonal and selected from the contrasting category. Varying the attended category and location individually allowed me to probe for both spatial and categorical selectivity.

7.3.4 Cortical Depth Definition

The 3D GM-WM (Grey Matter-White Matter) and GM-CSF (Grey Matter- Cerebrospinal fluid) boundaries were obtained from the Freesurfer's reconstruction of each individual participant's cortices. These boundaries were visually inspected by overlaying them on the structural volume to ensure that the segmentation was accurate. In cases of poor segmentation, the realignment between the structural and the Freesurfer segmentation template was manually adjusted prior to repeating the Freesurfer reconstruction. The boundaries were exported to CBStools (Bazin et al., 2012) and used to generate four equivolume (Leprince et al., 2015) segmentations of the GM. Each GM voxel was then

assigned to one of the four layers using a winner-takes-all approach where the voxel was assigned to the layer with which it had the largest overlap with. An illustration of how this segmentation works was shown in Figure 7-2.

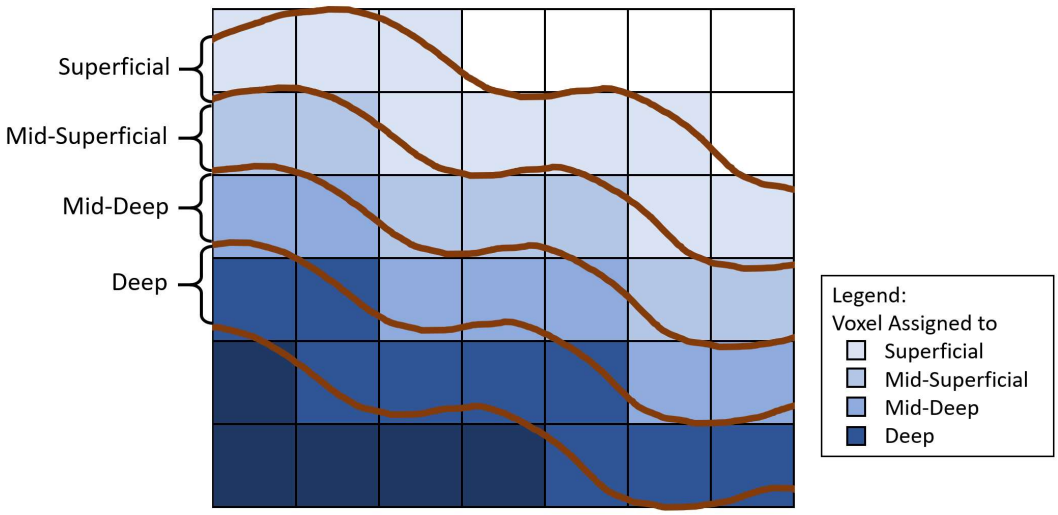

2420 *Figure 7-2: Illustration of how laminar segmentation is mapped onto the voxels. Upon generating the boundaries between the layers and superimposing it on the EPI volume, each voxel is assigned to the layer with which it has the greatest overlap with.*

7.3.5 Correcting for superficial bias

One of the concerns with laminar analysis using GE sequences is the presence of a superficial bias (Fracasso et al., 2018; Polimeni et al., 2010; Yacoub et al., 2013). This superficial bias is driven by two main contributory factors: a) the presence of draining veins in the brain structure causes deoxygenated blood from the deep layers to flow towards the superficial layers, resulting in an artificial increase in fMRI signal in the superficial layers that is not reflective of the underlying activation and b) variations in baseline CBV and relaxation parameters across different depths (Kashyap et al., 2017). To address the impact of draining veins, I attempted to exclude the voxels with high venous contributions. Next, for the variations in baseline parameters, I utilized a Deming regression approach.

7.3.6 Removing voxels with high venous contributions

Venous blood flow have been shown to lower the BOLD signal or even produce a negative BOLD signal in some cases (Bianciardi et al., 2011). Thus, I attempted to identify and isolate voxels with a high venous contribution using tSNR. I calculated the tSNR for each voxel and pooled them into two categories: “venous” voxels that predominantly contain veins (voxels with bottom 30% tSNR) and

"grey-matter" voxels that predominantly contain grey matter (remaining 70% of voxels). The 30% tSNR threshold was decided by visual inspection of the tSNR threshold map overlaid on the mean EPI and discussion with other 7T groups. While this threshold is arbitrary, the exact value of the threshold is of little consequence as using alternate thresholds(20%) yield comparable results (See Figure 7-8 and Supplementary Figure 7-1).

A sample overlay (Figure 7-3) of the "venous" voxels in V1 (left hemisphere) onto the mean EPI image shows strong clustering and a good overlap with the dark spots in the EPI, making a case that I am indeed excluding voxels with high venous contributions.

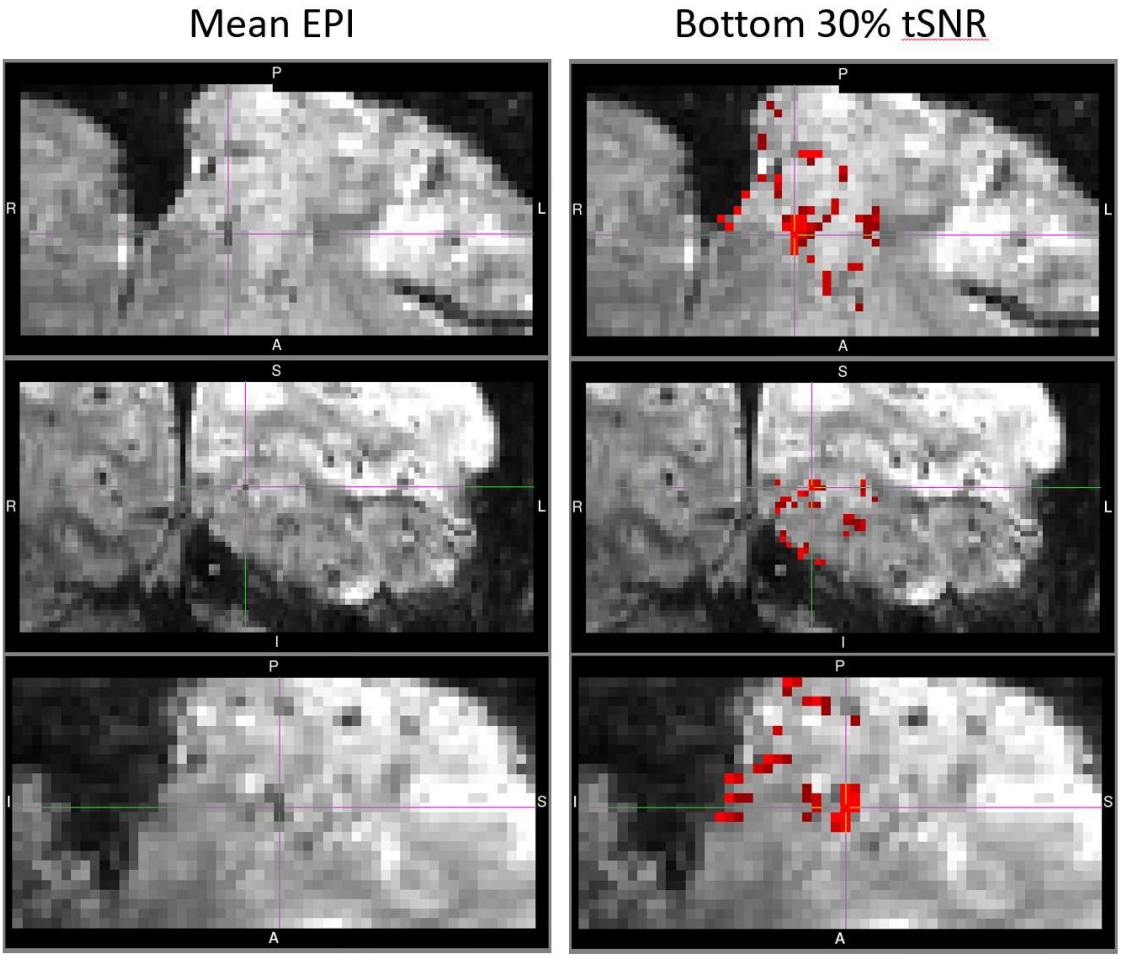

Figure 7-3: The mean EPI image and the mean EPI image overlaid with the bottom 30% tSNR voxels from the V1 (left hemisphere). The bottom 30% tSNR voxels show clustering and overlaps with dark spots on the mean EPI image, suggesting that these voxels indeed have a high veneous contribution.

7.3.7 Deming Regression

To remove the depth dependent profile due to variations in baseline parameters, I attempted a normalization approach using Deming regression. This was motivated by the assumption that the baseline parameters, such as the baseline blood volume, the baseline oxygen extraction fraction, have a purely multiplicative effect on BOLD sensitivity (Kashyap et al., 2017). Thus, I can formulate the BOLD signal change as $\delta S = L*R$, where L is a function of the baseline physiological parameters that influence the BOLD response and R is the actual change in CBV and concentration of deoxygenated haemoglobin as a response to brain function. I expect L to be constant within each cortical layer but varying across different cortical layers and R is my actual quantity of interest. Thus, by taking a ratio of the signal changes for two contrast estimates for each voxel:

$$\frac{\delta S_1}{\delta S_2} = \frac{L * R_1}{L * R_2} = \frac{R_1}{R_2}$$

Equation 10: By taking the ratio of 2 signal changes, I am able to remove the dependence on baseline physiological parameters.

I would be able to remove the dependence of the contrast on baseline parameters.

To obtain a single representative value for each layer, I chose to use Deming regression to obtain the ratio of $\delta S_1/\delta S_2$. This enabled me to compare across different laminar layers while adjusting for any superficial bias due to baseline parameters. Deming regression was chosen over ordinary least squares regression because it accounts for errors in both variables and hence is invariant to whether δS_1 or δS_2 is the regressor.

Deming regression was utilized over alternative normalization approaches (Kashyap et al., 2017; Lawrence et al., 2019; Liu et al., 2019) as my computer simulations below showed that Deming regression was more stable and precise relative to other metrics. As an added sanity check, I also generated scatterplots of δS_2 against δS_1 for each group of voxels and ensured that the voxels are reasonably clustered around the estimated best fit line. If different voxels were engaged by attention effects and stimuli effects, I would expect to see two or more distinct clusters and that would invalidate this approach.

7.3.8 Data analysis

Due to the higher noise levels of 7T and reduced voxel count due to partitioning into layers, there is much more noise and variation in the data during laminar analysis. Thus, I pooled the voxels across all ROIs according to their expected attention selectivity to increase my sensitivity to any variation in attention modulation across layers. More specifically, I pooled all the voxels from V1, V2 and V3 to

generate a spatially selective ROI and pooled all the voxels from TOS, PPA, OFA and FFA to generate a categorically selective ROI. I also looked at individual ROIs to ensure that the pooled ROIs are reflective of the constituent ROIs and that I am not discarding any between-ROI variations (Section 7.4.1).

I utilized spatial and categorical selectivity as my metric of interest. The definition of these metrics is described in depth in Section 5.3.3. Briefly, I contrasted the response from conditions attending to stimuli along one diagonal to the response from conditions attending to stimuli along other diagonal to obtain spatial selectivity. For categorical selectivity, I contrasted the response from conditions attending to stimuli from one category to the response from conditions when attending to stimuli from the other category. I also flipped the signs of the selectivity estimates to align with the region's expected preference.

7.4 Results

7.4.1 Computational simulations of various normalization methods

For my computational simulation, I first verified that the simulation was able to replicate the superficial bias observed in the 7T data. This was done by simulating a constant response across all layers and generating the simulated measured response. I verified that the superficial bias is indeed present in the measured response for attention modulation values of 1.5x (Figure 7-4, Panel A) and 3x (Figure 7-4, Panel B), which corresponds to the estimated attention modulation in retinotopic and categorical ROIs respectively.

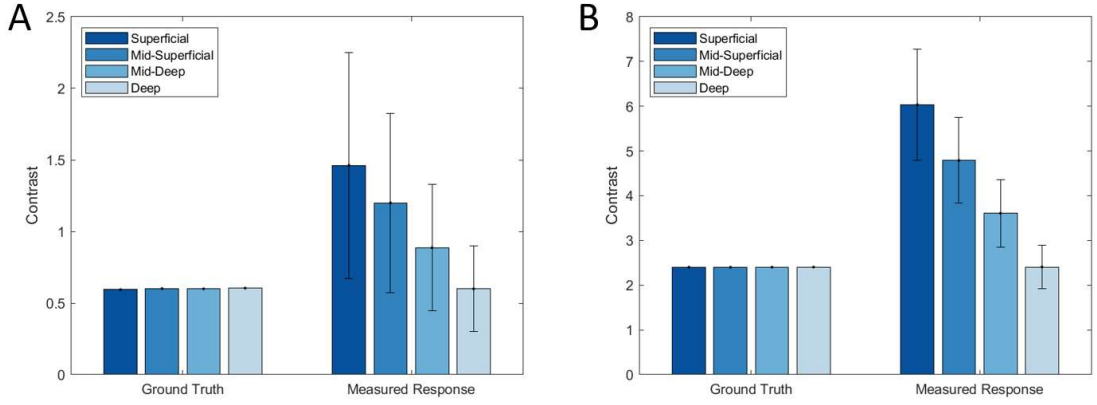

2500

Figure 7-4: Plots of the mean contrast between conditions for TaskD+. The ground truth reflects the value generated from my simulations in the absence of noise and superficial bias while the measured response corresponds to the expected measured values due to the presence of noise and superficial bias. This was repeated

for attention modulations of 1.5x (Panel A) and 3x (Panel B), corresponding to simulations of retinotopic and categorical ROIs respectively.

Next, I attempted to recover the true underlying attention modulation using the various metrics for the null case and investigated their stability and accuracy (Figure 7-5). Both the raw ratio of TaskD+/TaskD- and the AMI estimate are highly unstable and I was unable to obtain a stable estimate of the underlying attention modulation. Moreover, there was also no discernable trend across layers, and thus I was unable to verify if the method is able to remove the superficial bias. Both Deming regression methods were able to recover the flat profile across laminar layers, demonstrating that both methods indeed remove the superficial bias that arises due to variations in the baseline parameters. Deming regression of TaskD+/TaskD- was also able to recover the true underlying attention modulation accurately. However, the Deming regression of TaskD-/FixD- generated an inflated estimate of the true underlying attention modulation due to the presence of salient modulation. Moreover, the Deming regression of TaskD-/FixD- was also noisier than the Deming regression of TaskD+/TaskD-.

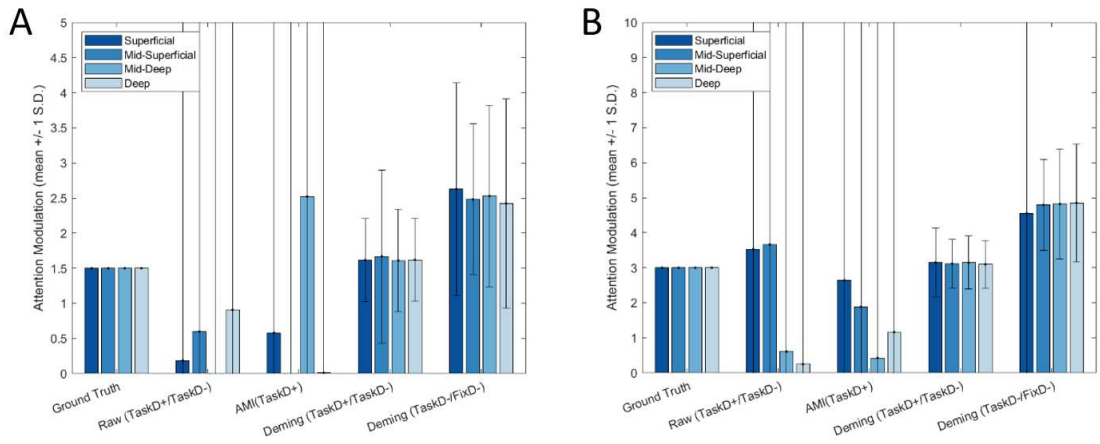

Figure 7-5: Plots of the attention modulation predicted by the various normalization metrics for the simulated retinotopic ROIs (Panel A) and categorical ROIs (Panel B) in a null case— constant attentional modulation across all layers. The ground truth reflects the actual attention modulation values used for the simulation. The graph scales were restricted between 0 to 5 and 0 to 10 respectively to prevent the instability of the metrics from distorting the graphs.

Lastly, I simulated an attention profile similar to what neuroanatomical studies suggest— stronger attention modulation in the superficial and deep laminar layers (Figure 7-6). Similar to the null case, the raw ratio and AMI metrics were extremely volatile and there did not seem to be any recoverable laminar profile across layers. Both metrics were also extremely noisy. The Deming regression of TaskD-

/FixD- was able to reproduce the same laminar trend as the underlying attention modulation. However, this estimate was inflated due to the presence of salient modulation, similar to the null case. Deming regression of TaskD+/TaskD- clearly outperformed all the other metrics and was able to recover the laminar profile with accurate estimates of the underlying attention modulation. Moreover, the Deming regression of TaskD+/TaskD- also had the least amount of noise among all metrics. Thus, this simulation motivated and justified the use of Deming regression of TaskD+/TaskD- as the metric of interest to test for laminar effects.

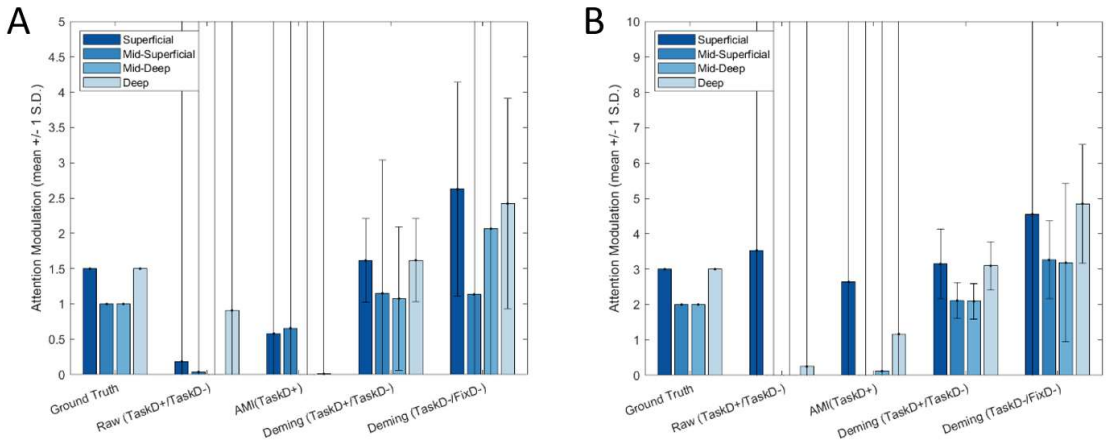

Figure 7-6: Plots of the attention modulation predicted by the various normalization metrics for the simulated retinotopic ROIs (Panel A) and categorical ROIs (Panel B) when feedback attention modulation was present—stronger attentional modulation in the superficial and deep layers. The ground truth reflects the actual attention modulation values used for the simulation. The graph scales were restricted between 0 to 5 and 0 to 10 respectively to prevent the instability of the metrics from distorting the graphs.

7.4.2 Laminar analysis of raw 7T selectivity responses

Laminar analysis on the 7T data prior to correcting for superficial bias showed strong selectivity responses in the superficial layers and a constant decrease towards deeper layers (Figure 7-7). This was consistent for both spatial and categorical selectivity, across all ROIs and both task types. OFA was the only exception, with a slightly weaker superficial response relative to the mid-superficial layer. This consistent superficial bias is in line with expectations from the current literature (Polimeni et al., 2010; Yacoub et al., 2013) due to the superficial bias of GE sequences.

For further laminar analysis, I pooled voxels from V1, V2 and V3 to form the spatially-selective ROI and voxels from TOS, PPA, OFA and FFA to form the categorically-selective ROI (Figure 7-7, rightmost bars). Comparing the behaviour of the individual ROIs and the pooled ROIs shows that the pooled ROI laminar profile is reflective of the individual ROIs that constitute it, justifying the pooling of ROIs.

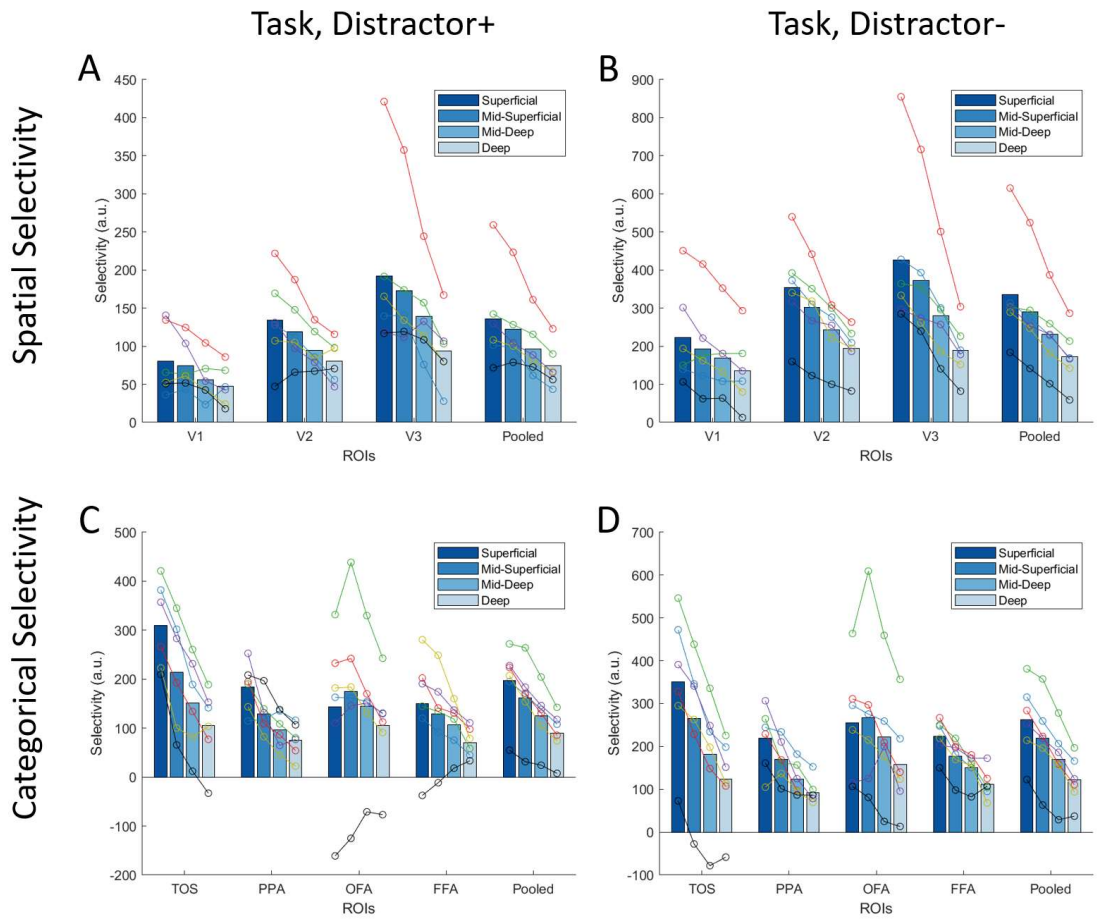

Figure 7-7: Plots of the selectivity estimates obtained at 7T across different layers for the two groups of pooled ROIs. Panels A and B show the laminar profile for location selectivity under the different task types: task with distractor (Panel A) and task without distractors (Panel B). Panels C and D show the laminar profile for category selectivity under the different task types: task with distractor (Panel C) and task without distractors (Panel D). The rightmost group illustrates the selectivity estimates when all the retinotopic or categorical ROIs are pooled. The bars represent the average of all six participants, with each pair of joint circles represent an individual subject. The same colour represents the same participant throughout all plots.

7.4.3 Laminar analysis of 7T using Deming regression

I applied two corrections to address the issue of superficial bias. Firstly, I separated the "venous" voxels (defined as the voxels with bottom 30% tSNR) from the remaining "grey-matter" voxels within each ROI prior to pooling. Note that the distribution of "venous" voxels was not uniform across layers, with a greater density of "venous" voxels in the superficial layers and a decreasing trend towards deeper layers. This is in line with neuroanatomical vasculature results (Adams et al., 2015) and other fMRI studies (Kay et al., 2019) which showed decreasing density of draining veins when moving from

superficial to deep layers. Secondly, I utilized a Deming regression of the two selectivity responses, TaskD+ against TaskD-, to remove the variations due to differences in baseline parameters.

Taking the Deming regression of TaskD+/TaskD- (Figure 7-8) shows a constant Deming slope estimate across all layers for the "grey-matter" voxels, suggesting that the superficial bias observed previously (Figure 7-7) is no longer present. The constant slope estimates suggest that attention modulation exerted proportionally similar effects across layers, after accounting for superficial bias. The estimates from the "venous" voxels show a similar trend but are notably more variable than the estimates from the "grey-matter" voxels, as expected from the lower tSNR.

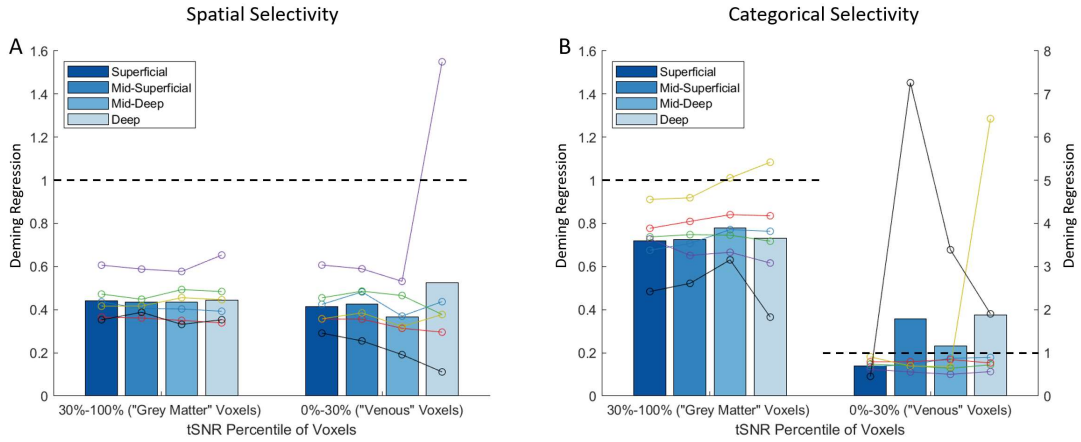

Figure 7-8: Plots of the location selectivity (Panel A) and category selectivity (Panel B) Deming regression of TaskD+/TaskD- obtained at 7T across different layers. Only the spatially-selective ROIs pool was used for the location selectivity plot and only the pooled category-selective ROIs were used for the category selectivity plot. The voxels were also divided into "grey matter" voxels and "venous" voxels by their tSNR. The dotted line represents a ratio of 1, which would be the expected ratio if no stimuli-driven effects were present. The bars represent the average of all six participants, with each pair of joint circles represent an individual subject. The same colour represents the same participant throughout all plots. Note that the "venous" voxels in Panel B has a different scale.

Looking at voxelwise scatterplots of TaskD+/TaskD- for a representative participant (Figure 7-9), I note that most voxels follow the best-fit line. This demonstrates that Deming regression is indeed detecting variations across the entire ROI and is not unduly influenced by outliers. The absence of individual clusters demonstrate that similar voxels are recruited for both attention modulation and stimuli representation effects, which validates the regression approach. Moreover, the high density of voxels close to the origin would produce highly unstable per-voxel ratio estimates, making a simple average of the per-voxel ratios unreliable. In contrast, the near-zero voxels have little influence on the slope estimate, and thus would not affect my Deming regression methodology.

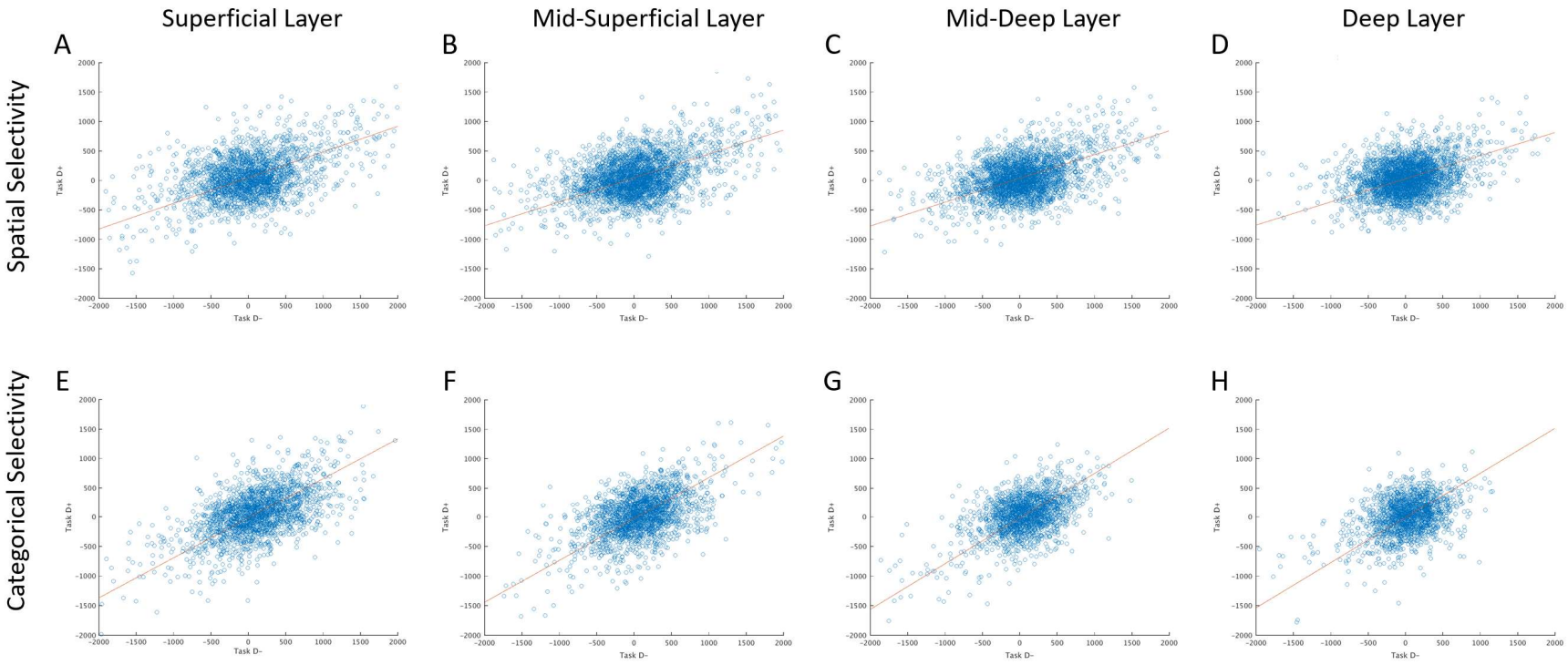

Figure 7-9: Scatterplots of the location selectivity (Panel A-D) and category selectivity (Panel E-H) contrast ratio of TaskD+/TaskD- obtained at 7T for the "grey matter" voxels across different layers for one participant. Only voxels from the spatially-selective ROIs was used for the location selectivity plot and only voxels from the category-selective ROIs were used for the category selectivity plot. The red line indicates the best fit line obtained by Deming regression which is then used to generate the slope estimate.

7.4.4 Laminar analysis of 7T data using alternative metrics

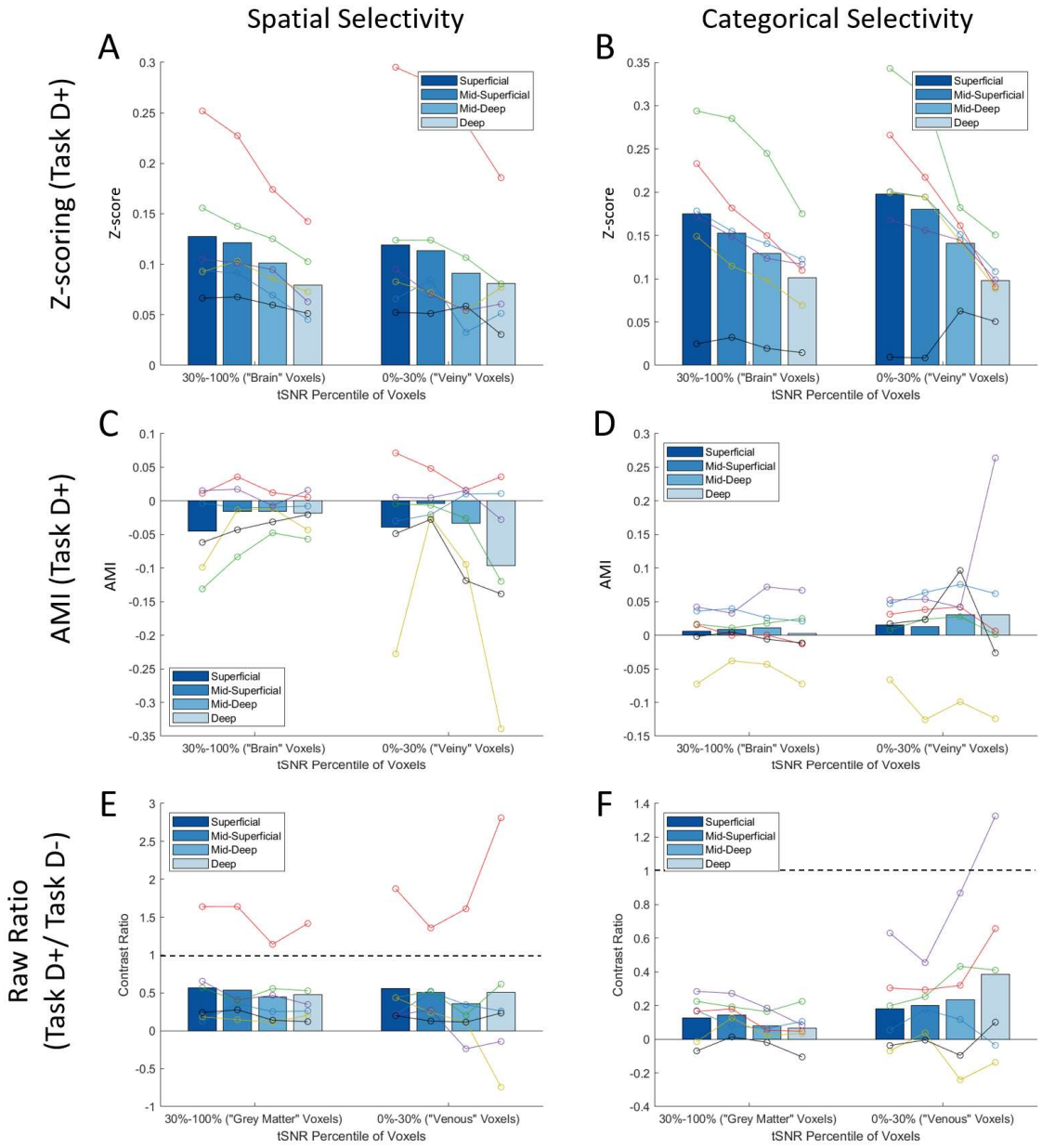

Figure 7-10: Plots of the estimates using the various alternative metrics on location selectivity (Panel A, C and E) and category selectivity (Panel B, D and F) at 7T across different layers. Only the spatially-selective ROIs pool was used for the location selectivity plot and only the pooled category-selective ROIs were used for the category selectivity plot. The metrics illustrated here are z-scoring (Panels A and B), AMI (Panels C and D) and raw ratio (Panels E and F) The voxels were also divided into "grey matter" voxels and "venous" voxels by their tSNR. The bars represent the average of all six participants, with each pair of joint circles represent an individual subject.

I also attempted to evaluate the effectiveness of the alternative metrics (Figure 7-10) to corroborate the findings of my computational simulation. The AMI metric was very noisy on the 7T data, similar to

what was observed in computational simulations. The negative values of AMI reflect that effect of the noise is masking the attentional modulation as any attentional modulation should give rise to a positive AMI value by definition.

The raw ratio performs slightly better than the AMI for 7T data, but it is also noisier than the Deming regression. This is in line with my expectations as the large number of voxels with small Task D- contrast values (as observed in Figure 7-9) is likely to distort the raw average of the contrast ratios.

Lastly, I also looked at the effectiveness of z-scoring in removing laminar bias, using a similar methodology as Lawrence et al., 2019. My results show that z-scoring is unsuccessful in removing the superficial bias in the data as the voxels still demonstrate a superficial bias after z-scoring.

7.5 Discussion

In this chapter, I showed that my GE data suffered from the same superficial bias problem noted in the literature (Fracasso et al., 2018; Polimeni et al., 2010; Yacoub et al., 2013) and demonstrated that the application of my two proposed corrections (Deming regression and exclusion of "venous" voxels) was able to remove the superficial bias. Simply excluding "venous" voxels was unsuccessful in mitigating superficial bias as seen from Figure 7-10. Application of Deming regression without removing "venous" voxels is able to mitigate most of the effects of superficial bias but the estimates becomes substantially noisier.

The Deming regression of the selectivity estimates of TaskD+/TaskD- was constant across layers. While this shows that the Deming regression is successful in removing the laminar bias, I was unable to discern any difference in attention modulation across layers. This suggests that the attention modulation was constant across layers, in contrast to previous literature (Kok et al., 2016; Lawrence et al., 2019; Muckli et al., 2015). However, this lack of difference across layers could also be due to other factors, such as low power, insufficient motion correction and the lack of specificity of BOLD contrast.

While I only utilized experienced MRI participants for this study to minimize participant movement, there will always still be a small amount of motion present. Moreover, due to the submillimetre voxel sizes employed at 7T, even the smallest drift could affect the data substantially. The employment of additional motion correction methods, such as prospective motion correction (Huang et al., 2018; Stucht et al., 2015) or more complex retrospective motion correction (Gallichan et al., 2016; Yarach et al., 2015), could potentially unmask laminar effects. While I have shown the ability to correct for the superficial bias in the GE sequences, it is still possible for there to be residual draining vein effects,

which would reduce the specificity of the sequence. Thus, the blurring of signals across layers could also mask potential laminar effects. Alternative sequences, such as VASO or ASL (Huber et al., 2017b; Kashyap et al., 2019; Lu et al., 2013), could potentially untangle laminar effects due to their higher specificity, but at the cost of lower sensitivity. However, it is also important to note VASO and ASL sequences also have longer TR and reduced spatial coverage and might not be able to capture all the ROIs for this study. Moreover, as this was a preliminary study to assess the 7T data quality and validate the various methods of improvement presented throughout this thesis, I only utilized six participants. This small number of participants could result in insufficient power and hence, no discernible difference between layers. To address some of these issues, I am currently planning to repeat this study with a larger cohort (20 participants) and with PMC applied. This would allow us to eliminate lack of power and participant motion as probable confounds.

My computational simulation also compared the Deming regression employed above with the current methods of normalization being employed for 7T— raw ratios (Kashyap et al., 2017) and AMI (Liu et al., 2019). My simulation demonstrated that by taking the Deming regression of TaskD+/TaskD-, I was able to remove the superficial bias present in the simulated data. Deming regression was able to recover the underlying attention modulation accurately and precisely and also captured the variations in attention modulation across laminar layers. Other methods were notably noisier and did not reflect the underlying attention modulation profile across laminar layers. This simulation agrees with the observations from my 7T data, which showed that applying Deming regression was able to remove the superficial bias in the data while other metrics were substantially noiser (AMI, raw ratio) or unsuccessful (z-scoring).

Next, I validated the usage of Deming regression by generating scatterplots of TaskD+ against TaskD-. I observed that most of the voxels clustered along the best fit line, suggesting that Deming regression is indeed capturing the average voxel behaviour in the ROI and not unduly influenced by outliers. These scatterplots also excluded the possibility of improper normalization giving rise to the lack of laminar effects. At a neurological level, the absence of voxels clustered along the y=x diagonal and along the x-axis indicated that similar voxels are recruited for both attention modulation and stimuli representation since I expect voxels that were purely recruited for attention modulation should cluster along the y=x diagonal while voxels that respond purely to the stimuli representation should cluster along the x-axis.

My initial laminar analysis (without correction for superficial bias) demonstrated a consistent superficial bias across all ROIs in agreement with previous literature. While I was unable to compare the relative responses across different laminar layers in this analysis (due to the dominant effect of

superficial bias), it is interesting to note that all layers showed attention modulation and stimuli representation. The presence of the stimuli representation in all layers agree with the results presented by Polimeni et al., 2010, where they observed a retinotopic representation of the stimuli in all layers of V1. The presence of attention modulation across all layers is contrary to previous laminar studies on top-down effects in the visual cortex, which have only observed attention effects in either the superficial (Muckli et al., 2015) or deep (Kok et al., 2016) layers. However, a recent publication (Lawrence et al., 2019) also found the presence of top-down effects across all laminar layers, in agreement with my findings here.

7.6 Conclusion

In this chapter, I demonstrated that Deming regression combined with the exclusion of "venous" voxels was successful in correcting for the superficial bias present in GE sequences. This approach was further validated using a computational simulation, where Deming regression was shown to outperform other normalization metrics. On the neuroscience front, I demonstrated that similar voxels are recruited for both attention modulation and stimuli representation. However, I was unable to discern any difference in attention modulation across laminar layers. A repetition of this study with a larger cohort and PMC is planned for future work to verify whether the lack of difference across laminar layers is due to lack of power, motion or that the underlying pattern is indeed constant across layers.

7.7 Supplementary Materials

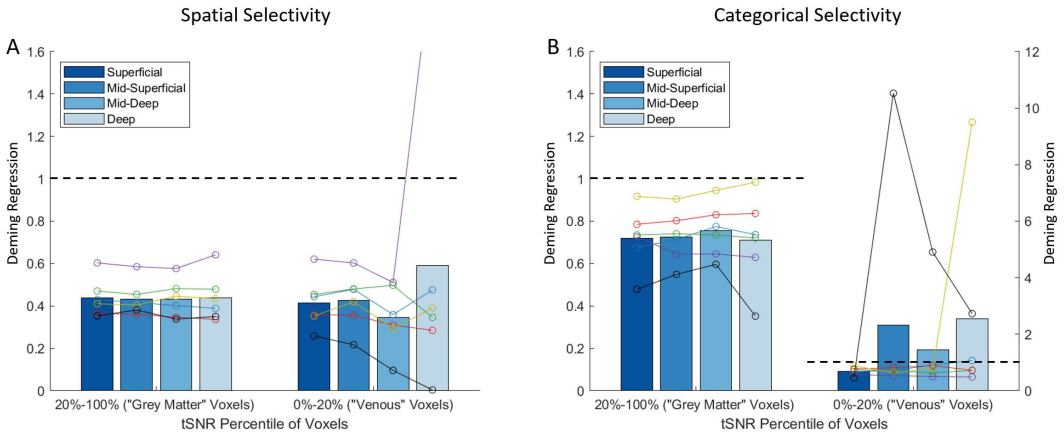

Supplementary Figure 7-1: Plots of the location selectivity (Panel A) and category selectivity (Panel B) contrast ratio of TaskD+/TaskD- obtained at 7T across different layers, with a different threshold for "venous" voxels as compared to Figure 7-8. All other aspects of the plot were held constant. The bars represent the average of all six participants, with each pair of joint circles represent an individual subject. The same colour represents the same participant throughout all plots. Note that the "venous" voxels in Panel B has a different scale. The "grey matter" voxel plots are extremely similar despite the different thresholds, suggesting that the exact value of the threshold does not impact the results.

2700

8 Overall Discussion

The appeal of MRI is clear— providing a safe, non-invasive way to acquire high resolution images of the brain in real time while the participant is awake, or even carrying out cognitive tasks. Moreover, this is an exciting time for MRI research, with constant innovations in multiple fronts—novel sequences, higher fields and more complex analyses. However, it is important to tread carefully and avoid the various pitfalls in these uncharted territories. The large amounts of data, coupled with thermal and physiological noise and artefacts arising from the higher fields, can lead to false positives and erroneous conclusions, perhaps best highlighted by the famous dead salmon experiment (Bennett et al., 2009). Novel sequences and new analyses can also give rise to new artefacts and anomalies that researchers have not encountered before. In this thesis, I looked at four methods (PMC, BBR realignment, LDC analysis and Deming regression) to improve the data quality of fMRI data and demonstrated how the utilization of these methods can help improve the sensitivity and accuracy of fMRI analysis. In addition, I also carried out identical tasks at 3T and 7T with the same participants, allowing me to compare the quality of the data obtained across scanners.

Typical fMRI experiments last in the range of 30 minutes to 2 hours to ensure that they have sufficient power to detect differences in activation (Murphy et al., 2007). As such, it is inevitable that all participants will move through the course of the scan, even if explicitly instructed to stay still. Even the best trained participants will often have unavoidable drift and unconscious motions due to respiratory (~1mm) and cardiac activity (~100um) (Maclaren et al., 2012) which can impact data quality (Hutton et al., 2011), especially at higher resolutions. As such, it is important to accurately correct for motion, be it during acquisition or during post-processing. PMC and BBR realignment are two complimentary methods that I evaluated in this thesis to address participant motion.

PMC utilizes an in-bore optical camera to track a Moiré phase marker attached to the participant so as to be able to obtain real time positional information on the participant's motion. This motion data is utilized to update the co-ordinates of the acquisition box prior to the acquisition of each slice (for 2D GE sequences). This ensures that the position of the acquisition box is tightly coupled to the participant's head and thus, the same voxel throughout the entire time series should correspond to the same point in the participant's brain. In Chapter 3, I demonstrated the application of PMC on 3T fMRI data and show that there was indeed a benefit of PMC at higher resolutions and when probing fine grain activation patterns. I also demonstrated that my custom marker attachment solution (utilizing dental putty and a dental tray to create a mouthpiece) performed similarly to dentist moulded mouthpieces in previous studies (Stucht et al., 2015; Todd et al., 2015). In addition, my custom moulded mouthpiece has the added advantage of being cheap and convenient, merely

requiring participants to be present a few minutes prior to the scan to mould the mouthpiece. This alternative addressed the issue of marker attachment with much less effort and could help in encouraging a more wide-spread adoption of the PMC system.

BBR realignment is a post-acquisition method for motion correction that realigns the fMRI time series. At 7T, the higher field strength gives rise to bigger distortions and signal inhomogeneities. In Chapter 6, I demonstrated that utilizing BBR realignment out-performs conventional VBR methods when realigning a 7T fMRI time series. BBR realignment is a novel way of utilizing the BBR cost function (previously employed to co-register images across modalities to good results) to realign each fMRI volume to the structural template, and hence, realigning the fMRI volumes to each other. This method outperforms standard VBR methods and gives rise to higher tNSR and fCNR. Thus, employment of this method in post-processing pipelines could help unmask any subtle differences in activations that could have otherwise been masked by poor realignment.

BBR realignment can be used independently or together with PMC. While PMC is able to capture and remove a substantial portion of participant motion, my analysis (Figure 3-6) showed that there are still small amounts of residual motion that PMC fails to correct. Thus, employment of BBR realignment could complement PMC, ensuring that most of the participant motion is removed from the data and no longer acts as a residual confound. I was unable to show any interaction between BBR realignment and PMC as BBR realignment did not work on 3T data due to the lower spatial resolution.

After post-processing of the data, there is a need to collapse the gigantic amounts of information into smaller and more manageable representational metrics so that researchers are able to visualise and compare their data. Multivariate pattern analysis (MVPA) is an emerging field that is becoming increasingly popular due to the higher sensitivity and the ability to investigate the multidimensional information present in the pattern of voxel activations compared with standard mass univariate analysis. One of the most commonly adopted MVPA methods is SVM classification (Mahmoudi et al., 2012; Misaki et al., 2010), which generates a decision boundary using the training data and validates it on the testing data. However, using both experimental and simulated data, I showed that LDC is a more sensitive metric than SVM (Chapter 4). LDC utilizes the training data to generate a discriminant and the testing data is mapped onto this discriminant. The resultant distance between the two conditions along the discriminant is indicative of the robustness of the difference in fMRI response between the two conditions. This method sidesteps multiple problems of SVM— less stable estimates of individual blocks, rigid decision boundaries and discretization of the results. Thus, I believe that the utilization of LDC for analysing fMRI data would improve the sensitivity of the analysis and potentially unmask subtle effects.

The last method for improving data quality that I proposed is specific to the laminar analysis of 7T data, an area that has been garnering increasing interest in recent years (Kashyap et al., 2017; Kok et al., 2016; Lawrence et al., 2019; Muckli et al., 2015). Due to the superficial bias present in GE sequences, it is difficult to interpret and compare results across different layers. While different groups have employed various normalization methods (Kashyap et al., 2017; Lawrence et al., 2019; Liu et al., 2019), as far as I am aware, there have been no studies done on the effectiveness of the methods and whether they actually remove the superficial bias. In Chapter 7, I utilized a computational simulation to showcase that Deming regression is optimal for removing superficial bias relative to other metrics, such as a simple ratio or AMI. The simulation shows that Deming regression is able to accurately recover the underlying attention modulation and the other metrics are much noisier than Deming regression. Applying Deming regression to a 7T dataset, in conjunction with the removal of venous voxels, demonstrated the successful removal of superficial bias, agreeing with the simulation results. The usage of Deming regression to normalize laminar data and remove superficial bias will be extremely useful for laminar analysis and can help unmask different modulations across laminar layers.

With new 7T scanners popping up all around the globe at a rapid pace, it is also worth evaluating whether the higher field strength is actually beneficial, or even needed, for typical fMRI studies. While 7T offers substantially higher SNR, it also has its own host of associated problems, including higher susceptibility to field inhomogeneities and participant motion. By repeating the same experimental paradigm at both 3T and 7T (Chapter 5), I showed that data acquired at both scanners showed similar results in terms of activation patterns across ROIs. While there were greater activation magnitudes at 7T, this was also accompanied by an increase in variance, both within and across participants. Thus, it is difficult to determine whether 7T increases sensitivity. My results suggest that for standard fMRI experiment simply investigating ROI-level activity, 3T data would suffice. However, if researchers are interested in probing laminar layers or columns, 7T scanners would be required to acquire data at sufficiently high resolution. Moreover, it is important to note that I was comparing across resolutions and scanners (3mm isotropic for 3T and 0.8mm isotropic for 7T). Thus, it is possible that by acquiring lower resolution data at 7T, I would be able to see an improvement in terms of sensitivity.

8.1 Future Work

Due to technical difficulties, I was unable to implement PMC at 7T for this thesis. Given that PMC only showed significant improvements for 1.5mm isotropic data, I suspect that the benefits of PMC would

be even more apparent at higher resolution at 7T. I plan to validate this theory in a future study by carrying out the visual attention paradigm (Section 2.1.2) with and without PMC at 7T.

In addition, the same experiment will also provide insight into the interaction between the two motion correction methods I have employed— PMC and BBR realignment. I believe that both methods help to mitigate motion effects but does not hit the gold standard of absolutely zero motion effects independently. Thus, the application of both methods should further improve data quality relative to the application of either methods individually.

Lastly, I also seek to address some neuroscience questions with this experiment. My current results were unable to show any difference in attention modulation across layers. However, I only utilized a small sample size (six participants) and no PMC was applied. Thus, its is possible that this experiment had insufficient power to detect differences in attention modulation across layers, which I believe is more likely than the alternative hypothesis of constant attention modulation across all layers. By repeating the same paradigm with 20 participants and PMC, I hope to be able to discern the laminar bias of attention modulation.

In addition to the planned future work above, it would also be interesting to carry out a few additional experiments to supplement the findings present in this thesis. Firstly, while my BBR realignment results are convincingly better than the standard realignment, I utilized an unconventional FOV due to the need to capture both early and higher visual areas. Therefore, while unlikely, it is possible that the improvement due to BBR realignment is merely applicable to the FOV employed here, rather than being a general improvement for all possible FOVs. An additional study on the impact of the various realignment methods with different FOVs would address this issue and potentially strengthen the case for widespread implementation of BBR realignment as a standard realignment methodology.

Further comparisons of 3T and 7T data would also be relevant, especially if the voxel sizes were matched across scanners. With similar voxel sizes, 7T acquisitions could allow for faster scan times, higher SNR or a combination of both. Due to the complex nature of MRI scans and the various noises and their interactions, it is possible that there will not be a clear answer to which field strength is better. The optimal scanner and resolution to use will likely depend on a variety of factors, including the sequence parameters, the post-processing and analysis methods, nature of the task, the ROIs examined and perhaps even the model of the scanners used.

8.2 Conclusion

Since the first MRI image was produced in 1973, the field of MRI has grown by leaps and bounds, with an exponential increase in the number of MRI-related publications every year. The ability to study the human brain while it is at work is a tantalizing one, made even more attractive by the non-invasive and harmless nature of the procedure. However, in the pursuit of novel acquisitions sequences and new analysis methods, it is important to ensure the validity of these methods and their corresponding results through careful evaluation.

My work presented in this thesis demonstrated a variety of methods (PMC, BBR realignment, LDC analysis and Deming regression) to improve data quality when acquiring at 3T or 7T. My results, both computational and experimental, support the assertions that the utilization of my proposed improvements would be beneficial to fMRI data quality. This is critical to fMRI studies, since proper processing and analyses would increase the sensitivity and accuracy of the results, potentially unmasking subtle effects and reducing false positives.

9 References

Abdulkadir, A., Ronneberger, O., Christian Wolf, R., Pfleiderer, B., Saft, C., Kloppel, S., 2013. Functional and Structural MRI Biomarkers to Detect Pre-Clinical Neurodegeneration. Curr. Alzheimer Res. 10, 125–134. https://doi.org/10.2174/1567205011310020002

Abdulrahman, H., Henson, R.N., 2016. Effect of trial-to-trial variability on optimal event-related fMRI design: Implications for Beta-series correlation and multi-voxel pattern analysis. Neuroimage 125, 756–766. https://doi.org/10.1016/j.neuroimage.2015.11.009

Adams, D.L., Piserchia, V., Economides, J.R., Horton, J.C., 2015. Vascular supply of the cerebral cortex is specialized for cell layers but not columns. Cereb. Cortex 25, 3673–3681. https://doi.org/10.1093/cercor/bhu221

Alink, A., Krugliak, A., Walther, A., Kriegeskorte, N., 2013. fMRI orientation decoding in V1 does not require global maps or globally coherent orientation stimuli. Front. Psychol. 4. https://doi.org/10.3389/fpsyg.2013.00493

Andersson, J.L.R., Hutton, C., Ashburner, J., Turner, R., Friston, K., 2001. Modeling geometric deformations in EPI time series. Neuroimage 13, 903–919. https://doi.org/10.1006/nimg.2001.0746

Andersson, J.L.R., Skare, S., Ashburner, J., 2003. How to correct susceptibility distortions in spin-echo echo-planar images: Application to diffusion tensor imaging. Neuroimage 20, 870–888. https://doi.org/10.1016/S1053-8119(03)00336-7

Andre, J.B., Bresnahan, B.W., Mossa-Basha, M., Hoff, M.N., Patrick Smith, C., Anzai, Y., Cohen, W.A., 2015. Toward quantifying the prevalence, severity, and cost associated with patient motion during clinical MR examinations. J. Am. Coll. Radiol. 12, 689–695. https://doi.org/10.1016/j.jacr.2015.03.007

Ashburner, J., Friston, K., 2003. Rigid Body Registration and Interpolation, in: Human Brain Function: Second Edition. pp. 635–653. https://doi.org/10.1016/B978-012264841-0/50034-2

Bandettini, P.A., Wong, E.C., Hinks, R.S., Tikofsky, R.S., Hyde, J.S., 1992. Time course EPI of human brain function during task activation. Magn. Reson. Med. 25, 390–397. https://doi.org/10.1002/mrm.1910250220

Bazin, P., Weiss, M., Dinse, J., Schaefer, A., Trampel, R., Turner, R., 2012. A computational pipeline for subject-specific, ultra-high resolution cortical analysis at 7 Tesla. 18th Annu. Meet. Organ. Hum. Brain Mapp. 883.

Belliveau, J., Kennedy, D., McKinstry, R., Buchbinder, B., Weisskoff, R., Cohen, M., Vevea, J., Brady, T., Rosen, B., 1991. Functional mapping of the human visual cortex. Science (80-.). 254, 716–719.

Bennett, C., Miller, M., Wolford, G., 2009. Neural correlates of interspecies perspective taking in the post-mortem Atlantic Salmon: an argument for multiple comparisons correction. Neuroimage 47, S125. https://doi.org/10.1016/s1053-8119(09)71202-9

Bianciardi, M., Fukunaga, M., Van Gelderen, P., De Zwart, J.A., Duyn, J.H., 2011. Negative BOLD-fMRI signals in large cerebral veins. J. Cereb. Blood Flow Metab. 31, 401–412. https://doi.org/10.1038/jcbfm.2010.164

Birn, R.M., Saad, Z.S., Bandettini, P.A., 2001. Spatial heterogeneity of the nonlinear dynamics in the FMRI BOLD response. Neuroimage 14, 817–826. https://doi.org/10.1006/nimg.2001.0873

Boxerman, J.L., Bandettini, P.A., Kwong, K.K., Baker, J.R., Davis, T.L., Rosen, B.R., Weisskoff, R.M., 1995. The intravascular contribution to fmri signal change: monte carlo modeling and diffusion-weighted studies in vivo. Magn. Reson. Med. 34, 4–10. https://doi.org/10.1002/mrm.1910340103

Bracci, S., Op de Beeck, H., 2016. Dissociations and Associations between Shape and Category Representations in the Two Visual Pathways. J. Neurosci. 36, 432–444. https://doi.org/10.1523/JNEUROSCI.2314-15.2016

Brett, M., Penny, W., Kiebel, S., 2003. Introduction to Random Field Theory. Hum. Brain Funct. Second Ed. 867–879. https://doi.org/10.1016/B978-012264841-0/50046-9

Buxton, R.B., 2001. The elusive initial dip. Neuroimage 13, 953–958. https://doi.org/10.1006/nimg.2001.0814

Caccomo, S., 2017. FDA clears first 7T magnetic resonance imaging device. FDA News Release.

Callaghan, M.F., Josephs, O., Herbst, M., Zaitsev, M., Todd, N., Weiskopf, N., 2015. An evaluation of prospective motion correction (PMC) for high resolution quantitative MRI. Front. Neurosci. 9, 1–9. https://doi.org/10.3389/fnins.2015.00097

Chambers, M.C., Bhushan, C., Haldar, J.P., Leahy, R.M., Shattuck, D.W., 2015. Correcting inhomogeneity-induced distortion in FMRI using non-rigid registration. Proc. - Int. Symp. Biomed. Imaging 2015-July, 1364–1367. https://doi.org/10.1109/ISBI.2015.7164129

Chen, J.J., Pike, G.B., 2009. Origins of the BOLD post-stimulus undershoot. Neuroimage 46, 559–568. https://doi.org/10.1016/j.neuroimage.2009.03.015

Cortes, C., Vapnik, V., 1995. Support-vector networks. Mach. Learn. 20, 273–297. https://doi.org/10.1007/BF00994018

Costafreda, S.G., Fu, C.H.Y., Picchioni, M., Toulopoulou, T., McDonald, C., Kravariti, E., Walshe, M., Prata, D., Murray, R.M., McGuire, P.K., 2011. Pattern of neural responses to verbal fluency shows diagnostic specificity for schizophrenia and bipolar disorder. BMC Psychiatry 11, 18. https://doi.org/10.1186/1471-244X-11-18

Coutanche, M.N., 2013. Distinguishing multi-voxel patterns and mean activation: Why, how, and what does it tell us? Cogn. Affect. Behav. Neurosci. 13, 667–673. https://doi.org/10.3758/s13415-013-0186-2

Davis, T., LaRocque, K.F., Mumford, J.A., Norman, K.A., Wagner, A.D., Poldrack, R.A., 2014. What do differences between multi-voxel and univariate analysis mean? How subject-, voxel-, and trial-level variance impact fMRI analysis. Neuroimage 97, 271–283. https://doi.org/10.1016/j.neuroimage.2014.04.037

Davis, T., Poldrack, R.A., 2013. Measuring neural representations with fMRI: Practices and pitfalls. Ann. N. Y. Acad. Sci. 1296, 108–134. https://doi.org/10.1111/nyas.12156

De Martino, F., Valente, G., Staeren, N., Ashburner, J., Goebel, R., Formisano, E., 2008. Combining multivariate voxel selection and support vector machines for mapping and classification of fMRI spatial patterns. Neuroimage 43, 44–58. https://doi.org/10.1016/j.neuroimage.2008.06.037

Dechent, P., Schütze, G., Helms, G., Merboldt, K.D., Frahm, J., 2011. Basal cerebral blood volume during the poststimulation undershoot in BOLD MRI of the human brain. J. Cereb. Blood Flow Metab. 31, 82–89. https://doi.org/10.1038/jcbfm.2010.133

Detre, G.J., Haxby, J. V., Norman, K.A., Polyn, S.M., 2006. Beyond mind-reading: multi-voxel pattern

analysis of fMRI data. Trends Cogn. Sci. 10, 424–430. https://doi.org/doi: DOI: 10.1016/j.tics.2006.07.005

Diedrichsen, J., Wiestler, T., Ejaz, N., 2013. A multivariate method to determine the dimensionality of neural representation from population activity. Neuroimage 76, 225–235. https://doi.org/10.1016/j.neuroimage.2013.02.062

Dietrich, B.E., Brunner, D.O., Wilm, B.J., BarmeT, C., Gross, S., Kasper, L., Haeberlin, M., Schmid, T., Vannesjo, S.J., Pruessmann, K.P., 2016. A field camera for MR sequence monitoring and system analysis. Magn. Reson. Med. 75, 1831–1840. https://doi.org/10.1002/mrm.25770

Donahue, M.J., Blicher, J.U., Østergaard, L., Feinberg, D.A., MacIntosh, B.J., Miller, K.L., Günther, M., Jezzard, P., 2009. Cerebral blood flow, blood volume, and oxygen metabolism dynamics in human visual and motor cortex as measured by whole-brain multi-modal magnetic resonance imaging. J. Cereb. Blood Flow Metab. 29, 1856–1866. https://doi.org/10.1038/jcbfm.2009.107

Dumoulin, S.O., Wandell, B.A., 2008. Population receptive field estimates in human visual cortex. Neuroimage 39, 647–60. https://doi.org/10.1016/j.neuroimage.2007.09.034

Engstrom, M., Martensson, M., Avventi, E., Norbeck, O., Skare, S., 2015. Collapsed fat navigators for brain 3D rigid body motion. Magn. Reson. Imaging 33, 984–991. https://doi.org/10.1016/j.mri.2015.06.014

Feinberg, D.A., Vu, A.T., Goebel, R., Kemper, V.G., Poser, B.A., Yacoub, E., De Martino, F., 2015. Sub-millimeter T2 weighted fMRI at 7 T: comparison of 3D-GRASE and 2D SE-EPI. Front. Neurosci. 9. https://doi.org/10.3389/fnins.2015.00163

Feinberg, D.A., Yacoub, E., 2012. The rapid development of high speed, resolution and precision in fMRI. Neuroimage 62, 720–725. https://doi.org/10.1016/j.neuroimage.2012.01.049

Field, A.S., Yen, Y.F., Burdette, J.H., Elster, A.D., 2000. False cerebral activation on BOLD functional MR images: Study of low-amplitude motion weakly correlated to stimulus. Am. J. Neuroradiol. 21, 1388–1396.

Fracasso, A., Luijten, P.R., Dumoulin, S.O., Petridou, N., 2018. Laminar imaging of positive and negative BOLD in human visual cortex at 7 T. Neuroimage 164, 100–111. https://doi.org/10.1016/j.neuroimage.2017.02.038

Freeman, J., Heeger, D.J., Merriam, E.P., 2013. Coarse-scale biases for spirals and orientation in human visual cortex. J. Neurosci. 33, 19695–703. https://doi.org/10.1523/JNEUROSCI.0889-13.2013

Freire, L., Mangin, J.F., 2001. Motion correction algorithms may create spurious brain activations in the absence of subject motion. Neuroimage 14, 709–722. https://doi.org/10.1006/nimg.2001.0869

Freud, E., Plaut, D.C., Behrmann, M., 2016. 'What' Is Happening in the Dorsal Visual Pathway. Trends Cogn. Sci. 20, 773–784. https://doi.org/10.1016/j.tics.2016.08.003

Friston, K.J., Holmes, A.P., Worsley, K.J., Poline, J.P., Frith, C.D., Frackowiak, R.S.J., 1994. Statistical parametric maps in functional imaging: A general linear approach. Hum. Brain Mapp. 2, 189–210. https://doi.org/10.1016/j.neuroimage.2016.12.040

Friston, K.J., Josephs, O., Rees, G., Turner, R., 1998. Nonlinear event-related responses in fMRI. Magn. Reson. Med. 39, 41–52. https://doi.org/10.1002/mrm.1910390109

Friston, K.J., Williams, S., Howard, R., Frackowiak, R.S.J., Turner, R., 1996. Movement-related effects in fMRI time-series. Magn. Reson. Med. 35, 346–355.

https://doi.org/10.1002/mrm.1910350312

Furmanski, C.S., Engel, S.A., 2006. An oblique effect in human primary visual cortex. America (NY). 3, 2005–2006.

Gallichan, D., Marques, J.P., Gruetter, R., 2016. Retrospective correction of involuntary microscopic head movement using highly accelerated fat image navigators (3D FatNavs) at 7T. Magn. Reson. Med. 75, 1030–1039. https://doi.org/10.1002/mrm.25670

Glasser, M.F., Sotiropoulos, S.N., Wilson, J.A., Coalson, T.S., Fischl, B., Andersson, J.L., Xu, J., Jbabdi, S., Webster, M., Polimeni, J.R., Van Essen, D.C., Jenkinson, M., 2013. The minimal preprocessing pipelines for the Human Connectome Project. Neuroimage 80, 105–124. https://doi.org/10.1016/j.neuroimage.2013.04.127

Glover, G.H., 2012. Spiral imaging in fMRI. Neuroimage 62, 706–712. https://doi.org/10.1016/j.neuroimage.2011.10.039

Glover, G.H., Li, T.Q., Ress, D., 2000. Image-based method for retrospective correction of physiological motion effects in fMRI: RETROICOR. Magn. Reson. Med. 44, 162–167. https://doi.org/10.1002/1522-2594(200007)44:1<162::AID-MRM23>3.0.CO;2-E

Goebel, R., Esposito, F., Formisano, E., 2006. Analysis of Functional Image Analysis Contest (FIAC) data with BrainVoyager QX: From single-subject to cortically aligned group General Linear Model analysis and self-organizing group Independent Component Analysis. Hum. Brain Mapp. 27, 392–401. https://doi.org/10.1002/hbm.20249

Greve, D.N., Fischl, B., 2009. Accurate and robust brain image alignment using boundary-based registration. Neuroimage 48, 63–72. https://doi.org/10.1016/j.neuroimage.2009.06.060

Grotegerd, D., Suslow, T., Bauer, J., Ohrmann, P., Arolt, V., Stuhrmann, A., Heindel, W., Kugel, H., 2013. Discriminating unipolar and bipolar depression by means of fMRI and pattern classification: A pilot study. Eur. Arch. Psychiatry Clin. Neurosci. 263, 119–131. https://doi.org/http://dx.doi.org/10.1007/s00406-012-0329-4

Henriksson, L., Nurminen, L., Hyvarinen, A., Vanni, S., Hyvarinen, A., Vanni, S., Hyvarinen, A., Vanni, S., 2008. Spatial frequency tuning in human retinotopic visual areas. J Vis 8, 1–13. https://doi.org/10.1167/8.10.5.Introduction

Herbst, M., MacLaren, J., Weigel, M., Korvink, J., Hennig, J., Zaitsev, M., 2012. Prospective motion correction with continuous gradient updates in diffusion weighted imaging. Magn. Reson. Med. 67, 326–338. https://doi.org/10.1002/mrm.23230

Hirano, Y., Stefanovic, B., Silva, A.C., 2011. Spatiotemporal Evolution of the Functional Magnetic Resonance Imaging Response to Ultrashort Stimuli. J. Neurosci. 31, 1440–1447. https://doi.org/10.1523/jneurosci.3986-10.2011

Hoeft, F., McCandliss, B.D., Black, J.M., Gantman, A., Zakerani, N., Hulme, C., Lyytinen, H., Whitfield-Gabrieli, S., Glover, G.H., Reiss, A.L., Gabrieli, J.D.E., 2011. Neural systems predicting long-term outcome in dyslexia. Proc. Natl. Acad. Sci. 108, 361–366. https://doi.org/10.1073/pnas.1008950108

Hu, X., Le, T.H., Uğurbil, K., 1997. Evaluation of the early response in fMRI in individual subjects using short stimulus duration. Magn. Reson. Med. 37, 877–884. https://doi.org/10.1002/mrm.1910370612

Hua, J., Stevens, R.D., Huang, A.J., Pekar, J.J., Van Zijl, P.C.M., 2011. Physiological origin for the BOLD poststimulus undershoot in human brain: Vascular compliance versus oxygen metabolism. J.

Cereb. Blood Flow Metab. 31, 1599–1611. https://doi.org/10.1038/jcbfm.2011.35

Huang, P., Carlin, J.D., Alink, A., Kriegeskorte, N., Henson, R.N., Correia, M.M., 2018. Prospective motion correction improves the sensitivity of fMRI pattern decoding. Hum. Brain Mapp. 39, 4018–4031. https://doi.org/10.1002/hbm.24228

Huber, L., Ivanov, D., Hall, A., Guidi, M., Bandettini, P.A., Gonzalez-Castillo, J., Goense, J., Chen, G., Marrett, S., Poser, B.A., Stüber, C., Handwerker, D.A., Jangraw, D.C., 2017a. High-Resolution CBV-fMRI Allows Mapping of Laminar Activity and Connectivity of Cortical Input and Output in Human M1. Neuron 96, 1253-1263.e7. https://doi.org/10.1016/j.neuron.2017.11.005

Huber, L., Uludağ, K., Möller, H.E., 2017b. Non-BOLD contrast for laminar fMRI in humans: CBF, CBV, and CMRO2. Neuroimage. https://doi.org/10.1016/j.neuroimage.2017.07.041

Hutton, C., Andersson, J., Deichmann, R., Weiskopf, N., 2013. Phase informed model for motion and susceptibility. Hum. Brain Mapp. 34, 3086–3100. https://doi.org/10.1002/hbm.22126

Hutton, C., Josephs, O., Stadler, J., Featherstone, E., Reid, A., Speck, O., Bernarding, J., Weiskopf, N., 2011. The impact of physiological noise correction on fMRI at 7T. Neuroimage 57, 101–112. https://doi.org/10.1016/j.neuroimage.2011.04.018

Jezzard, P., Clare, S., 1999. Sources of distortion in functional MRI data. Hum. Brain Mapp. 8, 80–85. https://doi.org/10.1002/(SICI)1097-0193(1999)8:2/3<80::AID-HBM2>3.0.CO;2-C

Johnstone, T., Ores Walsh, K.S., Greischar, L.L., Alexander, A.L., Fox, A.S., Davidson, R.J., Oakes, T.R., 2006. Motion correction and the use of motion covariates in multiple-subject fMRI analysis. Hum. Brain Mapp. 27, 779–788. https://doi.org/10.1002/hbm.20219

Josephs, O., Deichmann, R., Corfield, D.R., Turner, R., Hutton, C., 2002. Compensation of Susceptibility-Induced BOLD Sensitivity Losses in Echo-Planar fMRI Imaging. Neuroimage 15, 120–135. https://doi.org/10.1006/nimg.2001.0985

Kamitani, Y., Tong, F., 2005. Decoding the visual and subjective contents of the human brain. Nat. Neurosci. 8, 679–685. https://doi.org/10.1038/nn1444

Kanwisher, N., O'Craven, K.M., Downing, P.E., 1999. fMRI evidence for objects as the units of attentional selection. Nature 401, 584–587. https://doi.org/10.1038/44134

Kashyap, S., Ivanov, D., Havlicek, M., Poser, B., Uludag, K., 2019. Laminar CBF and BOLD fMRI in the human visual cortex using arterial spin labelling at 7T, in: Proceedings of the 27th Scientific Meeting of ISMRM. p. 609.

Kashyap, S., Ivanov, D., Havlicek, M., Poser, B.A., Uludağ, K., 2017. Impact of acquisition and analysis strategies on cortical depth-dependent fMRI. Neuroimage. https://doi.org/10.1016/j.neuroimage.2017.05.022

Kashyap, S., Ivanov, D., Havlicek, M., Sengupta, S., Poser, B.A., Uludağ, K., 2018. Resolving laminar activation in human V1 using ultra-high spatial resolution fMRI at 7T. Sci. Rep. 8. https://doi.org/10.1038/s41598-018-35333-3

Kay, K., Jamison, K.W., Vizioli, L., Zhang, R., Margalit, E., Ugurbil, K., 2019. A critical assessment of data quality and venous effects in sub-millimeter fMRI. Neuroimage 189, 847–869. https://doi.org/10.1016/j.neuroimage.2019.02.006

Kay, K.N., Winawer, J., Mezer, A., Wandell, B.A., 2013. Compressive spatial summation in human visual cortex [WWW Document]. J. Neurophysiol. https://doi.org/10.1152/jn.00105.2013

Kemper, V.G., De Martino, F., Vu, A.T., Poser, B.A., Feinberg, D.A., Goebel, R., Yacoub, E., 2015. Sub-

millimeter T<inf>2</inf> weighted fMRI at 7 T: Comparison of 3D-GRASE and 2D SE-EPI. Front. Neurosci. 9, 1–14. https://doi.org/10.3389/fnins.2015.00163

Kiefer, B., Wang, J., Jakob, P.M., Jellus, V., Nittka, M., Heidemann, R.M., Haase, A., Griswold, M.A., 2002. Generalized autocalibrating partially parallel acquisitions (GRAPPA). Magn. Reson. Med. 47, 1202–1210. https://doi.org/10.1002/mrm.10171

Kim, D.S., Duong, T.Q., Kim, S.G., 2000. High-resolution mapping of iso-orientation columns by fMRI. Nat. Neurosci. 3, 164–169. https://doi.org/10.1038/72109

Kim, T., Kim, S.G., 2011. Temporal dynamics and spatial specificity of arterial and venous blood volume changes during visual stimulation: Implication for BOLD quantification. J. Cereb. Blood Flow Metab. 31, 1211–1222. https://doi.org/10.1038/jcbfm.2010.226

Kindermann, S.S., Bell, A.J., Makeig, S., Brown, G.G., Sejnowski, T.J., Jung, T., Mckeown, M.J., 2002. Analysis of fMRI data by blind separation into independent spatial components. Hum. Brain Mapp. 6, 160–188. https://doi.org/10.1002/(sici)1097-0193(1998)6:3<160::aid-hbm5>3.3.co;2-r

Kok, P., Bains, L.J., Van Mourik, T., Norris, D.G., De Lange, F.P., 2016. Selective activation of the deep layers of the human primary visual cortex by top-down feedback. Curr. Biol. 26, 371–376. https://doi.org/10.1016/j.cub.2015.12.038

Kriegeskorte, N., 2008. Representational similarity analysis – connecting the branches of systems neuroscience. Front. Syst. Neurosci. https://doi.org/10.3389/neuro.06.004.2008

Kriegeskorte, N., Diedrichsen, J., 2016. Inferring brain-computational mechanisms with models of activity measurements. Philos. Trans. R. Soc. Lond. B. Biol. Sci. 371, 489–495. https://doi.org/10.1098/rstb.2016.0278

Kriegeskorte, N., Formisano, E., Sorger, B., Goebel, R., 2007. Individual faces elicit distinct response patterns in human anterior temporal cortex. Proc Natl Acad Sci U S A 104, 20600–20605.

Kriegeskorte, N., Goebel, R., Bandettini, P., 2006. Information-based functional brain mapping. Proc. … 103, 3863–3868.

Kriegeskorte, N., Mur, M., Ruff, D.A., Kiani, R., Bodurka, J., Esteky, H., Tanaka, K., Bandettini, P.A., 2008. Matching categorical object representations in inferior temporal cortex of man and monkey. Neuron 60, 1126–41. https://doi.org/10.1016/j.neuron.2008.10.043

Kwong, K.K., Belliveau, J.W., Chesler, D.A., Goldberg, I.E., Weisskoff, R.M., Poncelet, B.P., Kennedy, D.N., Hoppel, B.E., Cohen, M.S., Turner, R., 1992. Dynamic magnetic resonance imaging of human brain activity during primary sensory stimulation. Proc. Natl. Acad. Sci. U. S. A. 89, 5675–9.

LaConte, S., Strother, S., Cherkassky, V., Anderson, J., Hu, X., 2005. Support vector machines for temporal classification of block design fMRI data. Neuroimage 26, 317–329. https://doi.org/10.1016/j.neuroimage.2005.01.048

Lauterbur, P.C., 1973. Image formation by induced local interactions: examples employing nuclear magnetic resonance. Nature 242, 190–191.

Lawrence, S.J., Norris, D.G., de Lange, F.P., 2019. Dissociable laminar profiles of concurrent bottom-up and top-down modulation in the human visual cortex. Elife 8. https://doi.org/10.7554/eLife.44422

Ledoit, O., Wolf, M., 2003. Improved estimation of the covariance matrix of stock returns with an application to portfolio selection. J. Empir. Financ. 10, 603–621.

https://doi.org/10.1016/S0927-5398(03)00007-0

Leprince, Y., Poupon, F., Delzescaux, T., Hasboun, D., Poupon, C., Riviere, D., 2015. Combined Laplacian-equivolumic model for studying cortical lamination with ultra high field MRI (7 T). Proc. - Int. Symp. Biomed. Imaging 2015-July, 580–583. https://doi.org/10.1109/ISBI.2015.7163940

Lindauer, U., Royl, G., Leithner, C., Kühl, M., Gold, L., Gethmann, J., Kohl-Bareis, M., Villringer, A., Dirnagl, U., 2001. No evidence for early decrease in blood oxygenation in rat whisker cortex in response to functional activation. Neuroimage 13, 988–1001. https://doi.org/10.1006/nimg.2000.0709

Liu, C., Qian, C., Zhang, Z., Sun, K., An, J., Wang, D., Zhang, P., 2019. Attention modulation of layer-specific signals in human visual cortex, in: Proceedings of the 27th Scientific Meeting of ISMRM.

Logothetis, N.K., Pauls, J., Augath, M., Trinath, T., Oeltermann, A., 2001. Neurophysiological investigation of the basis of the fMRI signal. Nature 412, 150–7. https://doi.org/10.1038/35084005

Lu, H., Hua, J., van Zijl, P.C.M., 2013. Noninvasive functional imaging of cerebral blood volume with vascular-space-occupancy (VASO) MRI. NMR Biomed. 26, 932–948. https://doi.org/10.1002/nbm.2905

Lutti, A., Thomas, D.L., Hutton, C., Weiskopf, N., 2013. High-resolution functional MRI at 3 T: 3D/2D echo-planar imaging with optimized physiological noise correction. Magn. Reson. Med. 69, 1657–1664. https://doi.org/10.1002/mrm.24398

Maclaren, J., Armstrong, B.S.R.R., Barrows, R.T., Danishad, K.A., Ernst, T., Foster, C.L., Gumus, K., Herbst, M., Kadashevich, I.Y., Kusik, T.P., Li, Q., Lovell-Smith, C., Prieto, T., Schulze, P., Speck, O., Stucht, D., Zaitsev, M., 2012. Measurement and Correction of Microscopic Head Motion during Magnetic Resonance Imaging of the Brain. PLoS One 7. https://doi.org/10.1371/journal.pone.0048088

Maclaren, J., Herbst, M., Speck, O., Zaitsev, M., 2013. Prospective Motion Correction in Brain Imaging : A Review. Magn. Reson. Med. 636, 621–636. https://doi.org/10.1002/mrm.24314

Maclaren, J., Speck, O., Stucht, D., Schulze, P., Hennig, J., Zaitsev, M., 2010. Navigator accuracy requirements for prospective motion correction. Magn. Reson. Med. 63, 162–170. https://doi.org/10.1002/mrm.22191

Magri, C., Schridde, U., Murayama, Y., Panzeri, S., Logothetis, N.K., 2012. The Amplitude and Timing of the BOLD Signal Reflects the Relationship between Local Field Potential Power at Different Frequencies. J. Neurosci. 32, 1395–1407. https://doi.org/10.1523/jneurosci.3985-11.2012

Mahmoudi, A., Takerkart, S., Regragui, F., Boussaoud, D., Brovelli, A., 2012. Multivoxel Pattern Analysis for fMRI Data: A Review. Comput. Math. Methods Med. 2012, 1–14. https://doi.org/10.1155/2012/961257

Mallard, J., Hutchison, J.M.S., Edelstein, W., Ling, R., Foster, M., 1979. Imaging by nuclear magnetic resonance and its bio-medical implications. J. Biomed. Eng. 1, 153–160. https://doi.org/10.1016/0141-5425(79)90036-0

Malonek, D., Grinvald, A., 1996. Interactions between electrical activity and cortical microcirculation revealed by imaging spectroscopy: Implications for functional brain mapping. Science (80-.). 272, 551–554. https://doi.org/10.1126/science.272.5261.551

Mandelkow, H., de Zwart, J.A., Duyn, J.H., 2016. Linear Discriminant Analysis Achieves High

Classification Accuracy for the BOLD fMRI Response to Naturalistic Movie Stimuli. Front. Hum. Neurosci. 10. https://doi.org/10.3389/fnhum.2016.00128

Mansfield, P., 1977. Multi-planar image formation using NMR spin echoes. J. Phys. C Solid State Phys. 10, L55–L58.

Markov, N.T., Vezoli, J., Chameau, P., Falchier, A., Quilodran, R., Huissoud, C., Lamy, C., Misery, P., Giroud, P., Ullman, S., Barone, P., Dehay, C., Knoblauch, K., Kennedy, H., 2014. Anatomy of hierarchy: Feedforward and feedback pathways in macaque visual cortex. J. Comp. Neurol. 522, 225–259. https://doi.org/10.1002/cne.23458

McGibney, G., Smith, M.R., Nichols, S.T., Crawley, A., 1993. Quantitative evaluation of several partial fourier reconstruction algorithms used in mri. Magn. Reson. Med. 30, 51–59. https://doi.org/10.1002/mrm.1910300109

Meier, T.B., Desphande, A.S., Vergun, S., Nair, V.A., Song, J., Biswal, B.B., Meyerand, M.E., Birn, R.M., Prabhakaran, V., 2012. Support vector machine classification and characterization of age-related reorganization of functional brain networks. Neuroimage 60, 601–613. https://doi.org/10.1016/j.neuroimage.2011.12.052

Miller, K.L., Luh, W.-M., Liu, T.T., Martinez, A., Obata, T., Wong, E.C., Frank, L.R., Buxton, R.B., 2001. Nonlinear temporal dynamics of the cerebral blood flow response. Hum. Brain Mapp. 13, 1–12. https://doi.org/10.1002/hbm.1020

Misaki, M., Kim, Y., Bandettini, P.A., Kriegeskorte, N., 2010. Comparison of multivariate classifiers and response normalizations for pattern-information fMRI. Neuroimage 53, 103–118. https://doi.org/10.1016/j.neuroimage.2010.05.051

Morgan, V.L., Dawant, B.M., Li, Y., Pickens, D.R., 2007. Comparison of fMRI statistical software packages and strategies for analysis of images containing random and stimulus-correlated motion. Comput. Med. Imaging Graph. 31, 436–446. https://doi.org/10.1016/j.compmedimag.2007.04.002

Muckli, L., De Martino, F., Vizioli, L., Petro, L.S., Smith, F.W., Ugurbil, K., Goebel, R., Yacoub, E., 2015. Contextual Feedback to Superficial Layers of V1. Curr. Biol. 25, 2690–2695. https://doi.org/10.1016/j.cub.2015.08.057

Muraskin, J., Ooi, M.B., Goldman, R.I., Krueger, S., Thomas, W.J., Sajda, P., Brown, T.R., 2013. Prospective active marker motion correction improves statistical power in BOLD fMRI. Neuroimage 68, 154–161. https://doi.org/10.1016/j.neuroimage.2012.11.052

Murphy, K., Bodurka, J., Bandettini, P.A., 2007. How long to scan? The relationship between fMRI temporal signal to noise ratio and necessary scan duration. Neuroimage 34, 565–574. https://doi.org/10.1016/j.neuroimage.2006.09.032

Niazy, R.K., De Stefano, N., Beckmann, C.F., De Luca, M., Vickers, J., Matthews, P.M., Behrens, T.E.J., Saunders, J., Flitney, D.E., Jenkinson, M., Zhang, Y., Bannister, P.R., Woolrich, M.W., Smith, S.M., Brady, J.M., Johansen-Berg, H., Drobnjak, I., 2004. Advances in functional and structural MR image analysis and implementation as FSL. Neuroimage 23, S208–S219. https://doi.org/10.1016/j.neuroimage.2004.07.051

Nowogrodzki, A., 2018. The world's strongest MRI machines are pushing human imaging to new limits. Nature 563, 24–26. https://doi.org/10.1038/d41586-018-07182-7

O'Brien, T.J., Wong, Y.T., Moffat, B.A., Grayden, D.B., Cleary, J.O., Oxley, T.J., Yoo, P.E., Mulcahy, C.B., Opie, N.L., Ordidge, R.J., Ng, A., John, S.E., Farquharson, S., 2017. 7T-fMRI: Faster temporal resolution yields optimal BOLD sensitivity for functional network imaging specifically at high

spatial resolution. Neuroimage 164, 214–229. https://doi.org/10.1016/j.neuroimage.2017.03.002

Oakes, T.R., Johnstone, T., Ores Walsh, K.S., Greischar, L.L., Alexander, A.L., Fox, A.S., Davidson, R.J., 2005. Comparison of fMRI motion correction software tools. Neuroimage 28, 529–543. https://doi.org/10.1016/j.neuroimage.2005.05.058

Ogawa, S., Lee, T.-M., Stepnoski, R., Chen, W., Zhu, X.-H., Ugurbil, K., 2002. An approach to probe some neural systems interaction by functional MRI at neural time scale down to milliseconds. Proc. Natl. Acad. Sci. 97, 11026–11031. https://doi.org/10.1073/pnas.97.20.11026

Ogawa, S., Lee, T.M., Kay, A.R., Tank, D.W., 1990. Brain magnetic resonance imaging with contrast dependent on blood oxygenation. Proc. Natl. Acad. Sci. U. S. A. 87, 9868–72.

Ogawa, S., Tank, D.W., Menon, R., Ellermann, J.M., Kim, S.G., Merkle, H., Ugurbil, K., 1992. Intrinsic signal changes accompanying sensory stimulation: functional brain mapping with magnetic resonance imaging. Proc. Natl. Acad. Sci. U. S. A. 89, 5951–5955. https://doi.org/10.1073/pnas.89.13.5951

Olman, C.A., Yacoub, E., 2011. High-Field fMRI for Human Applications: An Overview of Spatial Resolution and Signal Specificity. Open Neuroimag. J. 5, 74–89. https://doi.org/10.2174/1874440001105010074

Ontivero-Ortega, M., Lage-Castellanos, A., Valdes-Sosa, M., 2015. A framework for massive searchlight MVPA approach. IFMBE Proc. 49, 468–471. https://doi.org/10.1007/978-3-319-13117-7_120

Ooi, M.B., Krueger, S., Muraskin, J., Thomas, W.J., Brown, T.R., 2011. Echo-planar imaging with prospective slice-by-slice motion correction using active markers. Magn. Reson. Med. 66, 73–81. https://doi.org/10.1002/mrm.22780

Pauling, L., Coryell, C.D., 1936. The Magnetic Properties and Structure of Hemoglobin, Oxyhemoglobin and Carbonmonoxyhemoglobin. Proc. Natl. Acad. Sci. 22, 210–216. https://doi.org/10.1073/pnas.22.4.210

Penny, D.W., Friston, J.K., Ashburner, T.J., Kiebel, J.S., Nichols, E.T., 2011. Statistical parametric mapping: the analysis of functional brain images.

Petcharunpaisan, S., 2010. Arterial spin labeling in neuroimaging. World J. Radiol. 2, 384. https://doi.org/10.4329/wjr.v2.i10.384

Polimeni, J.R., Fischl, B., Greve, D.N., Wald, L.L., 2010. Laminar analysis of 7T BOLD using an imposed spatial activation pattern in human V1. Neuroimage 52, 1334–1346. https://doi.org/10.1016/j.neuroimage.2010.05.005

Poser, B.A., Van Mierlo, E., Norris, D.G., 2011. Exploring the post-stimulus undershoot with spin-echo fMRI: Implications for models of neurovascular response. Hum. Brain Mapp. 32, 141–153. https://doi.org/10.1002/hbm.21003

Rees, G., Friston, K., Koch, C., 2000. A direct quantitative relationship between the functional properties of human and macaque V5. Nat. Neurosci. 3, 716–723. https://doi.org/10.1038/76673

Renvall, V., Nangini, C., Hari, R., 2014. All that glitters is not BOLD: inconsistencies in functional MRI. Sci. Rep. 4, 3920. https://doi.org/10.1038/srep03920

Rockland, K.S., 2017. What do we know about laminar connectivity? Neuroimage. https://doi.org/10.1016/j.neuroimage.2017.07.032

Rockland, K.S., Knutson, T., 2000. Feedback connections from area MT of the squirrel monkey to areas V1 and V2. J. Comp. Neurol. 425, 345–368. https://doi.org/10.1002/1096-9861(20000925)425:3<345::AID-CNE2>3.0.CO;2-O

Rockland, K.S., Virga, A., 1989. Terminal arbors of individual "Feedback" axons projecting from area V2 to V1 in the macaque monkey: A study using immunohistochemistry of anterogradely transported Phaseolus vulgaris-leucoagglutinin. J. Comp. Neurol. 285, 54–72. https://doi.org/10.1002/cne.902850106

Runeson, G., Boynton, M., Murray, S.O., 2013. Effects of Task and Attentional Selection on Responses in Human Visual Cortex. J. Neurophysiol. 109, 2606–2617.

Sadaghiani, S., Uğurbil, K., Uludağ, K., 2009. Neural activity-induced modulation of BOLD poststimulus undershoot independent of the positive signal. Magn. Reson. Imaging 27, 1030–1038. https://doi.org/10.1016/j.mri.2009.04.003

Savoy, R.L., Cox, D.D., 2003. Functional magnetic resonance imaging (fMRI) "'brain reading'": detecting and classifying distributed patterns of fMRI activity in human visual cortex. Neuroimage 19, 10.

Schulz, J., Siegert, T., Bazin, P.L., Maclaren, J., Herbst, M., Zaitsev, M., Turner, R., 2014. Prospective slice-by-slice motion correction reduces false positive activations in fMRI with task-correlated motion. Neuroimage 84, 124–132. https://doi.org/10.1016/j.neuroimage.2013.08.006

Sengupta, A., Speck, O., Yakupov, R., Kanowski, M., Tempelmann, C., Pollmann, S., Hanke, M., 2018. The effect of acquisition resolution on orientation decoding from V1 : comparison of 3T and 7T.

Sengupta, A., Yakupov, R., Speck, O., Pollmann, S., Hanke, M., 2017. The effect of acquisition resolution on orientation decoding from V1 BOLD fMRI at 7 T. Neuroimage 148, 64–76. https://doi.org/10.1016/j.neuroimage.2016.12.040

Seymour, K., Clifford, C.W.G., Logothetis, N.K., Bartels, A., 2010. Coding and binding of color and form in visual cortex. Cereb. Cortex 20, 1946–1954. https://doi.org/10.1093/cercor/bhp265

Smith, S.M., Beckmann, C.F., Andersson, J., Auerbach, E.J., Bijsterbosch, J., Douaud, G., Duff, E., Feinberg, D.A., Griffanti, L., Harms, M.P., Kelly, M., Laumann, T., Miller, K.L., Moeller, S., Petersen, S., Power, J., Salimi-Khorshidi, G., Snyder, A.Z., Vu, A.T., Woolrich, M.W., Xu, J., Yacoub, E., Uğurbil, K., Van Essen, D.C., Glasser, M.F., 2013. Resting-state fMRI in the Human Connectome Project. Neuroimage 80, 144–168. https://doi.org/10.1016/j.neuroimage.2013.05.039

Stehling, M.K., Turner, R., Mansfield, P., 1991. Echo-planar imaging: Magnetic resonance imaging in a fraction of a second. Science (80-.). 254, 43–50.

Stucht, D., Danishad, A., Schulze, P., Godenschweger, F., Zaitsev, M., Speck, O., Danishad, K.A., Schulze, P., Godenschweger, F., Zaitsev, M., Speck, O., 2015. Highest Resolution in vivo Human Brain MRI Using Prospective Motion Correction. PLoS One 10. https://doi.org/10.1371/journal.pone.0133921

Tak, S., Noh, J., Cheong, C., Zeidman, P., Razi, A., Penny, W.D., Friston, K.J., 2018. A validation of dynamic causal modelling for 7T fMRI. J. Neurosci. Methods 305, 36–45. https://doi.org/10.1016/j.jneumeth.2018.05.002

Todd, N., Josephs, O., Callaghan, M.F., Lutti, A., Weiskopf, N., 2015. Prospective motion correction of 3D echo-planar imaging data for functional MRI using optical tracking. Neuroimage 113, 1–12. https://doi.org/10.1016/j.neuroimage.2015.03.013

Todd, N., Moeller, S., Auerbach, E.J., Yacoub, E., Flandin, G., Weiskopf, N., 2016. Evaluation of 2D multiband EPI imaging for high-resolution, whole-brain, task-based fMRI studies at 3T: Sensitivity and slice leakage artifacts. Neuroimage 124, 32–42. https://doi.org/10.1016/j.neuroimage.2015.08.056

Tong, F., Swisher, J.D., Gore, J.C., Gatenby, J.C., Wolfe, B.A., Moon, C.-H., Kim, S.-G., 2010. Multiscale Pattern Analysis of Orientation-Selective Activity in the Primary Visual Cortex. J. Neurosci. 30, 325–330. https://doi.org/10.1523/JNEUROSCI.4811-09.2010

Tripoliti, E.E., Fotiadis, D.I., Argyropoulou, M., Manis, G., 2010. A six stage approach for the diagnosis of the Alzheimer's disease based on fMRI data. J. Biomed. Inform. 43, 307–320. https://doi.org/10.1016/j.jbi.2009.10.004

Tyler, C.W., Likova, L.T., Nicholas, S.C., 2015. Analysis of neural-BOLD coupling through four models of the neural metabolic demand. Front. Neurosci. 9. https://doi.org/10.3389/fnins.2015.00419

Uludağ, K., Blinder, P., 2018. Linking brain vascular physiology to hemodynamic response in ultra-high field MRI. Neuroimage 168, 279–295. https://doi.org/10.1016/j.neuroimage.2017.02.063

Ungerleider, L.G., Mishkin, M., 1982. Two cortical visual systems, in: The Analysis of Visual Behavior. pp. 549–586.

Van Der Kouwe, A.J.W., Benner, T., Dale, A.M., 2006. Real-time rigid body motion correction and shimming using cloverleaf navigators. Magn. Reson. Med. 56, 1019–1032. https://doi.org/10.1002/mrm.21038

Vaziri-Pashkam, M., Xu, Y., 2017. Goal-Directed Visual Processing Differentially Impacts Human Ventral and Dorsal Visual Representations. J. Neurosci. 37, 8767–8782. https://doi.org/10.1523/JNEUROSCI.3392-16.2017

Vazquez, A.L., Noll, D.C., 1998. Nonlinear aspects of the BOLD response in functional MRI. Neuroimage 7, 108–118. https://doi.org/10.1006/nimg.1997.0316

Viswanathan, A., Freeman, R.D., 2007. Neurometabolic coupling in cerebral cortex reflects synaptic more than spiking activity. Nat. Neurosci. 10, 1308–1312. https://doi.org/10.1038/nn1977

Walther, A., Nili, H., Ejaz, N., Alink, A., Kriegeskorte, N., Diedrichsen, J., 2016. Reliability of dissimilarity measures for multi-voxel pattern analysis. Neuroimage 137, 188–200. https://doi.org/10.1016/j.neuroimage.2015.12.012

Ward, H. a, Riederer, S.J., Grimm, R.C., Ehman, R.L., Felmlee, J.P., Jack, C.R., 2000. Prospective multiaxial motion correction for fMRI. Magn. Reson. Med. 43, 459–69.

Weygandt, M., Blecker, C.R., Schäfer, A., Hackmack, K., Haynes, J.D., Vaitl, D., Stark, R., Schienle, A., 2012. FMRI pattern recognition in obsessive-compulsive disorder. Neuroimage 60, 1186–1193. https://doi.org/10.1016/j.neuroimage.2012.01.064

Wright, K.L., Hamilton, J.I., Griswold, M.A., Gulani, V., Seiberlich, N., 2014. Non-Cartesian parallel imaging reconstruction. J. Magn. Reson. Imaging 40, 1022–1040. https://doi.org/10.1002/jmri.24521

Xing, D., Yeh, C.-I., Burns, S., Shapley, R.M., 2012. Laminar analysis of visually evoked activity in the primary visual cortex. Proc. Natl. Acad. Sci. U. S. A. 109, 13871–13876. https://doi.org/10.1073/pnas.1201478109

Yacoub, E., De Martino, F., Zimmermann, J., Ugurbil, K., Goebel, R., Muckli, L., Ugurbil, K., Yacoub, E., Goebel, R., 2013. Cortical Depth Dependent Functional Responses in Humans at 7T: Improved Specificity with 3D GRASE. PLoS One 8, e60514. https://doi.org/10.1371/journal.pone.0060514

Yacoub, E., Hu, X., 2001. Detection of the early decrease in fMRI signal in the motor area. Magn. Reson. Med. 45, 184–190. https://doi.org/10.1002/1522-2594(200102)45:2<184::AID-MRM1024>3.0.CO;2-C

Yakupov, R., Lei, J., Hoffmann, M.B., Speck, O., 2017. False fMRI activation after motion correction. Hum. Brain Mapp. 38, 4497–4510. https://doi.org/10.1002/hbm.23677

Yancey, S.E., Rotenberg, D.J., Tam, F., Chiew, M., Ranieri, S., Biswas, L., Anderson, K.J.T., Nicole Baker, S., Wright, G. a., Graham, S.J., 2011. Spin-history artifact during functional MRI: Potential for adaptive correction. Med. Phys. 38, 4634. https://doi.org/10.1118/1.3583814

Yarach, U., Luengviriya, C., Danishad, A., Stucht, D., Godenschweger, F., Schulze, P., Speck, O., 2015. Correction of gradient nonlinearity artifacts in prospective motion correction for 7T MRI. Magn. Reson. Med. 73, 1562–1569. https://doi.org/10.1002/mrm.25283

Yoon, J.H., Nguyen, D. V., McVay, L.M., Deramo, P., Minzenberg, M.J., Ragland, J.D., Niendham, T., Solomon, M., Carter, C.S., 2012. Automated classification of fMRI during cognitive control identifies more severely disorganized subjects with schizophrenia. Schizophr. Res. 135, 28–33. https://doi.org/10.1016/j.schres.2012.01.001

Zaitsev, M., Akin, B., LeVan, P., Knowles, B.R., 2016. Prospective Motion Correction in Functional MRI. Neuroimage 0–1. https://doi.org/10.1016/j.neuroimage.2016.11.014

Zhu, C.Z., Zang, Y.F., Cao, Q.J., Yan, C.G., He, Y., Jiang, T.Z., Sui, M.Q., Wang, Y.F., 2008. Fisher discriminative analysis of resting-state brain function for attention-deficit/hyperactivity disorder. Neuroimage 40, 110–120. https://doi.org/10.1016/j.neuroimage.2007.11.029

Zong, X., Huang, J., 2011. Linear coupling of undershoot with BOLD response in ER-fMRI and nonlinear BOLD response in rapid-presentation ER-fMRI. Neuroimage 57, 391–402. https://doi.org/10.1016/j.neuroimage.2011.04.067